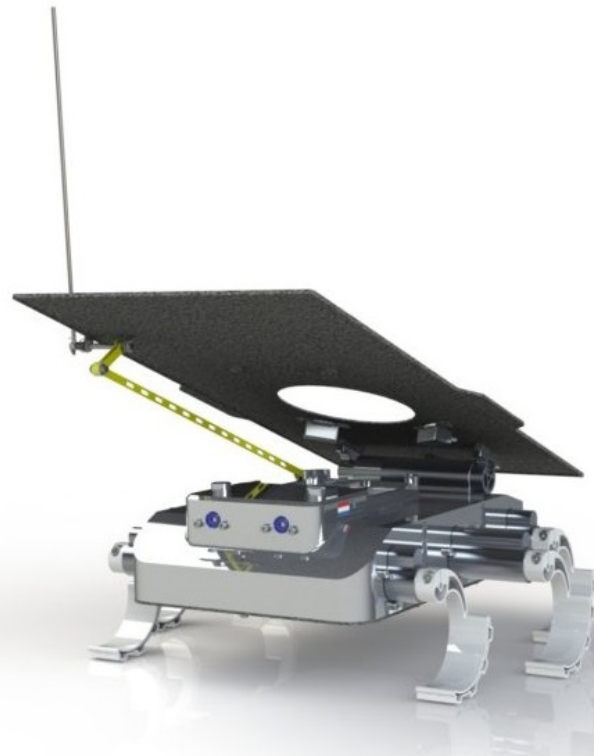


Department of Precision and Microsystems Engineering

A Mass Optimization Study of the Lunar Zebro Chassis

C.M. Sinck

Report no : 2023.073
Coach : Dr.Ir. J.F.L. Goosen
Professor : Dr.Ir. J.F.L. Goosen
Specialisation : Engineering Mechanics
Type of report : Master Thesis
Date : 29 August 2023



Preface

This MSc Thesis contains the conducted research in methods for mass optimization of the Lunar Zebro chassis. It is the main result of a graduation project toward the completion of my MSc degree within the department of High-Tech Engineering and Structural Optimization Mechanics at the Delft University of Technology.

My interest in structural analysis and design is the main motivation in the pursuit of this degree. The desire to apply and expand this knowledge, combined with a fascination for space exploration, made me eager to select this subject for my thesis project. I am grateful for this opportunity to learn about modern design methods and applications, and especially the challenge of exploring methods for new applications.

With thanks to Dr. Ir. J.F.L. Goosen for the supervision and guidance in the conducted research and creation of this report.

To Jan, Elke and Stan for your contributions in the biweekly meetings and brainstorm sessions.

To Maria, for your outstanding support and patience along the way.

And a final thank you to my friends and family for your support during this process.

Marc Sinck
Delft, August 2023

Abstract

A prototype lunar rover is in development by students of the TU Delft since 2017. It is a nanorover based on the terrestrial ZeBRo design, now named the Lunar Zebro. The Lunar Zebro is a prototype design as a proof of concept for nanorover capabilities. With a chassis of 200 by 140 by 60 millimeters, fitting on a sheet of A5 paper, the Lunar Zebro is intended to be the smallest and lightest autonomous rover on the Moon to date. The objective is to traverse a distance of 200 meters during a lunar day, surviving the harsh environment and strong solar radiation. Due to the limited time budget there is little refinement in the structural design. The resulting functional but heavy design leaves many opportunities for optimization.

While there are many examples of successful planetary rover missions, little is published concerning the design of the structures. This report contains further analysis of the design of satellite structures. The various structure types and design requirements highlight the importance of thermal transport and resistance to mechanical launch loads. Compared to the deployed planetary rovers, the Lunar Zebro is unique in many ways. The small size facilitates production of the current monolithic chassis which is ideal in its thermal conduction and environmental sealing properties. However with a constant plate thickness and no reinforcing substructure, the structure is not an efficient loadbearing design. Due to the many requirements and unique mission profile of the Lunar Zebro, there is no clear method by which to optimize the structure.

To better understand the current structure and reduce the mass, a case study is performed with Finite Element Methods. After validating a modelling approach for thin plate reinforcement, a simplified chassis structure is generated. Maintaining the essential configuration of the chassis and connected components, the response to the static launch load of 10G is analysed. Several methods for rib placement design are tested while reducing the plate thickness. Buckling behaviour and CNC production limitations are accounted for in this approach. To minimally affect the other design requirements, the stiffness of the structure is maintained. While the placement of ribs is sensitive to the vicinity of connected components, equally stiff designs can be obtained with reinforcement grids. Reducing the plate thickness by 66.6%, a mass reduction in the order of 50% can be achieved without sacrificing stiffness. However, local adjustments are required to prevent plastic deformation in high stress areas.

From there the analysis and design of reinforcement grids is investigated further. Grids are often seen in aerospace applications due to the convenient geometries for CNC production, light weight and predictable orthotropic or isotropic behaviour. A smeared stiffness approach is investigated that relates the rib and plate interaction to composite plate theory. Applying this analysis method provides beneficial insight in the parameters and related stiffness behaviour of a grid reinforced plate. By modelling three common grid sections on a hypothetical plate design scenario with varying boundary conditions, the important criteria for the selection and design of a reinforcement grid are provided.

Contents

1	Introduction	1
1.1	Background	1
1.2	Lunar Mission	2
1.2.1	Lunar Environment	2
1.2.2	Lunar Transit	3
1.3	State of the Art	3
1.3.1	Lunar Rovers	4
1.3.2	Mars Rovers	5
1.4	Satellite Structures Design	6
1.4.1	Satellite design process	6
1.4.2	Satellite structure types	7
1.4.3	Thermal management	8
1.4.4	Environmental protection	8
1.5	Lunar Zebro Chassis Design	9
1.5.1	Comparison	9
1.6	Problem Statement	10
2	Research Approach	11
2.1	Structures design and optimization	11
2.1.1	Structure types	11
2.1.2	Modelling methods	13
2.1.3	Optimization methods	13
2.2	Lunar Zebro chassis design	15
2.2.1	Chassis structure configuration	15
2.2.2	Chassis design requirements and methods	16
2.2.3	Chassis optimization approach	17
2.3	Chassis reinforcement design strategy	18
2.3.1	Case study model setup	18
2.3.2	Case study design loads	19
2.3.3	Reinforcement design approach	20
3	Chassis Modelling	21
3.1	Ribs modelling verification	21
3.1.1	Shell deflection comparison	22
3.1.2	Shell-Beam element interaction	22
3.2	Simplified Chassis Analysis	23
3.2.1	Model setup	24
3.2.2	Chassis deflection analysis	26
3.3	Reinforcement Design Test	27
3.3.1	Stiffened plate design	28
3.3.2	Large ribs test	29
3.3.3	Rib grid test	31
3.3.4	Iso grid test	33
3.4	Conclusion	34
4	Grid Reinforcement Analysis	35
4.1	Composite plate theory for grids	35
4.2	Grid test configuration	37
4.2.1	Buckling phenomena and rib sizing	37
4.2.2	Geometry and sizing of tested grids	38

4.3	Grid model analysis	40
4.3.1	Grid model setup	40
4.3.2	Out of plane point load.	41
4.3.3	In plane load	42
4.3.4	Distributed in plane load.	43
4.3.5	Discussion of results	44
4.4	Discussion.	44
5	Conclusion	45
5.1	Conclusion	45
5.2	Recommendations	46
A	Physical testing methods	47
B	Chassis design process evaluation	49
C	Finite Element Analysis Validation	51
D	Simplified model parameters	55
E	Large Rib Test	57
F	Rib Grid Test	59
G	Iso Grid Test	61
H	Grid Equivalent Stiffness Matrix	63
I	Grid comparison OoP load	65
J	Grid comparison in-plane load	69

1

Introduction

1.1. Background

In early 2017 the TU Delft was offered the rare opportunity for a university to develop an autonomous rover to be sent to the moon by the Indian Space Research Organisation (ISRO). The rovers of the TU Delft and a few other universities were intended to be carried as piggyback on the Chandrayaan 3 lunar landing mission, though this uncertain at the time of writing this report. In the TU Delft, research and development continues for potential future missions of the rover.

The rovers are nano class vehicles, serving as proof of concept for the potential of extra-terrestrial exploration by swarming vehicles. The aim of exploration by swarms is to cover more area than an individual rover, with the added capability of risking individual rovers on hazardous terrain. Such expendable robots also offer promising capabilities in assisting human exploration or habitation on the Moon, Mars and possibly more. In this field, mass is a critical aspect in mission planning. Especially in a swarm, any weight savings can be multiplied by all vehicles in the swarm.

To operate on the lunar surface, the TU Delft is developing a lunar adaptation of the six legged ZeBRo, now called the Lunar Zebro. The name is derived from a Dutch acronym of "Zes-Benige Robot". An early prototype of the Lunar Zebro is shown in Figure 1.1. By operating on legs instead of more conventional wheels or tracks, the ability to overcome obstacles and rough terrain is enhanced. This is especially important for small vehicles like the nanorovers. The current design of the Lunar Zebro features a movable solar panel, six C-shaped legs and two cameras for autonomous navigation. The chassis consists of a monolithic aluminium body sealed with a ceramic baseplate at the bottom.

This design is generated by student teams, of which the members change annually. A functioning rover has been rapidly designed and tested for the required certification for space launch. While there is ongoing research and development in new iterations of the Lunar Zebro, the shape and configuration of the structure remains unchanged.

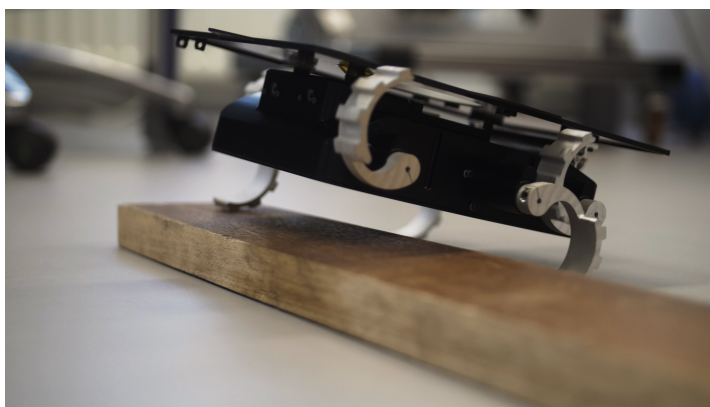


Figure 1.1: The Lunar Zebro

1.2. Lunar Mission

As a proof of concept for nanorovers, the current mission profile of the Lunar Zebro is limited. The goal is to operate for a lunar day, surviving the hostile environment and traverse a distance of 200 meters. To reach the Moon in the first place, the Lunar Zebro must also withstand space travel for a successful lunar transit. The conditions in the lunar environment and transit are explained in this section. Regarding the lunar environment, all information concerning the Moon is obtained from the "Lunar Sourcebook" [1].

1.2.1. Lunar Environment

The Moon is the only natural satellite of the Earth, with a surface area comparable to that of the continent of Asia. It has no magnetic field and a gravitational attraction of just 1.62m/s, only one sixth of Earth's gravity. Therefore it retains virtually no atmosphere. In fact "the six Apollo landings delivered six times as much gas to the lunar surface as there is in the ambient atmosphere" (Heiken et al. 1991, p. 41). This also means there is no effective insulation to trap heat or protect against radiation and micrometeorites.

The same side of the moon always faces the Earth in a phenomenon known as tidal locking. As a result the lunar day is roughly equal to its orbital period, about four weeks on Earth. Due to all these factors the surface temperature varies strongly with the exposure and incidence of sunlight. The mean daytime temperature is 107°C with a maximum of 127°C measured near the equator, whereas the mean temperature at night is -153°C.

The lunar landscape can be separated by two categories: rough highlands and comparatively smooth maria, both of which are shown in Figure 1.2. The highlands are shaped by mountains and many impact craters of various size. On the other hand, maria are shaped by basaltic deposits of ancient volcanic activity and are visibly darker than the highlands. Smooth hills with gentle slopes of less than 20° cover much of the highlands, though steep mountains with 40° slopes are also apparent. Traversing these slopes poses several risks to any surface exploration vehicle. A rover may get stuck in its own tracks, or it may topple and fall down a slope.

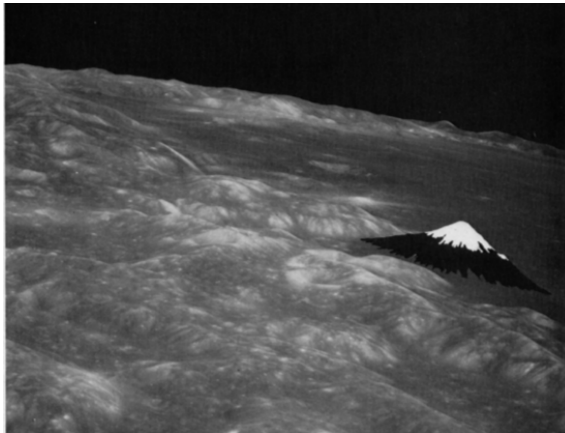


Figure 1.2: Lunar Highlands and Maria, compared to mount Fuji [1]

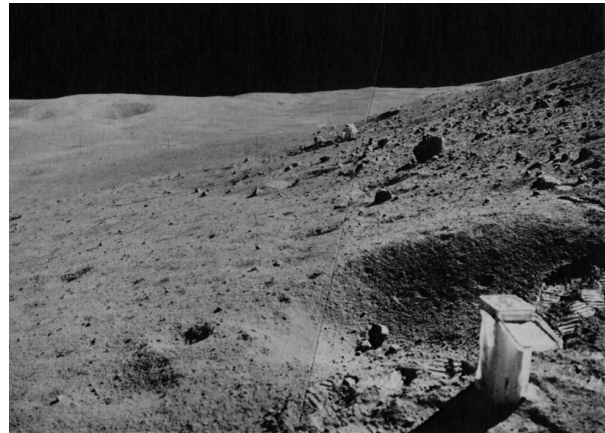


Figure 1.3: A boulder field on Stone Mountain near the Apollo 16 landing site [1]

Volcanic activity and meteoric impacts have covered the Moon in a layer of unconsolidated rock fragments, visible in Figure 1.3. This material is named regolith and varies in size from microscopic particles to pebbles and boulders. Due to the lack of natural erosion, the microscopic regolith are sharp crystalline particles between 40 and 800 micrometres in size. The material properties of these regolith particles is such that they accumulate electrostatic charge from exposure to ultraviolet radiation. The adhesive properties of this regolith has caused problems and equipment failures in past lunar missions, as will be explained with the history of lunar rovers in the next section.

1.2.2. Lunar Transit

It takes an enormous velocity to get any object from the surface of the Earth to the Moon. To reach a circular low Earth orbit, a height of at least 200km above sea-level, a velocity of about 7.8 km/s is required [2]. From here it takes another 3km/s to achieve trans-lunar injection [3]. All fuel that is spent to reach such velocities is accelerated by the fuel spent in the previous burn, and so forth. Therefore mass is a critical limiting factor in space missions.

Any lunar mission achieves trans-lunar injection through a process of several burns, as is shown in Figure 1.4. This was the flight path of the Chandrayaan-2 mission, which had offered to carry the Lunar Zebro and other nanorovers as piggyback payloads. During this transit, critical risks of space travel can be categorized by orbital launch, micrometeorite impacts and radiation.

- **Orbital launch:** launch vehicles generate enormous forces resulting in high acceleration. Taking the SpaceX Falcon-9 characteristics for example [4], a payload is designed for peak accelerations of 8.5g axial and 3g lateral to the launch direction. Additionally dynamic sinusoidal loads in the order of 0.5 to 0.8g affect the structure in a range of 5 to 100Hz. In limited occasions, spacecraft separation stages can deliver shocks of 30g at 100Hz and 1000g in kHz range. Though it should be noted that actual shock levels experienced at the payload adapter are mission-unique.
- **Micrometeors:** Many particles in the form of man made orbital debris and natural micrometeoroids orbit the earth at velocities of about 10km/s [5]. Micrometeoroids orbiting the sun that cross the orbit of the earth may have velocities up to 72km/s. The vast majority of these particles are of sub-millimeter diameters, with larger particles being less common proportionally to their size. On the Moon the overall meteoric flux is lower due to its lower gravity [6]
- **Radiation:** Piggybacked to a lunar lander the Lunar Zebro chassis is expected to cool to -180°C when not exposed to sunlight, while being selectively heated up to 120°C in several occasions. Repeated thermal expansion and contraction of the chassis can result in local strain cycles, weakening the structure by thermomechanical fatigue [7]. Additionally electronics are affected by ionizing radiation. This can cause several problems such as bit flips in the software and component failures in the hardware [8]. These radiation effects have been considered in the component selection and programming of the Lunar Zebro [9].

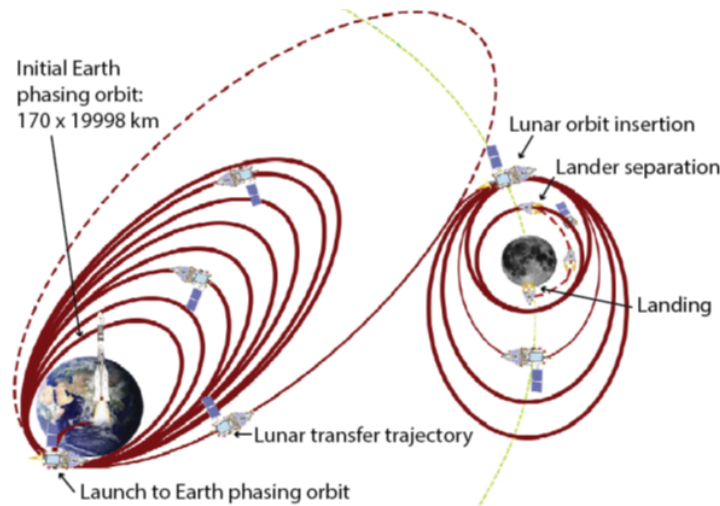


Figure 1.4: Chandrayaan-2 flight path [10]

1.3. State of the Art

In recent decades, multiple planetary rovers have been designed and mainly deployed on Mars. Very little has been publicly published about the structural design of these rovers, with most papers concerning the suspension system structure. The main body of the rovers is referred to as the Warm Electronics Box (WEB). In this section lessons of the Lunar Rovers and Mars Rovers design characteristics are explained. At the end structure types for satellites are briefly covered as there is significantly more information available concerning these structures.

Historically a limited amount of planetary rovers have been applied in space exploration. A planetary rover is defined as a mobile surface spacecraft that explores bodies in space other than the earth. In Table 1.1 an overview is given of launched planetary rovers to date. These are mostly wheeled rovers in the macro weight class above 100 kg and micro rovers of a mass between 10 and 50 kg. One exception is the Soviet Prop-M nanorover (<10 kg) which would operate on skis with a remote power supply [11]. Despite the considerable scale difference between these rovers and the Lunar Zebro, lessons can be learned from the design and operational life of these rovers.

Rover	Weight	Landing	Destination	Mission duration
Lunokhod 1 & 2	756 kg 840 kg	1970 - 1973	Moon	322 & 236 days
Prop-M	4.5 kg	1971	Mars	Failed
Lunar Roving Vehicles	218 kg	1971 - 1972	Moon	3 days
Sojourner	11 kg	1997	Mars	85 days
Spirit & Opportunity	174 kg	2004	Mars	6 years & 14 years
Curiosity	900 kg	2012	Mars	>10 years (ongoing)
Perseverance	1025 kg	2019	Mars	>3 years (ongoing)
Yutu 1 & Yutu 2	140 kg	2013 2019	Moon	32 months (42 days mobile) >3 years (ongoing)
Pragyan	27 kg	2019	Moon	Failed
Zhurong	240 kg	2021	Mars	>1 year (ongoing)

Table 1.1: History of planetary rovers

1.3.1. Lunar Rovers

Since the lunar exploration by American and Russian missions 1970s, no rovers have traversed the moon for several decades. Recently Chinese rovers were deployed successfully, with the Yutu-2 being the first surface exploration mission on the far side of the moon. In the near future ISRO aims to make India the fourth country to deploy a rover on the moon.

Though very little has been published about the Yutu rover design, it has been noted that the Chinese rover appears to copy many features of NASAs Mars rovers [12]. Both operate on a six wheeled chassis with suspension system similar to that seen on the Spirit and Opportunity rovers. The Yutu 1 suffered a control system malfunction and became immobile before its third Lunar night. With its movable solar panels and radioisotope heater, the other systems survived several lunar nights and continued to broadcast after becoming immobile.

Radioisotope heating is common in planetary rovers and was employed on the first extra-planetary rover missions in the 1970s. These Soviet Lunokhod rovers (Figure 1.5) both featured a pressurized magnesium alloy tub as instrument bay, maintaining a stable temperature with a radioisotope heat source and a radiator panel on top [13]. Both rovers successfully operated over several lunar days, traversing 11 and 37km respectively. The Lunokhod 1 rover stopped functioning after the radioisotope heater failed and the internal temperature dropped. The Lunokhod 2 operated successfully until the lid accidentally accumulated lunar dust, and deposited this on the radiator panel at night. As the rover returned from hibernation the next lunar morning, temperatures rose and the systems stopped broadcasting.

Regolith dust was also a concern for the Lunar Roving Vehicles (LRV) in the Apollo missions. These were large manned rovers of about 2 by 3 meters capable of carrying two astronauts as shown in Figure 1.6. The LRV could be operated from Earth if the crew were incapacitated [11].

Critical electronics were mounted to the front of the chassis, protected against the lunar and space environment by a multilayer insulation blanket with cutouts for four radiator panels. Some electronics were connected to the batteries by thermal straps, where the batteries contained two of the four radiator panels. Dust covers protected these radiator panels during operation of the LRV, which were removed manually while parked to allow energy transfer to deep space [14].

NASA mission planning estimated that any dust adhering to the radiator panels could be brushed off by astronauts. Especially on the Apollo 16 and 17 missions this proved largely ineffective, where the LRV batteries exceeded operational temperatures and some instruments had reduced performance due to overheating [15].

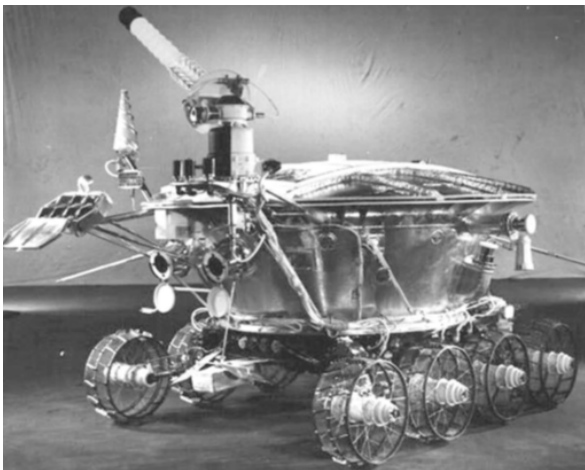


Figure 1.5: Lunokhod 1 rover [11]

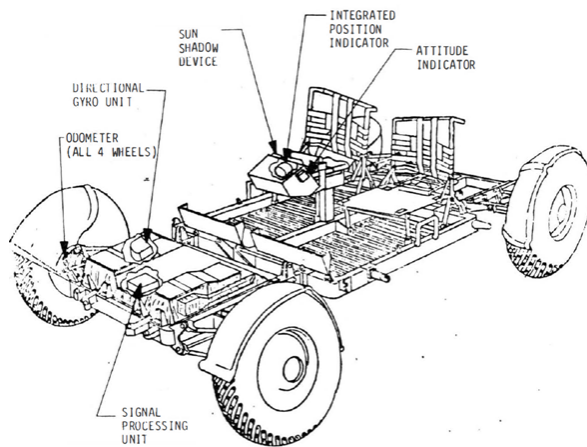


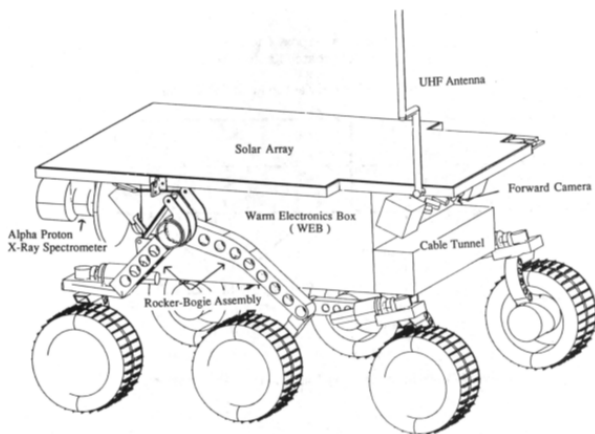
Figure 1.6: LRV without payload [14]

1.3.2. Mars Rovers

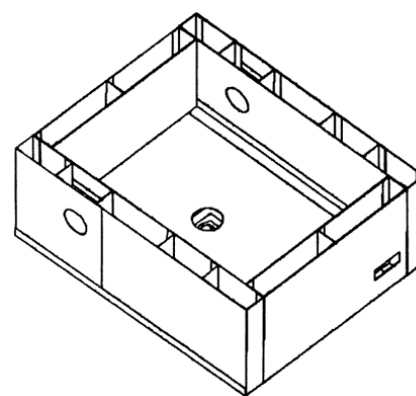
Until recently only NASA has successfully deployed rovers on Mars. In early 2021 Chinas space program successfully landed the Zhurong rover, though again limited information surrounding its design has been published. All Mars rovers from NASA follow the basic structural setup of a six-wheeled rocker-bogie chassis connected to the body through a single axial connection. Each wheel is individually powered by electric motors and steering is provided by four additional motors on the front and aft wheels [11].

Sojourner

Part of the Mars Pathfinder mission, the Sojourner rover is the smallest of all successfully deployed planetary rovers. The WEB is a dual layered composite box filled with aerogel insulation, with overall dimensions of 34 by 27 by 15 cm [16]. Depictions of this rover (a) and WEB structure (b) are displayed in Figure 1.7 below. The axial structural tube which connects the wheel assembly to the WEB also houses radioisotope heaters. Both this tube and interior circuit boards span from side wall to side wall as a design feature to carry structural loads and reduce mass. Here the internal components are integrated with the WEB structure through composite fittings which minimise conductive heat loss. A concept design 'lightweight survivable rover' based on the Sojourner design replaces the radioisotope heaters by a capacitive phase change material, combined with improved WEB insulation [17].



(a) Sojourner structure schematic



(b) WEB composite panels

Figure 1.7: Sojourner schematics [16]

Spirit and opportunity

Following the Pathfinder, the Mars Exploration Rover mission launched two identical rovers, shown in Figure 1.8 below, named Spirit and Opportunity to nearly opposite sites on Mars [18]. These rovers are significantly larger than their predecessor, with a WEB of 86 by 55 by 36.5cm. This is an exoskeleton design of aluminium honeycomb panels with carbon composite facesheets. Component fittings on the WEB and the rocker bogie chassis are made of titanium [19]. Like the Sojourner these rovers are insulated with aerogel and contain radioisotope heaters [20]. For thermal management an uncontrolled heatswitch prevents the battery system from overheating during the day. Once the temperature reaches 18°C, paraffin wax turns liquid and improves the thermal pathway to the external radiator panels. Around Martian noon, usage of highly dissipating electronics is limited to prevent overheating of critical components.

Curiosity and Perseverance

Part of separate missions with different science payloads [21], Curiosity and Perseverance are rovers of similar designs shown in Figure 1.9. Contrary to all previously deployed rovers, these rovers do not apply solar panels for energy generation. Instead electrical power is generated with a radioisotope thermal generator, which also provides heating to the body through a freon pumping system [22]. The body is made of aluminium with external white paint for thermal control. Mechanical and thermal design considerations are decoupled by this design strategy. The only insulation is provided by spacing between components inside the body and the outer walls, which is vented with Martian atmosphere [23].

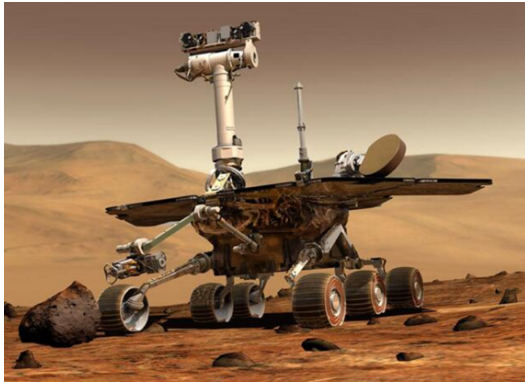


Figure 1.8: Mars Exploration Rover rendering [19]

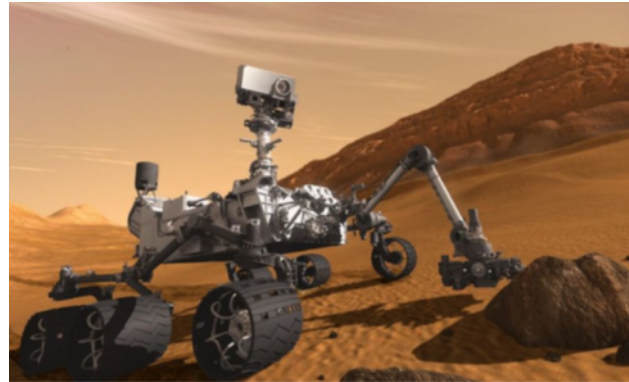


Figure 1.9: Curiosity rover rendering [22]

1.4. Satellite Structures Design

As available information on the design of planetary rovers is scarce, this section considers the design of satellite structures. These structures are designed with similar requirements, resisting orbital transport and the environment of space. Firstly the overall design process is investigated, concerning the setup and configuration of satellite structures and the various loads and requirements. Secondly common structure types of satellites are discussed. Finally methods for managing the thermal and environmental requirements are reviewed.

1.4.1. Satellite design process

In the design of satellite structures there are two main categories to consider. Primary structures are strictly loadbearing, housing equipment and transferring loads to the launch vehicle adapter. Secondary structures include connection points, closeout panels and movable equipment. Both of these are designed with mechanical loads and thermal pathways in mind, though secondary structures are more sensitive to launch vibrations [2] [5] [24].

Design and optimization is typically an iterative process. An example of this process is shown in Figure 1.10 below from a case study of satellite panelling design [25]. The overall shape and size of the structure is defined in the initial stage, where the position and orientation of component is adjusted to balance the load paths in launch and the thermal pathways in operation [2].

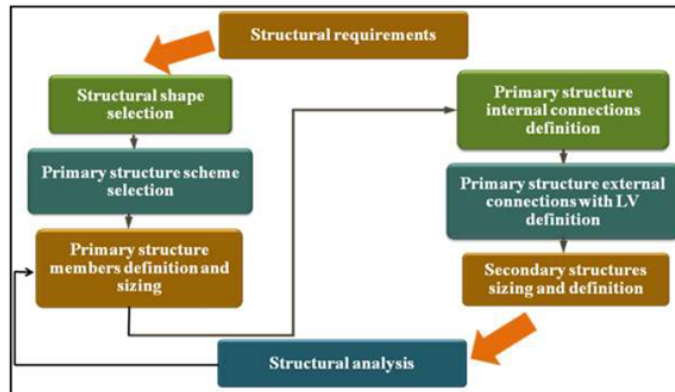


Figure 1.10: Structural design process diagram [25]

The final design of a satellite structure must account for all load scenario's associated with launch and operation. A list of verification requirements is published by ESA which, among other requirements, includes standards for the following structural analyses [26]:

- Static load response
- Dynamic load response (sine and random)
- Shock response
- Fatigue
- Thermoelastic stress/deformation
- Buckling (including composite microbuckling)

1.4.2. Satellite structure types

Looking further into primary structures, common structural schemes seen in spacecraft are: truss structures, skin frames and monocoques [2] [5]. Truss structures consist of axially loaded members in rectangular or triangular arrays, as seen in cubesats in Figure 1.11 below. Skin frame structures combine the load carrying structure with the external plating, using panels with enhanced out of plane stiffness. Possible plate types include composite panels, aluminium honeycombs as seen on Mars rovers or isogrids in micro satellites as shown in Figure 1.12. Monocoque structures combine a monolithic primary structure with the external skin. For cubesats as shown in Figure 1.13 this maximizes internal volume and is easy to produce due to the consistent geometry and dimensions [27].



Figure 1.11: ISISAT cubesat [28]

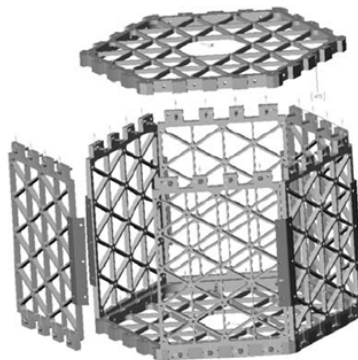


Figure 1.12: Microsat isogrid [29]

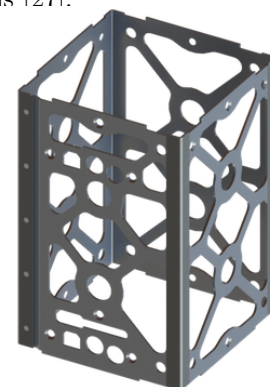


Figure 1.13: Pumpkin Inc. cubesat monocoque [27]

1.4.3. Thermal management

As spacecraft components have a range of allowable temperatures for operation and survival, the generated and stored heat energy must be balanced against the incoming and outgoing heat flux. Externally, panels are designed to be either insulating or radiating as required. Internal heat pathways are included in structural design through the placement and orientation of components. These heat pathways can be enhanced by passive or active thermal control features. According to ESA, common thermal control features in satellites include [30]:

- Reflective foils: Single Layered SLI or Multi Layered MLI.
- Thermal straps: Conductive link for thermal equalization between components.
- Heat pipes: Conductive link for components with high thermal dissipation.
- External coatings: paint or tape with low radiative absorptivity.
- Internal coatings: high emissivity and absorptivity for improved radiative exchange.
- Heating lines: direct thermal control of cold sensitive objects.

Aside from the thermal minima and maxima of components, spacecraft structures must account for thermal gradients and expansion. The thermal gradient between sun facing and shaded sides can cause periodic stress cycles, leading to the aforementioned thermoelastic fatigue. This is common in cubesats, as the limited volume in launch canisters restricts the use of relatively thick insulative materials [31]. Another factor of stresses is the different rate of expansion between materials, which must be accounted for in the interface design [2].

1.4.4. Environmental protection

In the environment of space, the effects of radiation and debris/meteor impacts are considered for the lifetime and reliability of satellites [5]. Effects of radiation on electronics have been mentioned before in 1.2.2, and are accounted for in the component selection of the Lunar Zebro [9].

Concerning micrometeors, the key factors for a satellite or probe are the destination and required lifetime. In a low orbit, debris and micrometeors are more common and impacts as a result more frequent. To some degree, a single structural wall can prevent penetration of low diameter micrometeors. Multiple layers with spacing are significantly more effective, allowing the high velocity particles to dissipate [32]. It is also stated that a multilayer shield with a density close to that of tissue paper is sufficient for most micrometeoroid impacts. This effect is visible in Figure 1.14 below, which compares the penetration resistance of different shield types with identical mass [2].

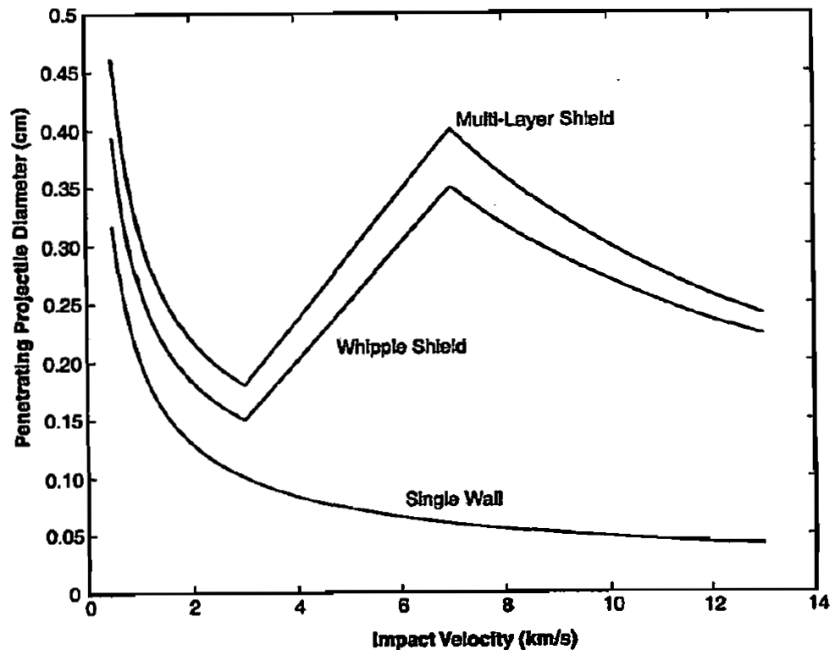


Figure 1.14: Critical meteor size and velocity for shielding [2]

1.5. Lunar Zebro Chassis Design

Due to the limited size of the Lunar Zebro, overall manufacturability and accessibility of components is less complicated compared to macro rovers. The chassis consists of two major parts, namely a monolithic body milled from a single block of aluminium and a composite bottom plate for the installation of components. Aluminium Al7075 T6 has been selected by the Lunar Zebro design team because of its mechanical and thermal properties, manufacturability in complex shapes and low cost.

As the structure of the Lunar Zebro features a frame, base plate and deployment plate it resembles the structural scheme of small satellites [24]. The consistent 1.5mm thickness of the aluminium chassis is also seen in the design of cubesat structures. This makes sense as there is no distinction between planetary rovers and satellites in the structural verification for orbital launch [26].

In its physical shape, the aluminium chassis is designed with the necessary component location in mind. A rendering of the chassis without solar panel, legs and insulation layer is displayed in Figure 1.15. The major box of the body connects to all motor hubs, the solar panel and antenna, while also housing most internal hardware. On the top the chassis has a smaller box structure to provide the cameras with a higher vantage point, while also protecting the lenses from frontal collisions. Behind this structure is the deployment plate which connects the chassis to the lunar landing craft. The insulation foil, not shown in this rendering, covers the entire chassis with cutouts for the leg motor hubs, cameras and deployment plate.

The base plate is entirely flat with some holes for bolt connections, where it attaches to the chassis and internal components. Due to the low shape complexity of the plate a metal fibre ceramic composite material has been selected. This material named CMC is produced by Arceon and has not been applied in extra-terrestrial missions before.

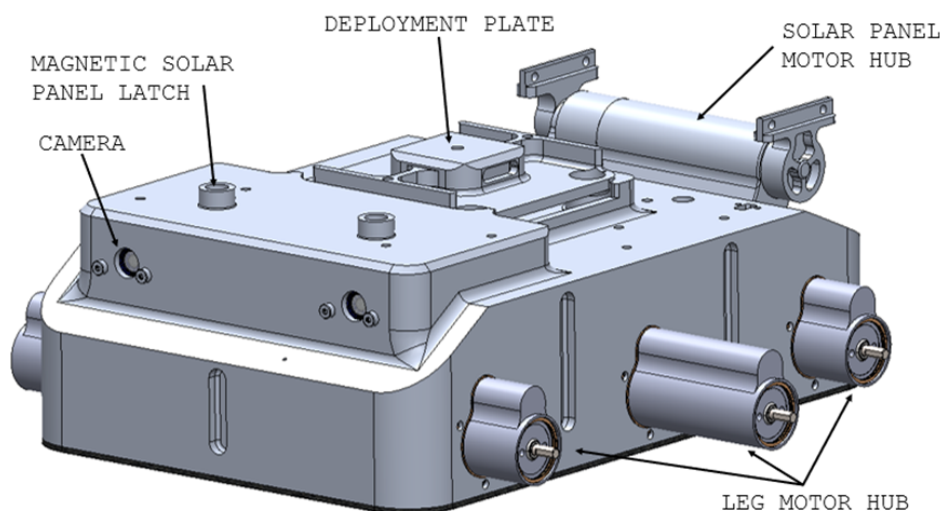


Figure 1.15: Lunar Zebro chassis rendering in SolidWorks

1.5.1. Comparison

From the reviewed rovers and satellites, it is clear that structural integrity in launch and thermal management in operation are the primary concerns defining the structures design. Protection against radiation and micrometeors is less critical for short duration space missions. If needed, these protections can more easily be added at a later stage of development and are as such not critical to initial design of space structures. An overview of the characteristics of reviewed space structures is given in Figure 1.16.

The Lunar Zebro is unique compared to the reviewed rovers with its semi-monocoque body, which functions as the chassis for the locomotion system and WEB simultaneously. Due to this compact design, each motor hub connection is a significant loading point on the chassis. This is the case for both mechanical loads and thermal pathways.

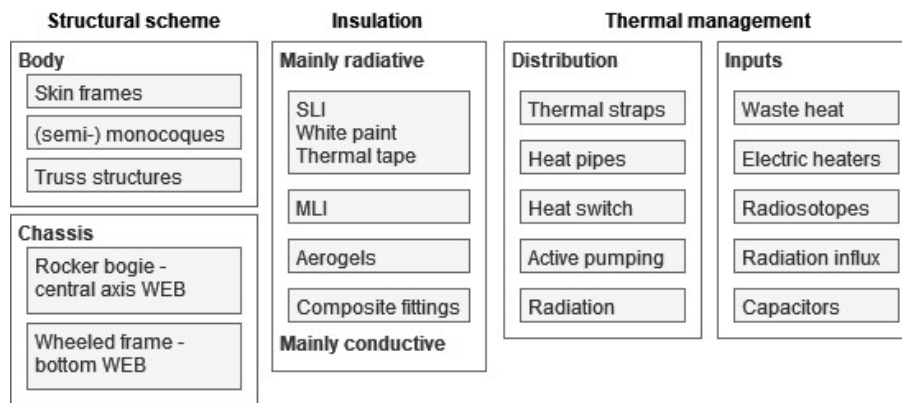


Figure 1.16: Characteristics of planetary rovers and satellite structures

An advantage of the monolithic design of the chassis is the reduction in connection points between structural plates. This makes monolithic structures highly effective in thermal conduction and heat sink properties [27]. However with a consistent plate thickness of 1.5mm, the material usage is not an efficient load bearing design. Other than the material selection, the structural scheme and dimensions of the chassis are scarcely investigated. The limited available time between initial design and necessary certification for launch resulted in a functional but heavy chassis structure.

1.6. Problem Statement

Design of planetary rover structures is a little reported field. There is no public information available on the design or test procedures by which the Warm Electronics Boxes are optimized. The available information concerns little more than material selection and thermal or environmental insulation properties.

Expanding the scope to investigate the design of satellite structures provides more insight. The primary structure is initially designed to resist launch loads and provide adequate thermal transport. A scheme for this loadbearing structure is selected based on the required payload and the benefits of each structure type. An iterative process follows in which the overall design is defined through multiple structural analyses.

In the design of the Lunar Zebro chassis, the main considered requirements were for the rover to function on the Moon. The body is a robust aluminium shell that provides few potential openings for the regolith of the lunar surface, and forms a smooth structure to conduct heat. However there is little investigation in efficient reinforcement design to resist the mechanical loads during launch.

Therefore this research report focuses on the mechanical behaviour of the Lunar Zebro chassis. Methods for designing reinforcement will be investigated to improve the efficiency of material use. The main research question is:

How can the chassis of the Lunar Zebro be redesigned to reduce mass while considering the mechanical requirements for lunar exploration?

This question is answered by the following research objectives:

- Investigate methods for the design of reinforcement structures.
- Analyse the load response of the Lunar Zebro chassis.
- Analyse and test applicable methods for reinforcement design.

2

Research Approach

In this chapter, firstly methods for the analysis and design of reinforcement structures are investigated. Observing the general characteristics of reinforcement structure, the current layout of the Lunar Zebro chassis structure is reviewed. Here potential methods for improvement are discussed, of which a selection is made to define the optimization approach. Finally the selected approach for mass reduction and reinforcement design of the Lunar Zebro chassis is explained.

2.1. Structures design and optimization

In the design of a structure, the optimality of a design can be judged by multiple criteria. In spacecraft design, typical criteria are cost, volume and mass. According to ESA a structure can be considered optimal when one criterium is fulfilled to the best possible extent, provided all design requirements are met [26]. This section introduces analysis methods behind common structure types, translating the basic equations to design logic. Subsequently analysis and optimization methods are investigated.

2.1.1. Structure types

Corresponding to the satellite structures discussed in Section 1.4.2, common reinforcement structures applied in mechanical design include:

- Truss and beam structures
- Monocoques and semi-monocoques
- Skin frames

Trusses and beams

Well known in classical mechanics, truss structures consist of structural members connected in rigid triangular arrays. When connected in a three-dimensional framework of tetrahedrons or pyramids the structure is referred to as a space-frame [33]. A structure of basic trusses assumes all trusses only carry axial loads. In linear elastostatics, a truss follows the basic beam theory for stiffness:

$$K = \frac{f}{\epsilon} \quad (2.1)$$

Where f is the applied load and ϵ displacement per unit length. More complex truss structures can be designed with bending and shear loads as well, expanding the beam theory with the cross sectional geometry. For axial and lateral loads, the beam stiffness expressions are:

$$\text{Tension: } K = \frac{AE}{L} \quad (2.2)$$

$$\text{Shear: } K = \frac{AG}{L} \quad (2.3)$$

$$\text{Bending: } K = \frac{EI}{L^3} \quad (2.4)$$

The load corresponding load conditions are shown in Figure 2.1. In these equations E and G are the Young's and Shear moduli of the material and A the cross sectional area, respectively. The inertia I is discussed in the next section, and can be enhanced by altering the geometry of the cross section.

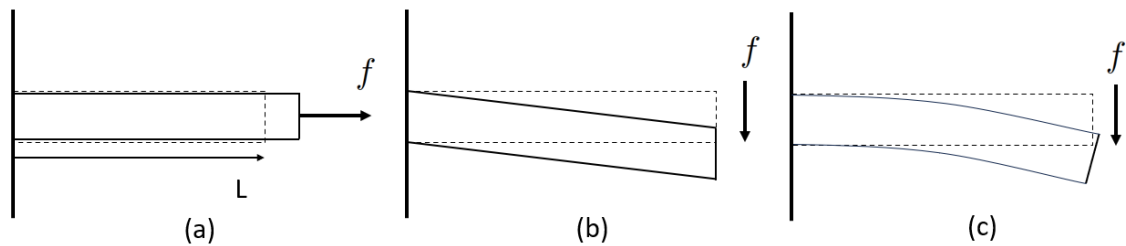


Figure 2.1: Beam deflection in: (a) tension, (b) shear, (c) bending

Semi- monocoques

A monocoque combines the external surfaces or 'skin' with the loadcarrying structure. When the entire external skin forms a continuous structure it is called a 'pure' monocoque design. This is often seen in homogeneous loading scenarios such as pressurised cylinders. When the skin is reinforced by attached stringers or stiffeners it can be classified as a semi-monocoque [2] [5]. These stiffeners can be considered tangent plates which increase the bending resistance of the skin. Consider the inertial properties of a plate section or stiffener cross section as shown in Figure 2.2, bending around the x-axis:

$$I_{xx} = \frac{wh^3}{12} \quad (2.5)$$

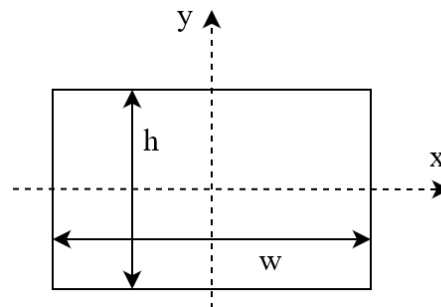


Figure 2.2: rectangular cross-section in the x-y plane

Such plate-based design is common in vehicle design where the external panelling is combined with the chassis. These designs are well suited for modern mass-production manufacturing where plates are easily welded together. When using plates as base components in vehicle design, a significant out of plane load requires reinforcement by a tangent stiffening plate. This plate transfers the load through shear stress into an in-plane point load at an adjacent plate on the chassis, holding the forces in equilibrium. This method forms the base of chassis design by Simple Structural Surfaces [33].

Skin frames

As mentioned in the previous section, skin frames are often seen in design of extra terrestrial structures. Similar to monocoques, a skin-frame structure combines the load carrying structures with the external surface. Skin frames typically form simple geometrical structures as a cube, hexagonal or octagonal tubes where the top, bottom and side panels are designed separately [34]. The panels used are often multi layered sandwich panels which have improved bending resistance over thin plates. Additionally the multi layered design can improve other properties of a structure such as the thermal insulation.

Compared to a solid plate, sandwich panels have a limited resistance to concentrated loads. The connecting interfaces for components and payload must distribute loads appropriately, or a reinforcing structure is applied. Sandwich panels are analysed by composite plate theory as shown in Equation 2.6, which relates the stresses and moments resulting from the interaction of multiple material layers.

$$\begin{bmatrix} \bar{N} \\ \bar{M} \end{bmatrix} = \begin{bmatrix} A & B \\ B & D \end{bmatrix} \begin{bmatrix} \varepsilon^0 \\ \kappa \end{bmatrix} \quad (2.6)$$

Here ε^0 denotes the strain on the midplane of the laminate plate. The A matrix gives the contribution of plane strains ε on stresses \bar{N} , and D the curvature κ on bending moments \bar{M} . B is the coupling stiffness matrix, which couples plate bending to in plane stresses generated in the laminate plate.

2.1.2. Modelling methods

In Finite Element Analysis for solid structures, a structure is partitioned in a mesh of elements connected by shared nodes. The complete mesh of connected nodes and elements is used to discretize a structure, for example by its stiffness $[K]$ or mass $[M]$. With this the structural deformation resulting from an applied force \mathbf{f} or acceleration $\ddot{\mathbf{q}}$ can be calculated:

$$[M] \{\ddot{\mathbf{q}}\} + [K] \{\mathbf{u}\} = \{\mathbf{f}\} \quad (2.7)$$

The resulting displacement array \mathbf{u} defines the local strain between nodes, from which stresses are derived. Through similar discretizations, FEA software is applied in space structure verification for thermal analysis, modal and vibration response, among many other analysis possibilities [5]. As these analyses are dependant on geometrical and computational simplifications, there are methods to ensure the validity of the analysed model:

- Convergence analysis: Analysing the structure with a more fine mesh to ensure the result changes gradually and the rate of change decreases
- Comparative studies: Performing a similar analysis with other element types or a different modelling software.
- Physical testing methods, examples discussed in Appendix A

2.1.3. Optimization methods

There is much recent research in computer models to optimize material allocation subject to one or multiple loads. This can serve as inspiration for generating an improved support structure, or it can optimize the exact dimensions of a part. This section discusses some examples of optimization models applied in design of reinforcement structures.

Size optimization

Sizing optimization algorithms work by exclusively increasing or decreasing material allocation within specified boundaries. This aims to find the optimal distribution of material in a predefined plate or truss structure. An example of size optimization is shown in Figure 2.3. Here a sizing optimization is the preceding step in a study for stiffener placement optimization.

Shape optimization

A size optimization study can be expanded by modifying the existing geometry and element properties. This is the basis of shape optimization [35]. Contrary to Topology Optimization, shape and size optimization algorithms are not capable of creating holes or new connections in the geometry.

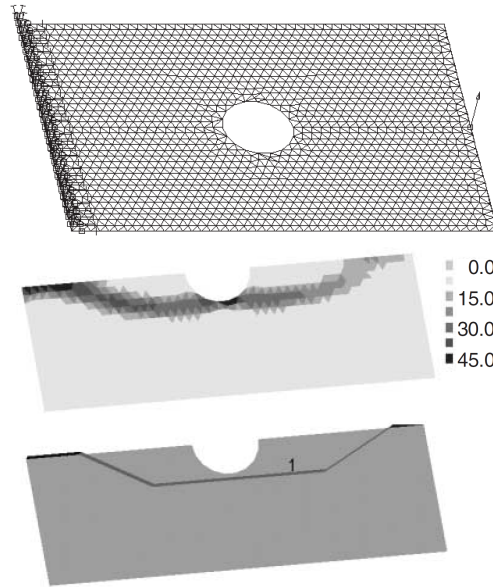


Figure 2.3: Size optimization and rib placement optimization [35]

Topology Optimization

Topology Optimization (TO) is the least bounded in the geometries generated by the algorithm. The capability of TO is limited by the complexity of the design loads and computational power. Results from a TO study can be used to directly define the geometry of a structure, or serve as inspiration in the design process. Two examples are discussed here.

A TO model can directly optimize for mass, for example when bounded by a stress limit. Here material is allocated near high-stress areas and removed where possible. Furthermore the supporting properties of other components can be incorporated with the loadbearing structure, as shown in Figure 2.4 below.

Alternatively the model may have a defined amount of material to distribute, optimizing for minimal stress to define critical loading areas. This method has been applied in the Multi-Objective TO of a satellite base plate structure, combining the launch acceleration load and random vibration response [36]. The result of this optimization study is visible in Figure 2.5. This result was supplementary to the selection of a stiffener grid layout in the design process.

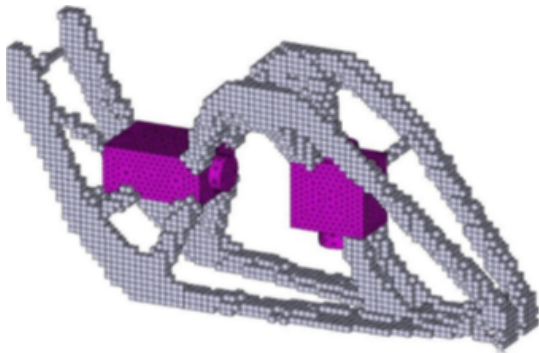


Figure 2.4: Helicopter pylon, Multi-component TO [37]

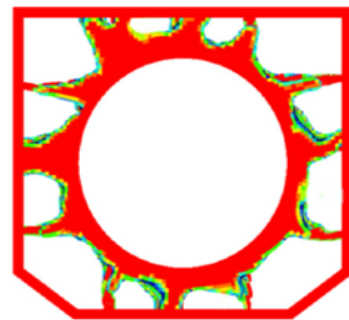


Figure 2.5: Topology Optimization with static and dynamic loads [36]

2.2. Lunar Zebro chassis design

The design approach applied by the Zebro Team is arguably identical to the Concurrent engineering approach. A functioning rover has been produced in a relatively short time, meanwhile various parts of the design are still being analysed and improved. Parallel research occurs among design teams while the affected aspects are codependent for the performance of a finalized design.

This section firstly investigates the setup of the current chassis structure. The design choices that lead to this configuration, shape and design scheme are considered. Secondly this section discusses potential methods for redesign of the chassis structure. Finally the selected approach for the mass optimization study is explained.

2.2.1. Chassis structure configuration

The monolithic aluminium body and CMC bottom plate are connected by a set of six long bolts which span the full height of the chassis. This forms a very rigid structure that carries all loads during launch. The bolts that hold the internal electronic boards, hereafter called the PCB stack, are neglected in the stress analyses conducted for the chassis. This PCB stack and other structural components are shown in Figure 2.6.

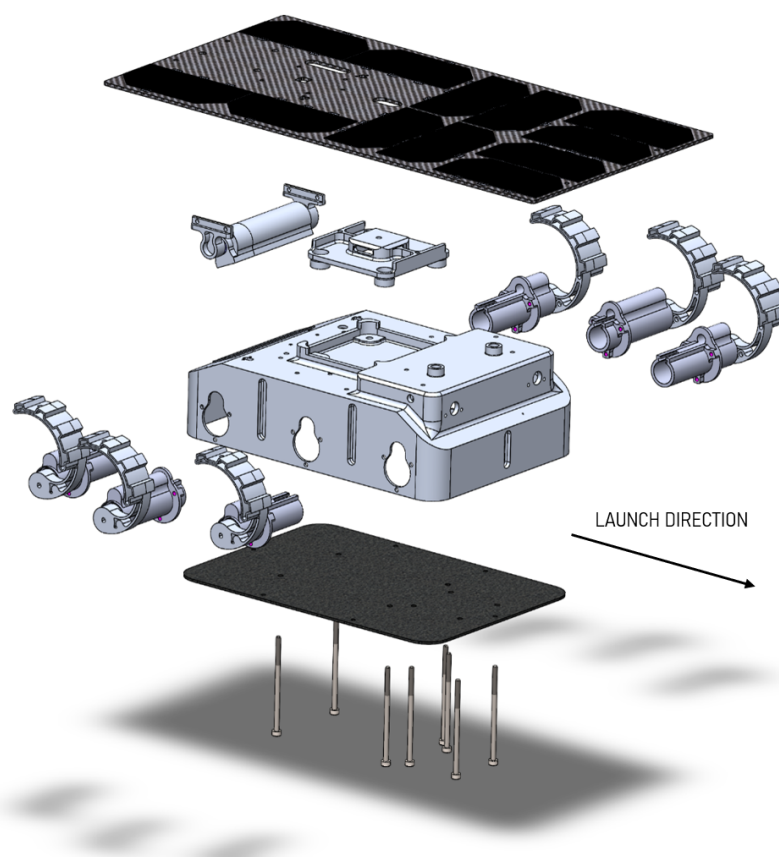


Figure 2.6: Lunar Zebro Structure exploded view in SolidWorks

In the design of spacecraft structures according to [5], the configuration of the structure is determined in the first design phase. Here the launch vehicle requirements, e.g. attachment method and mass budget, and the functional mission requirements are considered. The first design of the spacecraft structure follows, analysing the design loads and stiffness requirements in more detail. Subsequently the scheme and sizing of the support structure is defined.

For the Lunar Zebro chassis, these design phases were not strictly followed. The structural scheme is a combination of shell and beam structures. This scheme was selected due to the requirements for Lunar exploration, mainly focused on thermal conductivity and sealing against regolith. A review of the design choices of the Lunar Zebro chassis is shown in Appendix B. This shape and scheme were defined with little consideration of the design loads for space launch.

2.2.2. Chassis design requirements and methods

The objective is to reduce the total mass of the Lunar Zebro structure with the current mission profile. This can be achieved in many ways. An overview of the design process and considerations, as discussed in Section 1.4, are shown in Table 2.1 below.

Design Phase	Considerations
Structural requirements	<i>Withstand launch:</i> - Static loads up to 8G - Vibrations - Shocks ranging from 100-1000G <i>Mission requirements:</i> - Seal regolith - Act as heatsink - Thermal transport for steady-state behaviour - Survive thermal cycling from -180°C to 120°C
Shape selection	Leg spacing Solar panel attachment, movement range Camera position Lander attachment Components housing and assembly
Scheme selection	Monocoque: Current design, carries loads externally Truss structure: Carries loads internally, lightweight skin required Space frame: Carries loads externally, forms skin and insulation
Primary structure definition	Material selection: Metals, fibre composites, mixed skin-frames Initial sizing s.t. Structural requirements
Internal/External connections	Reachable during assembly Must maintain seal s.t. (thermo)mechanical loads
Secondary structure definition	Solar Panel Antenna Leg Module assembly
Analysis/verification	Does not yield to static/dynamic loads Composites: verify for delamination, fiber microbuckling Thermal: steady state temperature model analysis

Table 2.1: Chassis design process: overview of considered requirements, aspects and possibilities

A redesign of the structural scheme with composites is likely to obtain considerable weight savings. Composites provide an estimated 38% weight reduction when replacing an identically rigid aluminium plate [38]. It can be supported by a skeletal aluminium substructure for component attachment and thermal transfer, similar to the skin-frame satellite design discussed in section 1.4.2. However this design strategy comes with increased complexity in:

- Thermal deformation and Steady-State behaviour
- Manufacturing methods
- Material risks, e.g. delamination, fibre microbuckling, crippling
- Testing and certification requirements

While skin-frame structures are more common in all recent rover missions, this is most likely due to the size of these rovers. Production of a monolithic structure is logically more difficult with increasing size, hence monolithic satellite structures are seen in comparatively smaller cubesats.

Due to the many unknowns surrounding the current design and future state of the Lunar Zebro, the current structure and loading conditions should be investigated further before committing to such a redesign. Furthermore, obtained knowledge in load behaviour and reinforcement effects of the current chassis structure is beneficial to a future redesign with composites.

2.2.3. Chassis optimization approach

As the Lunar Zebro is designed by student teams, the timespan of design projects is relatively short. There is much uncertainty concerning the launch date and the lunar lander that may transport the Lunar Zebro. Therefore any future design may differ from the current situation in many ways. Suggested improvements to the current design may even be irrelevant by the end of this research project, or soon thereafter. Due to these uncertainties and the complexity of the design problem, the scope in this research project is limited to reinforcement design for equal stiffness on the current chassis structure.

A case study will be performed based on the current design of the chassis. This case study maintains the configuration and material choice to minimally affect the various mission requirements. Methods for the design and placement of reinforcement are tested while maintaining the stiffness of the chassis. Considered aspects for each design phase are displayed in Table 2.2 below. By analysing the structure in a less detailed way, the investigated reinforcement design methods can more easily be included when the chassis design is altered in the future.

Design Phase	Considerations
Structural requirements	Design for equal stiffness has minimal effect on other requirements
Structural shape selection	Will be evaluated and simplified during analysis/modelling
Structural scheme selection	Not adjusted, recommended for future study
Primary structure definition	Methods for efficient reinforcement design will be tested
Internal/External connections	Connections simplified, sealing not evaluated
Secondary structure definition	Not considered
Structural analysis/verification	Necessary verification of reinforcement methods will be indicated

Table 2.2: Chassis design phases: considerations for selected design approach

Computer based optimization programs have potential, but are either too easily invalidated by alterations in the design requirements, or too complex to feasibly realise. General load analysis and reinforcement tests in FEM presents potential in some short term mass reduction, and a lot of supplementary knowledge to any redesign or optimization study.

The approach that was originally planned would include thermal analysis in the FEA model. Afterwards the feasibility of replacing external plating with composite materials would be investigated. The acquired knowledge in load analysis and reinforcement design would be essential to support these research steps. Due to time constraints for this thesis project, this report is limited to the analysis and design of reinforcement against static mechanical loads.

2.3. Chassis reinforcement design strategy

In the current design, the Lunar Zebro chassis is a robust monocoque structure. The plates are relatively thick with no supporting substructure. As this is not an efficient loadbearing design, this report investigates methods for rib reinforcement design on thin plates. A case study is performed to analyse the behaviour of the chassis structure and test methods for rib reinforcement design. This case study is performed in the steps shown in Figure 2.7 below.

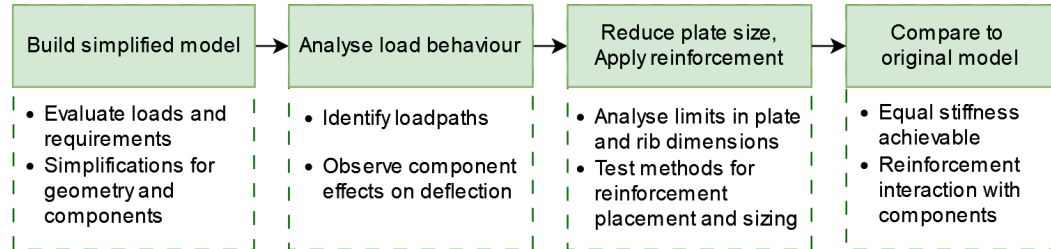


Figure 2.7: Structure modelling and design approach

Based on the results of this case study, the more effective methods for rib design are investigated further towards the end of this report. This section explains the configuration of the analysed chassis model and the approach for reinforcement design.

2.3.1. Case study model setup

The geometry of the simplified chassis model is shown in Figure 2.8 below. This model maintains the size, attachment plate and PCB stack connections of the original chassis. Additionally the local masses of the Leg Module Assemblies are included. As discussed, the connections and shape of secondary structures are strongly simplified. The following aspects are adjusted:

- Chassis shape: rounded corners, sloped front/back geometry removed
- Bottom Plate: simple aluminium plate, rigid link to chassis walls
- Camera hub and Solar Panel Assembly removed.

Making the camera hub an external structure is a design feature seen on all deployed planetary rovers. This is potentially beneficial to the thermal steady-state design [30]. Further research to this design feature is recommended. Removing the camera hub from the top of the chassis has several benefits:

- Easier CNC production
- Possible vacuum bed support during CNC milling, reducing the plate thickness limit
- Easier insulation design and manufacturing

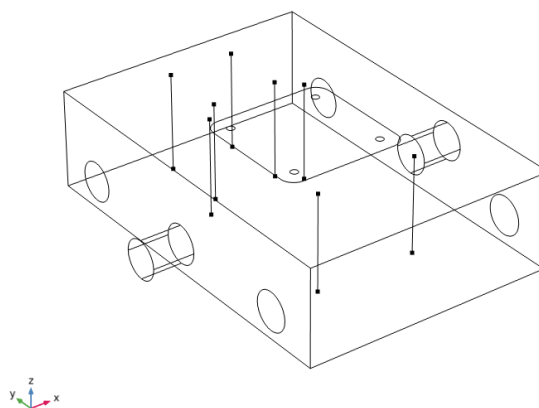


Figure 2.8: Chassis Model in COMSOL Multiphysics

2.3.2. Case study design loads

By designing the reinforcement for equal stiffness to the original situation, it is assumed the response to other loads is minimally affected. The orientation for launch is not definitive and vibrations can occur in any direction. Therefore the chassis should maintain its stiffness to all load directions. This method for reinforcement design concerns the design requirements of the Lunar Zebro as shown in Table 2.3.

Requirement Category	Description
<i>Functional</i>	Provide housing for all electronics and the payload
	The internal volume is not reduced by applied geometrical simplifications. Dimensions of reinforcements will be specified
<i>Performance</i>	Withstand acceleration loads, 8.5G axial and 4G lateral
	A combined acceleration vector of 10G is used in each principal direction. Deflections will remain similar, effect on stresses will be reported
<i>Performance</i>	Have a first harmonic frequency greater than 100 Hz
	A requirement for launch in ESA documentation [26]. When designed for equal stiffness but reduced mass, harmonic frequencies increase.
<i>Performance</i>	Survive enough thermal cycles ranging between -180C and 120C
	Thermal stresses and fatigue are not considered. Essential to analyse in future study.
<i>Environmental</i>	Survive micrometeoroids weighing 10 mg travelling at 18km/s
	Increasing the spacing of the external insulation is likely the most efficient approach. An investigation of the likelihood and effects of an impact event is recommended.

Table 2.3: Structure Loads from Lunar Zebro Structure documentation [39]

After observing the load response from the simplified model, different approaches for reinforcement design are tested. As the plate thickness is reduced, stiffening ribs are applied. By reducing material use in a structure while maintaining the same load response, the increase in observed stress should be proportional to the reduction of mass. Though this can differ strongly depending on the load scenario and improperly distributed reinforcement. Aside from the mentioned design requirements in Table 2.3, the following aspects should be analysed before applying ribs to a definitive design:

- Nonlinear buckling behaviour
- Local peak stress magnitudes
- Thermal gradients in the structure, deformation of ribs

2.3.3. Reinforcement design approach

By applying a static acceleration load in each principal direction, one can observe if any applied reinforcement is disproportional. A noticeable decrease in deflection in one direction suggests that the reinforcement is excessive. This likely results in concentrated stresses which can cause permanent deformation or cracks. The approach at rib reinforcement design used in the Zebro chassis model analysis is shown in Figure 2.9.

By including additional components after the initial load analysis, the rib design method for is tested in two aspects. Firstly it can be concluded if the method for rib design is suitable for both simple and complex structures and load setups. Secondly this approach allows to analyse how the ribs interact with the selected components specifically. If the reinforced models behave significantly different from the plain plate model when including additional components, the ribs design may need to be adjusted. The necessity and complexity of these adjustments will be discussed for each tested method of rib design.

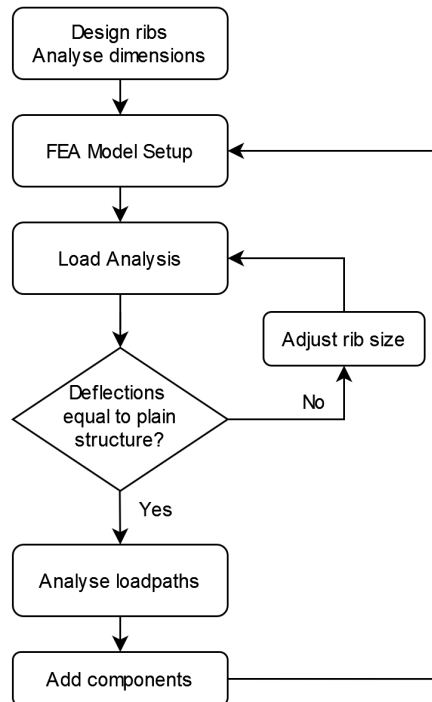


Figure 2.9: Reinforcement design approach diagram

3

Chassis Modelling

In this chapter, the case study for lightweight reinforcement design with ribs is performed as explained in Chapter 2. The objective is to identify methods for rib design suitable for the unique loading scenario of the Lunar Zebro, while maintaining the stiffness of the global structure. Firstly the modelling methods are investigated, verifying the accuracy of the applied FEM tools for thin plates and reinforcement in COMSOL Multiphysics. After that the load response of the chassis model is investigated. With this as a baseline, different design methods for rib placement are tested.

3.1. Ribs modelling verification

The selected approach to reinforcement design and modelling involves performing multiple analyses with minor adjustments. As such the objective is to build a model that runs in a relatively short amount of time. This way it is possible to rapidly run multiple tests with minor modifications to the model, where the effects and interaction of these modifications can be observed. In order to fairly compare the generated models they must be equally accurate. Therefore the modelling errors and discretization errors should be taken into account.

Discretization errors originate from mathematical simplifications and computational limitations. In this section, the accuracy of COMSOL shell elements is compared to those of other software packages. The number of evaluated Degrees Of Freedom is in the same order to accurately compare these element types.

Modelling errors arise from the geometrical simplifications and element selection. In this report both shell and beam elements are applied to model plates with small stiffeners. This method reduces the difficulty of the model setup, and allows to use a more coarse mesh. An overly coarse mesh of small stiffeners could cause a significant increase in the discretization error. This section compares the behaviour of the shell stiffeners to that of beam elements linked to a parallel plate with the COMSOL Multiphysics coupling.

3.1.1. Shell deflection comparison

First an example study from literature is recreated in COMSOL to ensure the model setup is done correctly. The configuration of the example analysis is shown in Figure 3.1. One is a simple square plate subjected to a pressure load and the second includes large stiffeners and a point load. The parameters of these analyses are given in appendix C.

The example study compares the triangular CTRIB3 element from the TU Delft Charles environment to the quadrilateral Shell181 elements of ANSYS. The COMSOL model uses quadrilateral MITC9 elements. This element type contains nine nodes with six Degrees Of Freedom (DOFs) per node. This is significantly more than the CTRIB3 and Shell181 elements, which have 12 and 24 DOFs per element respectively [40]. As the example study displayed the deflection in the centerpoint $w[m]$ over total number of elements instead of DOFs, these values are converted to graph a more accurate comparison. The calculation for this conversion is shown in appendix C.

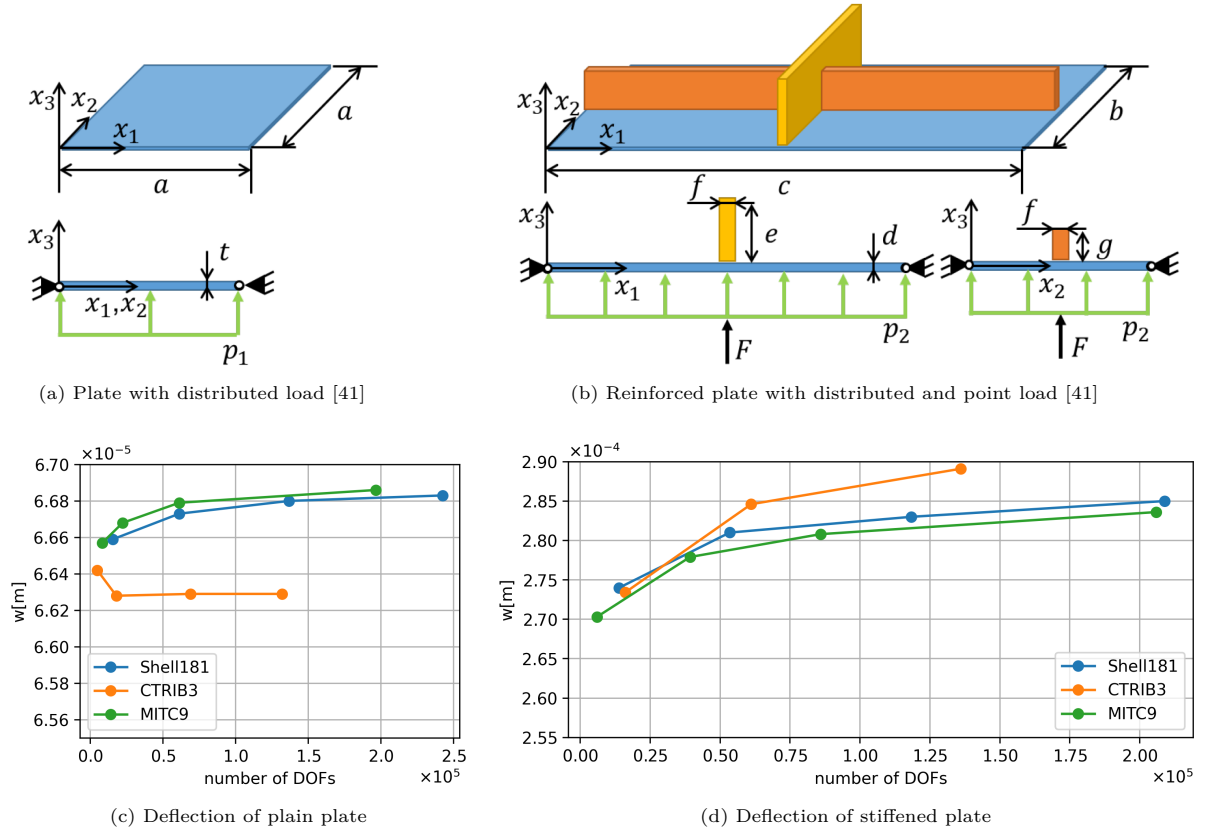


Figure 3.1: Comparison of three shell element types in a plain plate and stiffened plate

3.1.2. Shell-Beam element interaction

COMSOL Multiphysics has the functionality to model stiffeners as beam elements on a plate with a virtual offset. Modelling with beams as stiffeners has two potential benefits. Firstly the difficulty in model geometry setup is reduced. Secondly when analysing small stiffeners, the permissible minimum mesh size is increased without poor shaping of the stiffener elements. The nodal displacement of a beam \mathbf{u}_b can be described by the nodal displacement of the attached shell \mathbf{u}_s and offset \mathbf{d}_0 as follows:

$$\mathbf{u}_b = \mathbf{u}_s + (\mathbf{d}_0 \cdot \mathbf{n})\mathbf{a} \quad (3.1)$$

Where \mathbf{a} is the change of the shell normal vector \mathbf{n} . These parameters also define the nodal rotation of the beam θ_b as:

$$\theta_b = \mathbf{n} \times \mathbf{a} \quad (3.2)$$

As beam elements are only evaluated at their nodes on the midpoint, some accuracy is inherently lost compared to an analysis with properly sized shell elements. This is especially true for relatively large stiffeners as those in the analysed example of the previous section. When analysed in COMSOL with a similar number of DOFs, the model with beam elements converges to a lower deflection as shown in Figure 3.2 (a). This means that the stiffness of these large beams is excessive when interacting with adjacent shells.

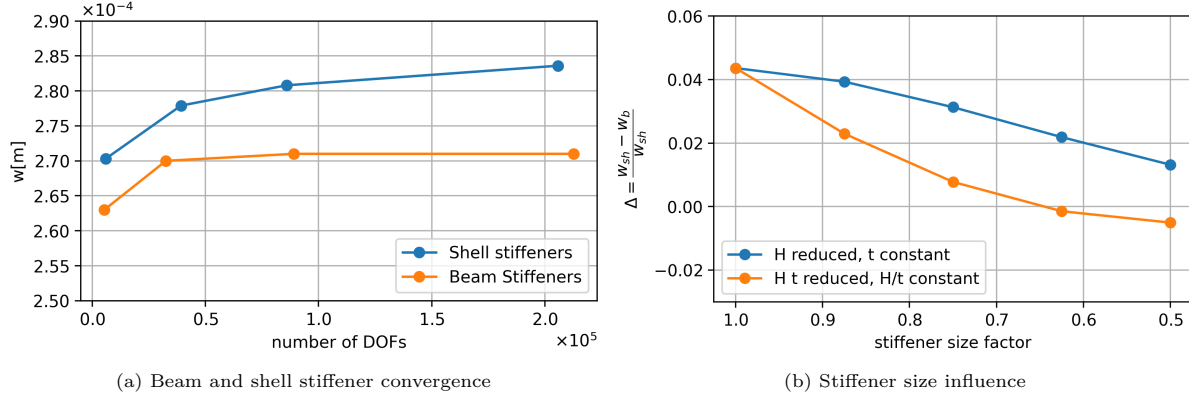


Figure 3.2: Comparisons of beam and shell elements as stiffeners

The analysed model considers stiffeners that are relatively large compared to the plate they support. This is not necessarily the case for thin plate reinforcement. As the shell elements in COMSOL perform very well, another test is carried out to compare shell and beam elements with a smaller stiffener size. In this test the configuration is identical to that in the previous section, while the size of the stiffeners is incrementally reduced to half the original size. The element size is kept constant with a total number of DOFs in the order of 200,000. As the provided support decreases, the peak deflection increases rapidly. To accurately compare the difference in performance of the beam and shell elements, the difference in deflections is normalised as follows:

$$\Delta w = \frac{w_{sh}[m] - w_b[m]}{w_{sh}[m]} \quad (3.3)$$

Where w_{sh} and w_b are the evaluated centerpoint deflections of the shell- and beam stiffened plates respectively. As the reinforcement provided by the stiffeners decreases, the difference between these models reduces as well. In one comparison the height of both stiffeners H_g and H_e is halved while the thickness t is kept constant. In the other the height and thickness both reduce at the same rate, maintaining the slenderness H/t of the stiffeners. This effectively reduces the volume of the stiffeners by 75%. The results are shown in Figure 3.2 (b) and in Appendix C.

As the mesh size is kept constant, the number of shell elements over the stiffener height reduces with the size of the stiffeners. Therefore the discretization error of this model gradually increases. When the slenderness of the stiffeners is kept constant, the evaluated deflection of the beam model becomes larger than that of the corresponding shell model. This shows that the selection of beam or shell elements is not critical when analysing the deflection of a plate with small stiffeners.

3.2. Simplified Chassis Analysis

A simplified chassis model is built based on the design of the Lunar Zebro. In this section the characteristics of the model are explained. A static load analysis is performed to identify the stress pathways, as well as the effects of the included components on the load behaviour. This defines the baseline deflections that the reinforced models will be compared to.

To ensure accuracy of the comparison, the model analysis is performed with slightly higher and lower mesh refinement. The model is sufficiently accurate if the resulting deformation does not change significantly.

3.2.1. Model setup

As discussed in the design approach, the chassis FEA model is a simple box structure fixed at the attachment plate. Here it is pinned at all bolt holes, thus assuming the attachment plate is fully rigid. The dimensions of this model geometry are shown in Appendix D. The model as shown in Figure 3.3 contains the following aspects:

- Boundary conditions: Pinned bolt holes.
- Attachment Plate ribs: Beam with offset, 6x3mm.
- PCB Stack connectors: Rigid beams, M3 diameter.
- Leg Module Assemblies (LMA): Mass per unit area.

Table 3.1 shows the essential parameters of the chassis model. For the LMA's the center of gravity is calculated based on the components masses, assuming a homogeneous mass distribution in each component. This calculation is shown in Appendix D. For the corner LMAs this offset is negligible. To model the additional torque of the middle LMAs, two solid cylinders are added with a density of 1g/m^3 as zero density is not possible. This raises the added mass per unit area to the proper offset height from the chassis walls.

<i>Parameter</i>	<i>Description</i>	<i>Value</i>	<i>Unit</i>
L	Length (Y axis)	197	mm
W	Width (X axis)	137	mm
H	Height (Z axis)	53	mm
T	Plate thickness	1.5	mm
T	Baseplate thickness	1.0	mm
Lc	Mass per unit area, corner leg modules	243.4	Kg/m ²
Lm	Mass per unit area, middle leg modules	244.8	Kg/m ²
E	Youngs modulus AL7075 T2 (COMSOL)	71.147	GPa
ν	Poisson ratio AL7075 T2 (COMSOL)	0.33125	-
G	Global acceleration load ($10 * g_{const}$)	98.066	m/s ²

Table 3.1: Baseline model parameters

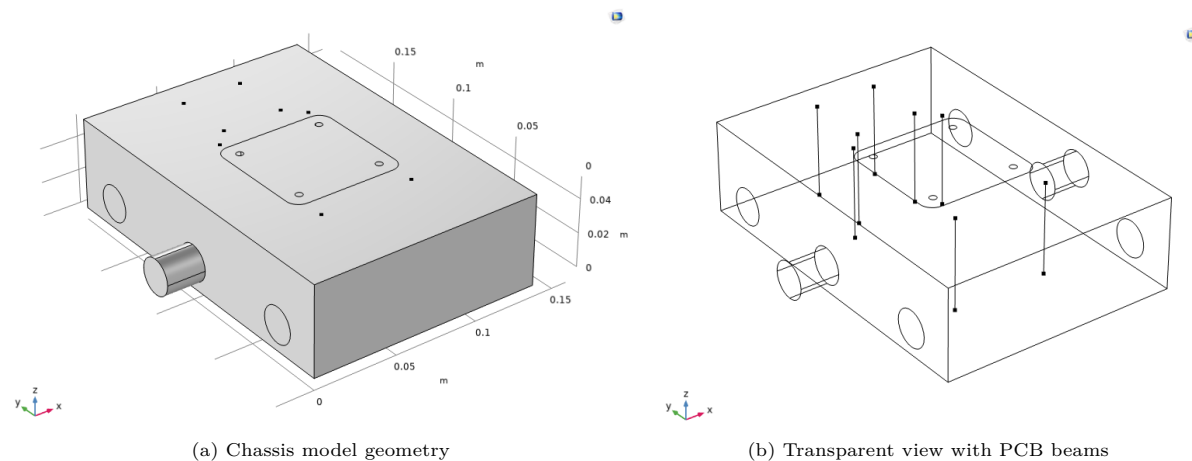


Figure 3.3: Chassis Model in COMSOL Multiphysics

The mesh generated by COMSOL Multiphysics version 6.1 is shown in Figure 3.4 on the following page and is generated with the following settings:

- Beam Elements (Timoshenko): Attachment plate edges, PCB stacks
- Quadrilateral shell elements: Front and rear sidewall
- Triangular shell elements: LMA, attachment plate, sidewalls, top and bottom plate

- Solid Tetrahedral elements: Middle LMA Cylinders

The mesh refinement is set to Extra fine for all shell and beam elements on the chassis plates. To improve computational efficiency, the LMA mesh is less detailed as these function solely to transfer loads to the chassis. The solid leg cylinders have Normal refinement and the corner LMAs are meshed as Extra coarse.

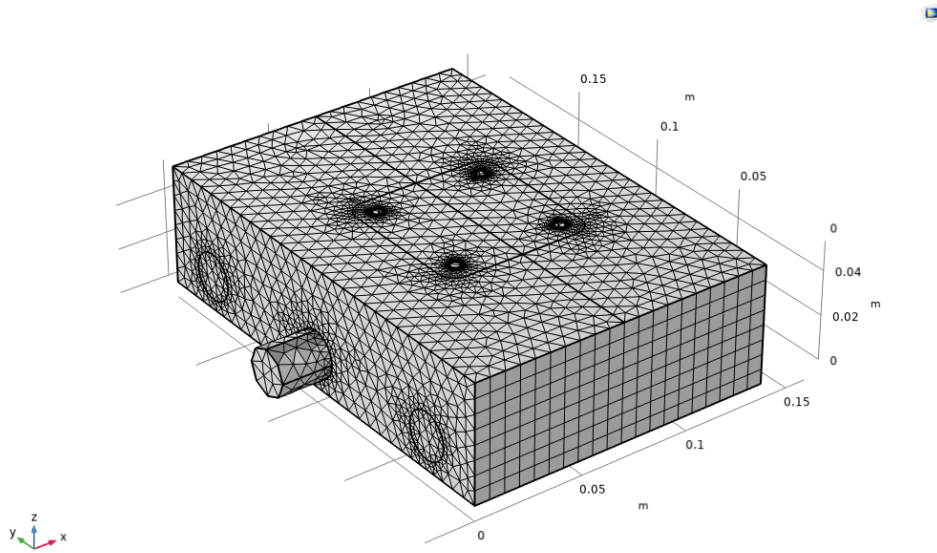


Figure 3.4: COMSOL Chassis Model Mesh

<i>Element type</i>	<i>Nr. of elements</i>
Domain elements	967
Boundary elements	7172
Edge elements	689

Table 3.2: Elements in baseline FEA model

This model is subjected to full body acceleration loads as shown in Figure 3.5. For the boundary conditions, the model is pinned at all bolt holes in the attachment late. The orientation for launch is not definitive and vibrations can occur in any direction. Therefore the chassis stiffness should remain similar in all load directions.

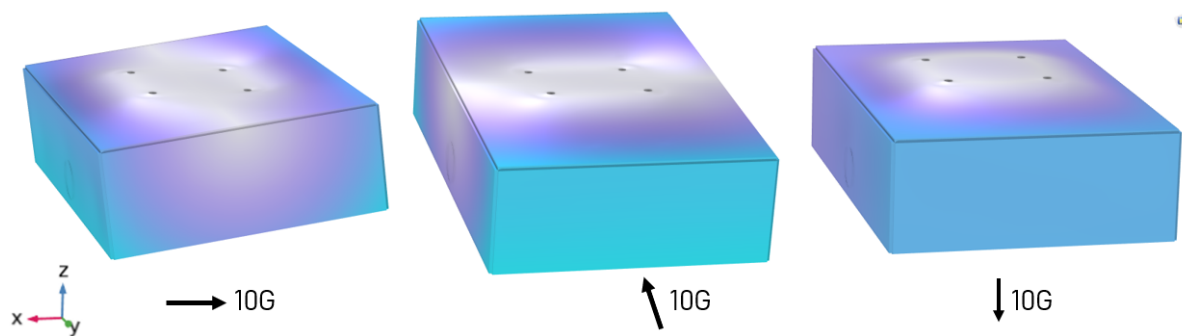


Figure 3.5: Chassis model full body acceleration loads

3.2.2. Chassis deflection analysis

As discussed in the test approach in Section 1.4.1, the plain model is analysed first without any attached components. The stress response of a 10G full body acceleration is shown in Figure 3.6.

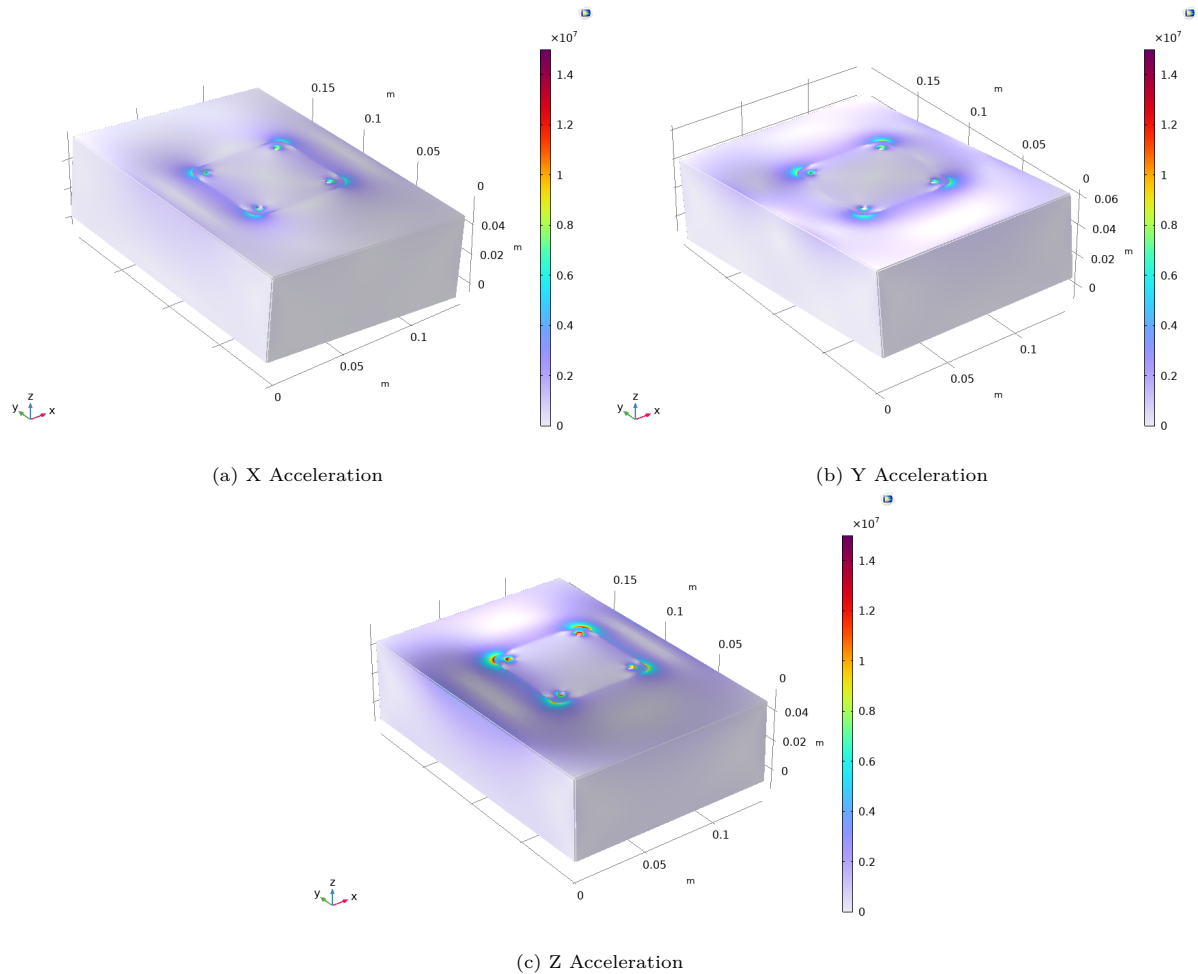


Figure 3.6: Plain model stress analysis in COMSOL

All graphs have a deflection scale factor of 150. A first observation from this model is that, despite the lack of attached components and masses, there are considerable stress concentrations at the attachment plate corners. The importance of rounding and stress distribution here is clear. Also the acceleration in the X and Z directions cause visible deflections and stresses propagating in the sidewalls.

The necessity of a reinforcing substructure can not be concluded as this model lacks critical details. The support provided by the baseplate connection bolts, the rounded corners of the chassis, but also the added load by the leg modules on the sidewalls need to be considered.

Note that during luring launch, all these accelerations can occur simultaneously and periodically. In the current design, the launch direction and main acceleration load is the Y direction. The X and Z accelerations are still considered in the design for equal stiffness, though the load responses are not displayed in the following tests. This is because most aspects of the load response behaviour can be observed from the Y-acceleration response. The resulting deflection responses of all model analyses are displayed in the referenced appendices.

Including the components as displayed in the previous section, the resulting stress response of the chassis model are shown in Figure 3.7. Note that the range of the stress magnitude is higher than that in the plain model above.

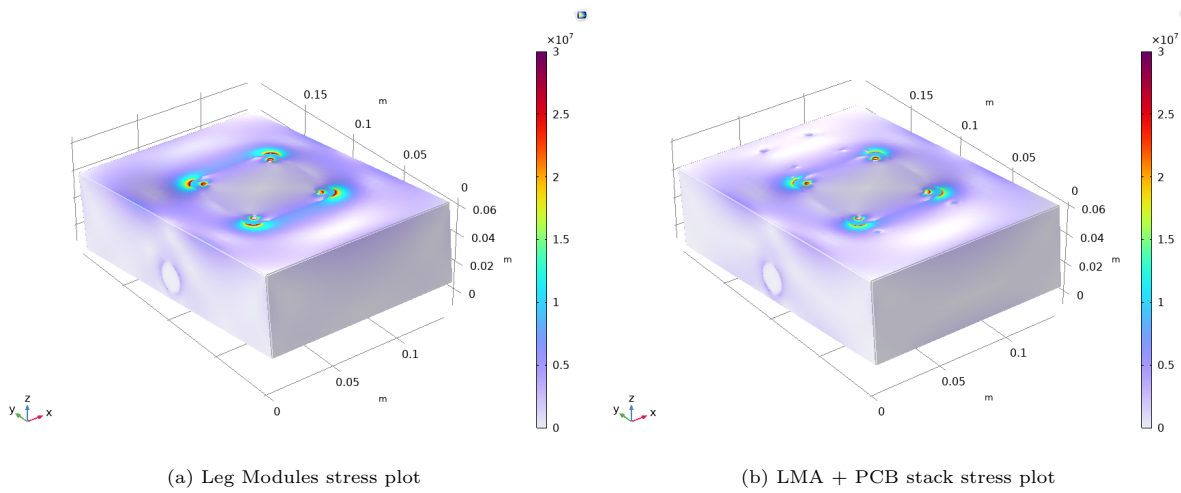


Figure 3.7: Stress response to Y acceleration with Leg Modules and PCB stack in COMSOL

In both these graphs the deformation scale factor is reduced to 50. When the leg masses are included, the deflections and stresses increased significantly but the stress pathways on the top plate are hardly affected. As such the effect of the Leg Module Assemblies on global deflections is limited. The most notable difference is the appearance of stress regions on the sidewalls. Here the torque generated by the middle leg modules should not be ignored.

Adding the PCB stack connection between top and bottom plate increases the stiffness of the chassis. Figure 3.7b shows a reduction in average stress in the top plate, with smaller stress concentrations near the attachment plate. The reduction of deflection is more clearly visible in Figure 3.8 below. This graph shows the deformation of the centerline from the neutral position, in response to the launch (Y-axis) acceleration. Thus it can be said, assuming the PCB stacks form a rigid link between the top and bottom plate, these connections have a major effect on the load response of the chassis.

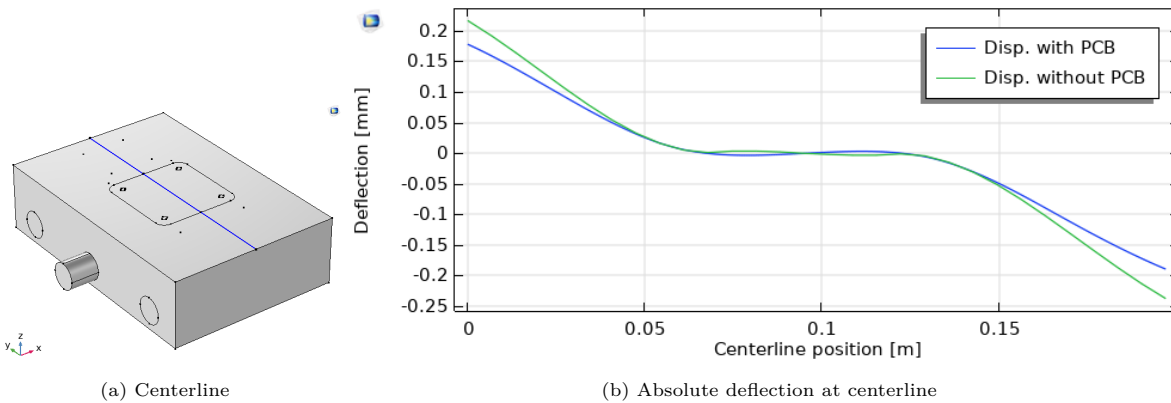


Figure 3.8: Effect of the PCB stack on chassis deformation in Y acceleration

3.3. Reinforcement Design Test

In this section the constructed chassis model is subjected to multiple tests for rib design. Firstly, requirements and limitations for rib design are investigated. This also provides analysis methods for structure sizing in the subsequent modelling and testing. The tests evaluate if manual stiffener design methods are effective, and also provide insight in design aspects that are critical during the design of a reinforcement structure.

3.3.1. Stiffened plate design

For the initial tests of reinforcement design with equal deflection, the following aspects are considered:

- Placement: Aligned with major load points on structure, discussed at each test setup.
- Sizing: Production limitations CNC milling.
- Sizing: Linear buckling limitations.
- Shape: Homogeneous rectangular ribs. No flanges or tapering.

Production limitation

The most lightweight plate has a thickness approaching zero, which is of course impossible in mechanical applications. By taking the production method of CNC milling as limitation, the resulting lightweight design can be compared to the existing model.

With common modern production methods, a CNC lathe can produce a thin wall of 300 x 50 x 0.3 mm only fixed at one long edge to the 0.3mm thickness [42]. The measured thickness had outliers of 0.322mm and 0.289mm respectively, with most measurements in the 0.308mm and 0.314mm range [42]. Since the Lunar Zebro chassis walls are shorter and more constrained by adjacent chassis walls, the potential error range can be lower. A minimal thickness of 0.3mm is maintained in this report with no error margin. For a definitive design, the production error should be accounted for.

Buckling limitation

To maintain realistic rib dimensions, linear buckling scenarios as shown in Figure 3.9 are considered. The Euler buckling assumption is evaluated for both axial and shear loads. These design tests assume the beam is free along its length, ignoring contribution of the plate. This is a very conservative approach and thus inefficient [5], though it is sufficient for an initial test of reinforcement design. For plate buckling, all edges are either pinned or fixed depending on the ribs size as will be discussed at each test. The applied equations from [5] [43] are:

$$F_{C_Euler} = C \frac{\pi^2 EI}{L^2} \quad (3.4)$$

$$F_{C_shear} = 0.41 \frac{hb^3 E}{L^2} \sqrt{1 - 0.630 \frac{h}{b}} \quad (3.5)$$

$$\sigma'_x = K \frac{E}{1 - \nu^2} \left(\frac{t}{b} \right)^2 \quad (3.6)$$

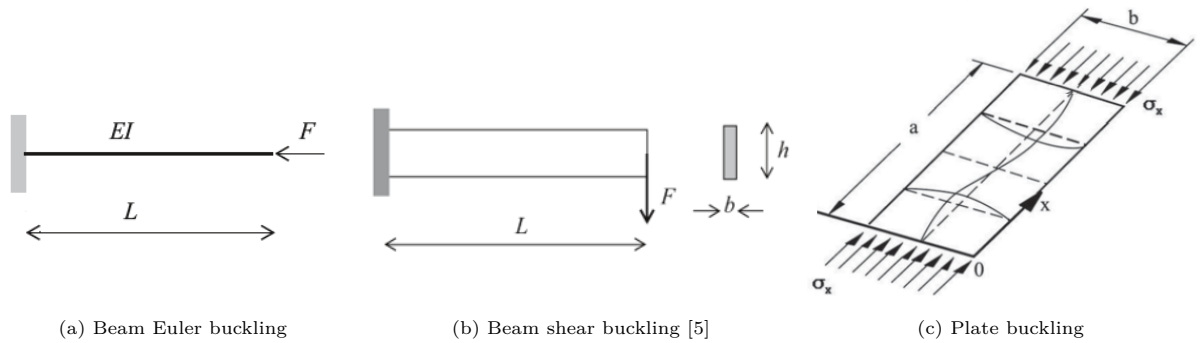


Figure 3.9: Linear buckling scenarios

The factors C and K depend on the boundary conditions of the beam and plate respectively. By applying these equations, the following factors are neglected:

- Plates are elastically supported at beam edges.
- Ribs are elastically constrained along their length by the plate.
- Non-axial load conditions, initial deflection of the structure pre-buckling.

3.3.2. Large ribs test

This section contains the setup and results of a rudimentary test of rib placement and sizing. The ribs are aligned with the peak stress paths perpendicular to the side walls, orthogonal to each other. There are no rounded corners for stress reduction at the rib connections as initial focus is on deflection only. The goals in this test are to:

- Investigate effect of ribs on load deflection behaviour.
- Investigate if manual rib design for equal stiffness is possible.
- Identify how components affect the rib reinforced chassis.

As explained in Figure 2.9 in the previous chapter, the ribs are designed for equal deflections of the chassis structure. To reiterate the approach at rib sizing is as follows:

1. Homogeneous rib sizing based on analysis
2. FEM deflection analysis, compare to plain 1.5mm plate model
3. Parametric sweep, increase thickness of each rib set separately by 0.2mm
4. Observe most/least effective ribs, adjust sizes for equal deflection
5. Add masses or component to model and repeat steps 2-4

The parameters and size ranges of this test are shown in Table 3.3. This test involves large ribs intended to support the chassis top plate and adjacent sidewalls. Therefore it is assumed the plate sections between the ribs are rigidly supported. Details of the preliminary sizing are displayed in appendix E.

<i>Parameter</i>	<i>Description</i>	<i>Value</i>	<i>Unit</i>
T_t	Top plate thickness	0.5	mm
T_s	Sidewall thickness	1.5	mm
T_{bp}	baseplate thickness	1.0	mm
h	rib height	3.5	mm
$t_{LB,LF}$	Longitudinal ribs thickness	1.2 - 1.4	mm
$t_{TB,TF}$	Transverse ribs thickness	1.2 - 1.8	mm
G	Global acceleration load	98.1	m/s ²
Lc	Mass per unit area, corner legs	243.4	Kg/m ²
Lm	Mass per unit area, middle legs	244.8	Kg/m ²
D_{pcb}	PCB stack beams diameter	3.1	mm

Table 3.3: Large ribs model parameters

Figure 3.10 on the following page shows a deflection comparison of the reinforced and plain model. As the global deflection of the top plate is smooth, the absolute deflection at corner nodes is used as reference in step 3 of design approach. These results are shown in Appendix E. To summarise, the following observations are made in this rib design approach:

- Equal deflections can be obtained for the plain model.
- When including LMA masses, more adjustments are necessary to obtain an equally stiff design.
- Considering the PCB stack, a more comprehensive reinforcement structure is necessary.

Brief attempts were made to improve the equal stiffness behaviour of this model. Both by adjusting the main ribs position and adding local small beams to connect the PCB stack. However this is not an effective design approach to maintain equal stiffness and improve mass. There are too many variables to consider and the localised effect of the PCB stacks causes significant jumps in the deflection of the chassis overall. As such the achievable mass reduction is strongly dependant on the expertise of a design engineer that applies this approach.

Similar to the plain model in the previous section, the included components significantly increase the deflection scale of the chassis model. The contour plots displayed in Figure 3.10 compare absolute deflection of the plain and rib reinforced model, relative to the unloaded state. Note that the chassis top plate is actually twisting around the attachment plate, meaning the front of the chassis deflects downwards and the rear part up. These deflections are obtained by only adjusting the longitudinal ribs to a thickness of 1.8mm. The shorter transverse ribs maintain a thickness of 1.2mm. In Figure 3.10 (d) the localised effect of the PCB connections is clearly visible.

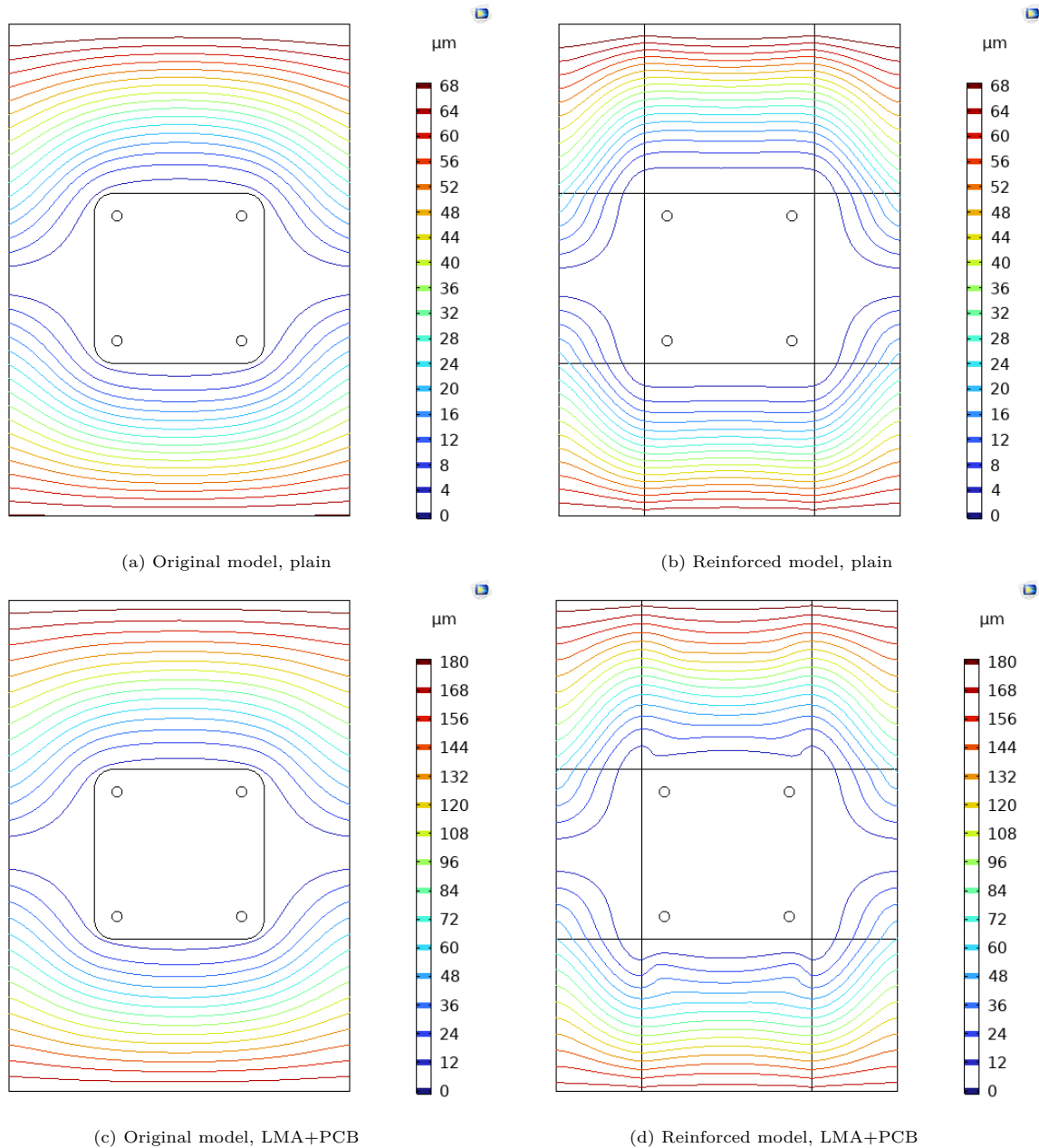


Figure 3.10: Absolute deflection contour plots to Y acceleration

Adjusting the size of any rib pair, longitudinal or transverse, affects every loadcase significantly. This is displayed in Appendix E. Especially the load response to out of plane acceleration in the Z-axis is sensitive to any rib adjustments. This load response from an attachment point central on a plate requires more research. A similar test is carried out in the next section where the stiffness is distributed, rather than focused on the peak loading points.

3.3.3. Rib grid test

As the connection points of the PCB stack interact significantly with provided reinforcement, the designed reinforcement is distributed evenly over the top plate in this test. The applied rib sections are shown in Figure 3.11. A subsequent test analyses the mass savings that can be achieved this rib design approach. Here the weight penalty of thick and slender ribs is evaluated. The objectives in this test are to:

- Observe the effect of distributed reinforcement on deflection of the chassis model.
- Investigate if the localised effect of PCB stacks is reduced.
- Investigate the effects of rib slenderness on stiffness and mass.

The applied approach at rib grid design is as follows:

1. Minimum rib and plate size based on analysis.
2. FEM deflection analysis, compare to plain 1.5mm. plate model
3. Adjust rib grid, observe effects.
4. Add component or mass to model and repeat steps 2-4.

<i>Parameter</i>	<i>Description</i>	<i>Value</i>	<i>Unit</i>
T_t	Top plate thickness	0.5	mm
T_s	Sidewall thickness	1.5	mm
T_{bp}	baseplate thickness	1.0	mm
h	Stiffener height	3.0000	mm
t	Stiffener thickness	0.8000	mm
n_l	Nr. of Longitudinal stiffeners	5 - 6	-
n_t	Nr. of Transverse stiffeners	7 - 8	-
G	Global acceleration load	98.1	m/s ²
Lc	Mass per unit area, corner legs	243.4	Kg/m ²
Lm	Mass per unit area, middle legs	244.8	Kg/m ²
D_{pcb}	PCB stack beams diameter	3.1	mm

Table 3.4: Rib grid model parameters

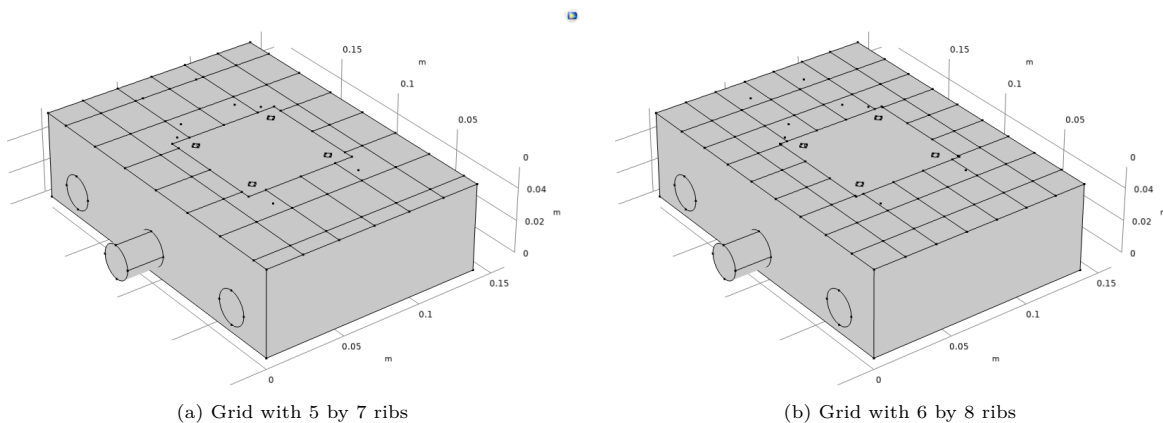


Figure 3.11: Grid reinforced top plate models

Figure 3.12 shows the deflection behaviour of the 6 by 8 grid reinforced model. Of the tested grids, this grid has the closest resemblance to the original model in global deflection magnitude. Again the PCB stack connections do affect the deflection contours, though it is visible the contour gradient lines are not as strongly affected. The vicinity of any ribs to the PCB stacks still affects global deflection considerably, which is indicated in Appendix F. An equal stiffness design can not be obtained with a homogeneous grid in this configuration. However when compared to the large rib design test in the previous section, the grid reinforcement approach is both less complex and closer to equal stiffness when the PCB stack is included.

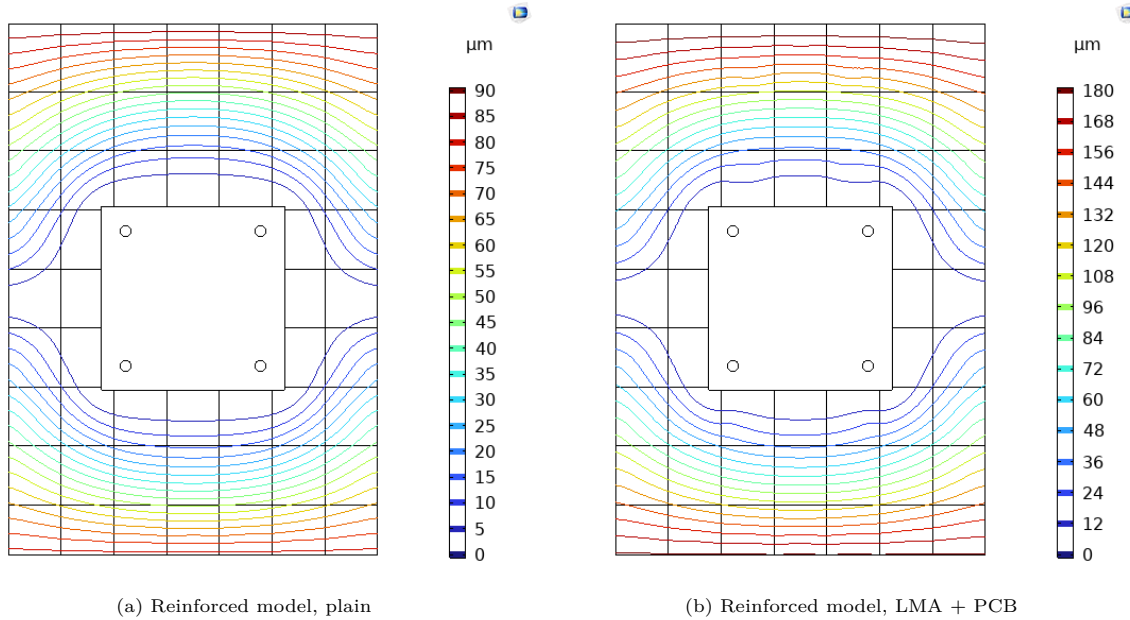


Figure 3.12: Deflection contour plots to Y acceleration

Concerning the effects of ribs sizing on the efficiency of the reinforcement mass, the rib sizes are adjusted as shown in Table 3.5. This parameter sweep is applied to the 6 by 8 rib reinforced model. The results are shown in Table 3.6. While the inertia of the ribs is maintained, the deflections still increase. This is because the effects of plate-rib interaction are not accounted for in the rib sizing.

This test shows applying ribs is an effective method for significant mass reduction, provided this is applicable to the load conditions on the plate. Areas with a strong curvature, as near the attachment plate corners and PCB stack connections, cause excessive bending stresses the structure. Though in this test exact stresses are not evaluated as this is a very coarse model.

Parameter	Description	Value	Unit
h	Stiffener height	3.0000 , 2.6403 , 2.1558	mm
t	Stiffener thickness	0.8000 , 1.1735 , 2.1558	mm
h/t	Stiffener slenderness	3.75 , 2.25 , 1	-
I	Stiffener second moment of inertia	1.80E-12	m ⁴

Table 3.5: Rib sizing parameters

Rib slenderness	Mass [g]	Mass reduction	Deflection increase
- Plain model	91,248	0%	-
3,75	41,735	54,3%	0%
2,25	45,029	50,7%	2.5% - 3.5%
1	54,479	40,3%	6.5% - 9%

Table 3.6: Effect of rib slenderness on mass

While the observed model deflections are considerably smooth, there are still considerable local strains in the structure. This is shown in Figure 3.13, which plots the rotation of the plate topsurface from the neutral axis. Despite the more smooth deflection response from the rib grid, local adjustments are needed in the vicinity of the PCB stack connections.

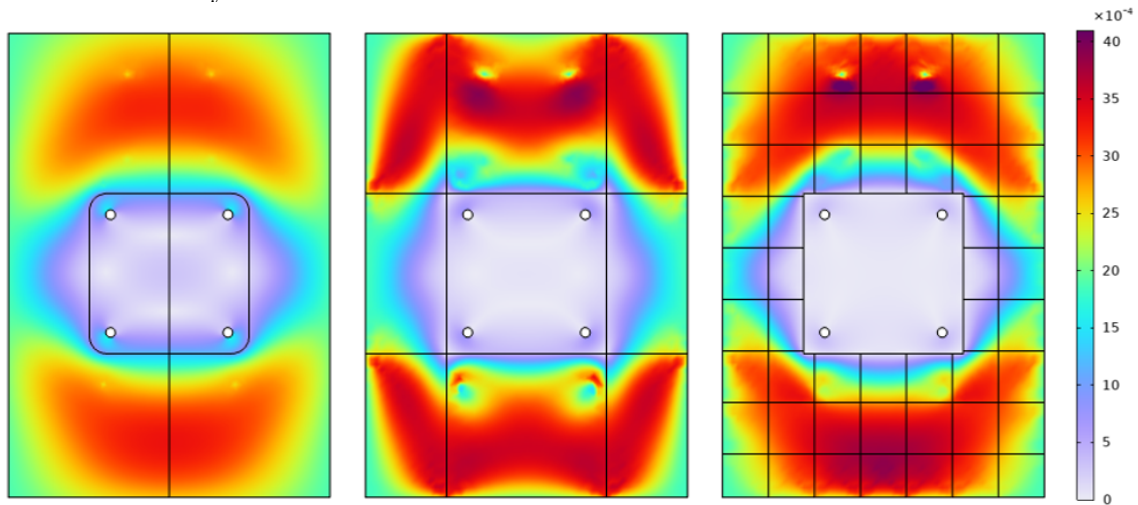


Figure 3.13: Rotation of shell normal in radians

Global deflections are mostly smooth, though local adjustments to the reinforcement are required near the PCB stack connections.

3.3.4. Iso grid test

As distributing the reinforcement with a grid of stiffeners provides beneficial results, a model with ribs in the iso grid configuration is built. The model is generated with the consistent geometric relations applied in the COMSOL model setup parameters, so the grid can easily be altered in size and orientation. After trial and error, with rib size and spacing shown in Table 3.7, the resulting iso grid is shown in Figure 3.14. The model is constructed with the settings as discussed in Section 3.2.1 and a top plate thickness of 0.5mm between the rib members.

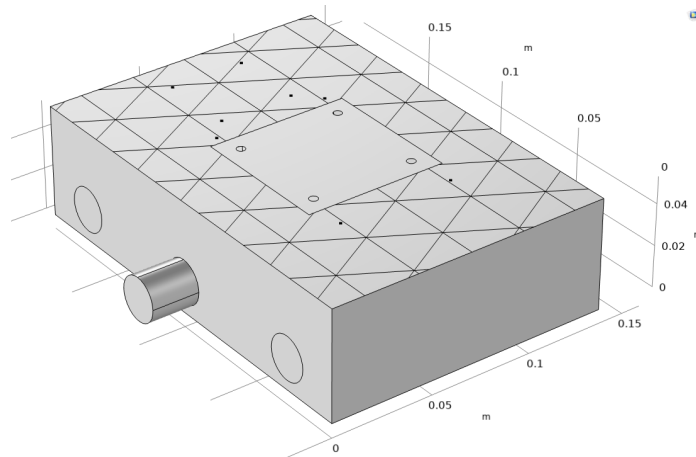


Figure 3.14: Iso grid reinforced chassis model

Parameter	Description	Value	Unit
h	Stiffener height	3.0000	mm
t	Stiffener thickness	0.700	mm
L_{iso}	Iso triangle base size	30.6	mm

Table 3.7: Rib sizing parameters

Observing the resulting deflections in Appendix G, the displayed iso grid setup has equal deflections under all three acceleration loads compared to the original chassis model. However a significant local effect of the PCB stack is still present due to the reduced plate thickness, as can be seen in Figure 3.15. With this configuration and orientation of a reinforcement grid, the PCB stack does not have a disproportional effect on the global stiffness of the chassis.

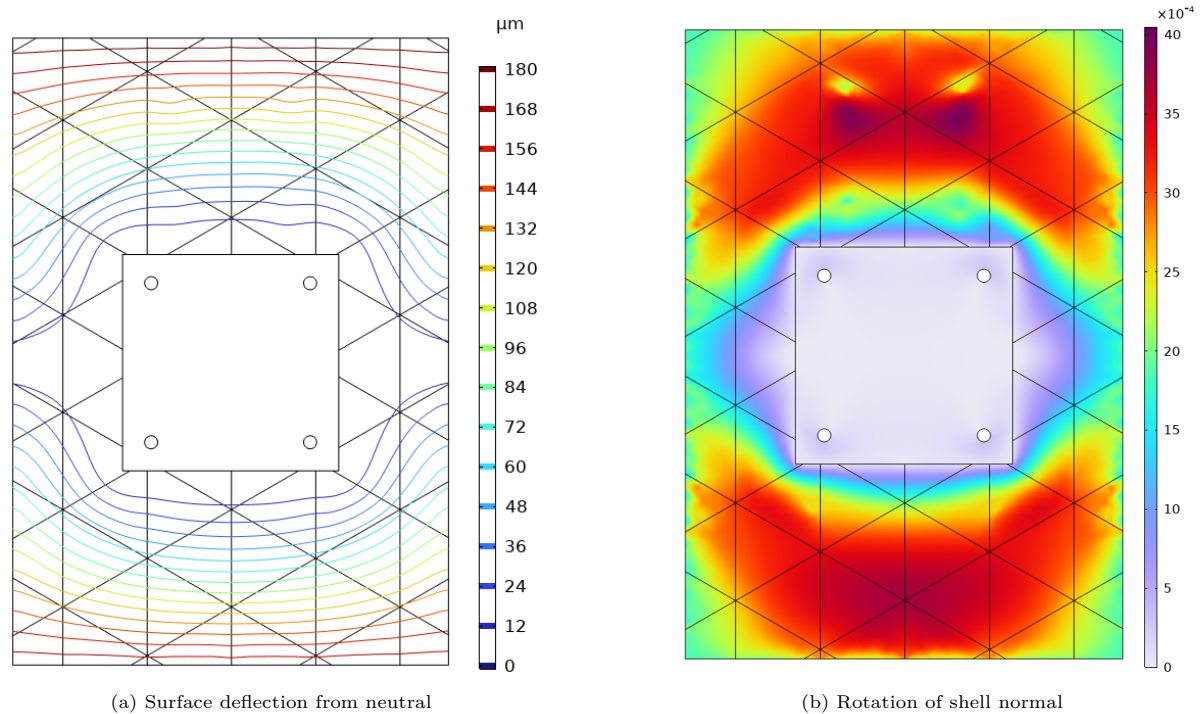


Figure 3.15: ISO grid deflection behaviour

3.4. Conclusion

For the Lunar Zebro chassis, the detachment between the spacecraft attachment plate and PCB stack complicates design of lightweight reinforcement. In the current configuration these bolts connect the top plate to the baseplate, but not the attachment plate to the lunar lander. With the considered configuration, reducing the thickness of this top plate and applying ribs can provide a structure with equal effective stiffness. For the plain chassis model this can be achieved with a coarse set of large ribs, where only adjustments to the rib size and thickness are required.

Including the PCB stack with the loadcarrying configuration complicates the reinforcement design. While it is possible to design an equally stiff reinforcement structure with a reinforcement grid, the PCB stack connections may require significant adjustments when the full component mass is applied. Furthermore, by not connecting the grid members directly to the PCB stack the potential reinforcement of the existing structure is not effectively applied. However further analysis to alternate structure types and potential redesign is not feasible in the time available for this research.

Prioritizing plate reinforcement, grids show beneficial behaviour. They respond smoothly to altered loads and are relatively easy to produce with modern CNC milling. This can be integrated with any existing design, hence more research to grid stiffeners is beneficial. Concentrated out of plane loads, as caused by the PCB stacks, are not included in literature of grid structures design and optimization. Therefore more research to grid design is conducted in the next chapter.

Based on the conducted load analysis and reinforcement modelling, some recommendations for further research can be made. This is discussed in detail in the final chapter of this report. Assuming this configuration of an attachment plate on the top of the chassis is maintained, the following topics should be investigated:

- To apply large ribs as reinforcement, a dedicated size optimization and rib placement study would be better suited.
- Different configurations: The placement of the PCB stack and baseplate connection bolts can be altered to contribute to the chassis reinforcement.

4

Grid Reinforcement Analysis

Based on the findings in Chapter 3 it is evident local loads strongly affect the load response of a grid reinforced structure. Grid stiffened structures are frequently applied in aerospace applications due to their high strength and light weight [44]. An example of such grid designs is shown in Figure 4.1. The configuration of a grid defines the desired orthotropic or isotropic behaviour of the grid reinforced plate. In this chapter the critical aspects for the selection and design of a reinforcement grid are investigated.

Firstly an analysis method is investigated that relates the geometrical properties and physical behaviour of grid stiffened plates. Secondly a set of common grid sections is selected and analysed for the setup of a comparative test. Subsequently the selected grid sections are analysed with varying loading conditions in COMSOL Multiphysics. With this, critical aspects to consider for the design of lightweight reinforcement grids are defined.

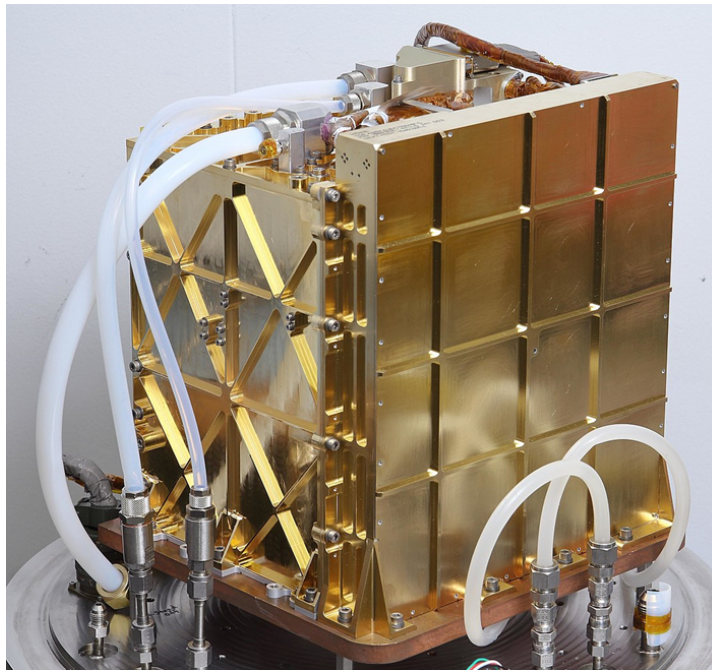


Figure 4.1: Perseverance rover instrument MOXIE [45]

4.1. Composite plate theory for grids

In the bending of a plate or beam, the bending resistance is determined by the inertial properties. When attached to a plate, both the plate and attached ribs no longer bend along their respective central sections. Grid stiffened plates can be analysed using composite plate theory according to methods formulated in [44], which is based on an improved "smeared stiffness" formulation of [46]. The stiffener

grid and adjacent plate are evaluated separately, each factoring the offset of the neutral bending planes. Their contributions to the Equivalent Stiffness Matrix (ESM) are then combined as follows:

$$\begin{bmatrix} N \\ M \end{bmatrix} = \begin{bmatrix} A & B \\ B & D \end{bmatrix} \begin{bmatrix} \varepsilon^0 \\ \kappa \end{bmatrix} = \begin{bmatrix} A^{pl} + A^{st} & B^{pl} + B^{st} \\ B^{pl} + B^{st} & D^{pl} + D^{st} \end{bmatrix} \begin{bmatrix} \varepsilon^0 \\ \kappa \end{bmatrix} \quad (4.1)$$

Where the superscript *pl* indicates the plate and *st* the stiffener grid. The smeared stiffness formulation considers a stiffener grid with a base geometry as shown in Figure 4.2.

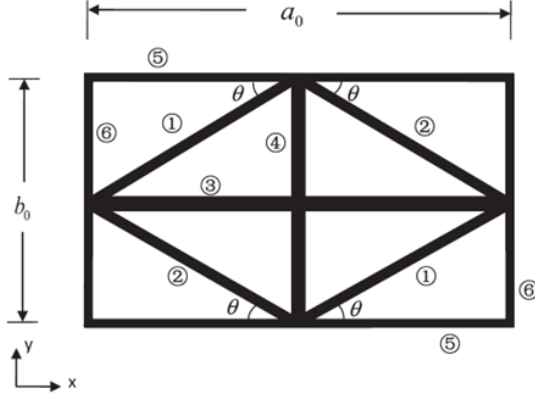


Figure 4.2: Stiffener grid unit cell [44]

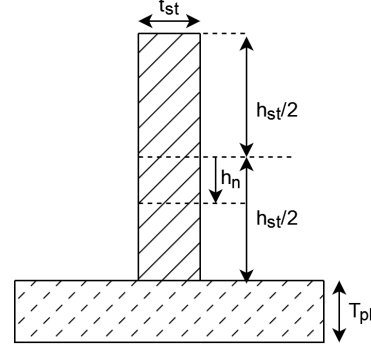


Figure 4.3: Stiffener equivalent neutral surface

As the considered grids are symmetric, the values of k_1 and k_2 are equal in this formulation. When simplified with the geometric relationships between a_0 , b_0 , $s = \sin(\theta)$ and $c = \cos(\theta)$, the loads and moments per unit length acting on the stiffener grid are formulated as follows [44]:

$$\begin{bmatrix} N_x^{st} \\ N_y^{st} \\ N_{xy}^{st} \\ M_y^{st} \\ M_y^{st} \\ M_{xy}^{st} \end{bmatrix} = \begin{bmatrix} R_a (2k_1 c^3 + k_3 + 2k_5) / b_0 & 2R_a k_1 s^2 c / b_0 & 0 & \dots \\ 2R_a k_1 s c^2 / a_0 & R_a (2k_1 s^3 + k_4 + 2k_6) / a_0 & 0 & \dots \\ 0 & 0 & 2R_a k_1 s^2 c / b_0 & \dots \\ \vdots & \vdots & \vdots & \ddots \end{bmatrix} \begin{bmatrix} \varepsilon_x^0 \\ \varepsilon_y^0 \\ \varepsilon_{xy}^0 \\ \kappa_y \\ \kappa_y \\ \kappa_{xy} \end{bmatrix} \quad (4.2)$$

This matrix describes the contribution of stiffener grid unit cells to the ESM in eq. (4.1). Only the existential contribution A^{st} is shown for clarity on the page size. The equations for the coupling B^{st} and bending D^{st} matrices are identical, replacing the parameters of $R_{a,b,d}$. In Appendix H the full stiffener ESM is shown. The existential, coupling and bending contribution are each respectively evaluated by:

$$R_A = EA_{st} \quad , \quad R_B = EA_{st} h_n \quad , \quad R_D = EA_{st} \left(\frac{h_{st}^2}{12} + h_n^2 \right) \quad (4.3)$$

Note that the k_{1-4} factors can only be 0 or 1 and k_{5-6} 0 or 0.5 in this analysis. The applied method assumes a consistent rib thickness and height in the whole grid, where the rib area A_{st} and neutral bending surface h_n are constant. There are other analysis methods that account for the possibility of inhomogeneous rib sizes in a grid [46]. As a stiffener interacts with the adjacent plate, the neutral bending surface of the stiffener is slightly shifted as shown in Figure 4.3. The equivalent neutral surface of stiffeners is evaluated as:

$$h_n = \frac{h_{st}}{2} - \frac{E_{st} h_{st}^2 - E_{pl} T_{pl}^2}{2(E_{st} h_{st} + E_{pl} T_{pl})} = \frac{T_{pl}}{2} \quad (4.4)$$

This is the reduced form of the equation used in [44] as the Young's moduli of the stiffener and plate material are identical in this report. To construct the complete ESM in eq. (4.1), the height of the equivalent neutral surface needs to be evaluated for the plate as well. As this report aims to compare different types of grids, the contribution of the plate is constant in each comparison. Therefore the neutral surface of the plate is not evaluated in this report.

4.2. Grid test configuration

In this section the grid stiffened plates applied in the model analysis are defined. Common grid sections as shown in Figure 4.4 are considered. To provide a valid comparison, all analysed grids have identical rib properties. At first the sizing of the ribs is determined. Afterwards the configuration and sizing of the analysed grids is explained.

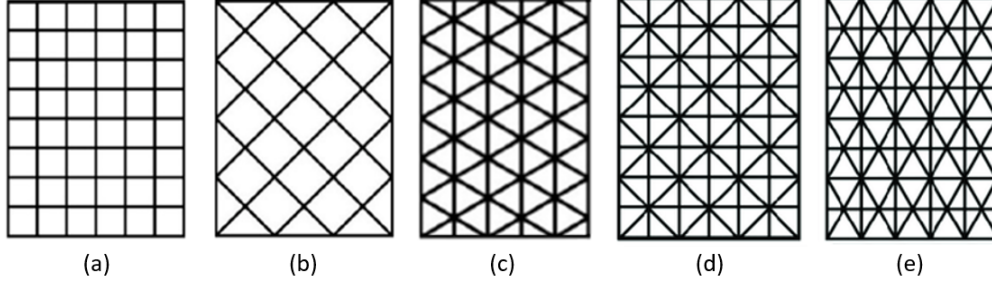


Figure 4.4: Common grids: (a) ortho grid, (b) waffle grid, (c) iso grid, (d) bi-ortho grid, (e) bi-isogrid

4.2.1. Buckling phenomena and rib sizing

To design a reinforcement grid as primarily supporting the plate, local rib buckling should be prevented. Local buckling in ribs or stiffeners as shown in Figure 4.5 is known as crippling [38]. In a linear plate buckling scenario, the compressive stress where crippling occurs can be calculated by [43]:

$$\sigma' = K \frac{E}{(1 - \nu^2)} \left(\frac{t}{h} \right)^2 \quad (4.5)$$

Here t is the rib thickness and h the rib height from the plate surface as shown in Figure 4.3. The length of the local buckling section is considered with the factor of K , which also considers the boundary conditions of the rib. Assuming the plate provides clamped support and the rib is simply supported along its own length, the most critical factor of $K = 1.09$ is applied. This corresponds to a buckling half wavelength l of 1.6 times the rib height.

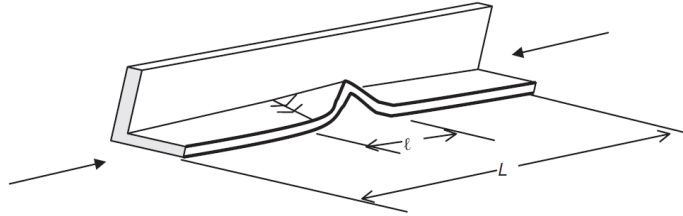


Figure 4.5: Stiffener crippling [38]

For linear buckling analyses of stiffened cylinder structures, NASA recommends a knockdown factor or Safety Factor (SF) of 1/3 to account for nonlinear buckling phenomena and production irregularities [47]. As the exact load distribution and post-buckling behaviour are unknown, the SF is set to 1/6. Buckling behaviour of the structure must be verified for the Design Load [26], which is a factor of the material ultimate load. Therefore the critical buckling load is calculated as:

$$\sigma_{crit} = \frac{\sigma_{DL}}{SF} = \frac{\sigma_U}{1.5 * SF} \quad (4.6)$$

Inverting eq. (4.5) and applying the ultimate load of AL7075-T6 of 560MPa, the critical aspect ratio of the ribs, also known as the slenderness, is set as:

$$\frac{h}{t} = \sqrt{K \frac{E}{\sigma_{crit} (1 - \nu^2)}} \approx 6 \quad (4.7)$$

Note that in this method of rib sizing, the following assumptions are made:

- Local plate buckling does not occur.
- Plate provides clamped support for stiffeners, contrary to elastic support.

4.2.2. Geometry and sizing of tested grids

To investigate how different grid types behave, the ortho, waffle and iso grids are applied in the model analyses. This is sufficient to analyse the behaviour of different grid configurations as the combined bi-ortho and bi-iso grids contain the same configuration aspects. The geometry of the test cases is shown in Figure 4.6. The total rib length on the plates is identical in each of these cases. This means for identical rib and plate cross sections, the mass and volume is automatically identical for all grids and plates.

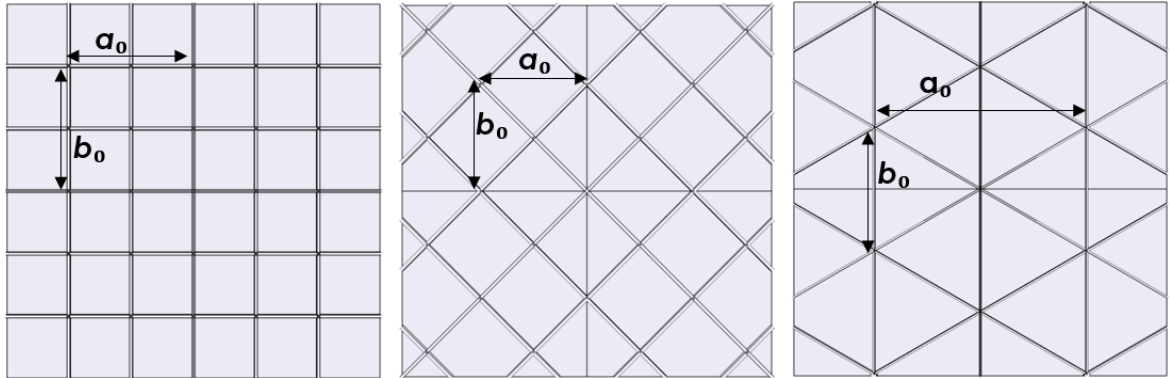


Figure 4.6: Hypothetical grid sections for model analysis

Examples in literature suggest a 50% grid to plate mass ratio [47]. In the following models, the volumetric size ratio is varied around this range. In order for all grid stiffened plates to have equal masses and volume, the number of ribs in the ortho grid is leading. The spacing of the waffle and iso grids is adjusted to obtain an identical grid size. The parameters of the grid reinforced plate sections are shown in Table 4.1 for the 50% grid to plate mass ratio. In the next section the adjusted rib and plate parameters are discussed, as the mass ratio is varied.

<i>Parameter</i>	<i>Description</i>	<i>Value</i>	<i>Unit</i>
l	Plate length/width	160	mm
h	Rib height	7.5	mm
t	Rib thickness	1.25	mm
h/t	Rib slenderness	6	-
T	Plate thickness	0.5859	mm
a_{0_iso}	Iso grid length	91.40	mm
b_{0_iso}	Iso grid width	52.77	mm
a_{0_orto}	Ortho grid spacing	53.33	mm
a_{0_waffle}	Waffle grid spacing	45.20	mm

Table 4.1: Parameters of reinforcement grid comparison

For the selected grid types, the ESM contribution is as follows:
 Ortho grid with $\theta = 45^\circ, k_1 = 0$:

$$\begin{bmatrix} N_x^{\text{st}} \\ N_y^{\text{st}} \\ N_{xy}^{\text{st}} \\ M_y^{\text{st}} \\ M_y^{\text{st}} \\ M_{xy}^{\text{st}} \end{bmatrix} = \left(\frac{1}{a_o} \right) \begin{bmatrix} 2R_a & 0 & 0 & 2R_b & 0 & 0 \\ 0 & 2R_a & 0 & 0 & 2R_b & 0 \\ 0 & 0 & 0 & 0 & 0 & 0 \\ 2R_b & 0 & 0 & 2R_d & 0 & 0 \\ 0 & 2R_b & 0 & 0 & 2R_d & 0 \\ 0 & 0 & 0 & 0 & 0 & 0 \end{bmatrix} \begin{bmatrix} \varepsilon_x^0 \\ \varepsilon_y^0 \\ \varepsilon_{xy}^0 \\ \kappa_y \\ \kappa_y \\ \kappa_{xy} \end{bmatrix} \quad (4.8)$$

Waffle grid with $\theta = 45^\circ, k_{3,4,5,6} = 0$:

$$\begin{bmatrix} N_x^{\text{st}} \\ N_y^{\text{st}} \\ N_{xy}^{\text{st}} \\ M_y^{\text{st}} \\ M_y^{\text{st}} \\ M_{xy}^{\text{st}} \end{bmatrix} = \frac{1}{\sqrt{2}} \left(\frac{1}{a_0} \right) \begin{bmatrix} R_a & R_a & 0 & R_b & R_b & 0 \\ R_a & R_a & 0 & R_b & R_b & 0 \\ 0 & 0 & R_a & 0 & 0 & R_b \\ R_b & R_b & 0 & R_d & R_d & 0 \\ R_b & R_b & 0 & R_d & R_d & 0 \\ 0 & 0 & R_b & 0 & 0 & R_d \end{bmatrix} \begin{bmatrix} \varepsilon_x^0 \\ \varepsilon_y^0 \\ \varepsilon_{xy}^0 \\ \kappa_y \\ \kappa_y \\ \kappa_{xy} \end{bmatrix} \quad (4.9)$$

ISO grid with $\theta = 30^\circ, k_{3,5} = 0$:

$$\begin{bmatrix} N_x^{\text{st}} \\ N_y^{\text{st}} \\ N_{xy}^{\text{st}} \\ M_y^{\text{st}} \\ M_y^{\text{st}} \\ M_{xy}^{\text{st}} \end{bmatrix} = \frac{3}{4} \left(\frac{1}{a_0} \right) \begin{bmatrix} 3R_a & R_a & 0 & 3R_b & R_b & 0 \\ R_a & 3R_a & 0 & R_b & 3R_b & 0 \\ 0 & 0 & R_a & 0 & 0 & R_b \\ 3R_b & R_b & 0 & 3R_d & R_d & 0 \\ R_b & 3R_b & 0 & R_d & 3R_d & 0 \\ 0 & 0 & 0 & 0 & 0 & R_d \end{bmatrix} \begin{bmatrix} \varepsilon_x^0 \\ \varepsilon_y^0 \\ \varepsilon_{xy}^0 \\ \kappa_y \\ \kappa_y \\ \kappa_{xy} \end{bmatrix} \quad (4.10)$$

4.3. Grid model analysis

In this section the designed plate sections are modelled in their load response with varying boundary conditions. To observe the grid behaviour, a load of 100N is applied at the center of the plate both in and out of plane. The goals in this test are to identify critical aspects in the design of a reinforcement grid. The following aspects are investigated:

- How the grid configuration affects load response to local in plane and out of plane loads.
- Effect of pinned or fixed plate boundary conditions.
- Effect of the grid to plate size ratio.

The ESM of each plate grid type is applied with the observations of the modelled deflection and stress results. Firstly the model setup of the grids in in COMSOL Multiphysics is explained. Subsequently the model analyses are discussed.

4.3.1. Grid model setup

The models apply tangent shell elements as plate stiffeners instead of the beam elements from the previous chapter. This provides better control of the plate and stiffener boundary conditions, and also improves visual analysis of the stress response. As mentioned in the previous section, the volume of the stiffener grid is varied about 50% of the total volume. This is done in increments of 10% by performing a parametric sweep. The parameters are shown in Table 4.2.

<i>Grid mass %</i>	<i>Rib height (mm)</i>	<i>Rib thickness (mm)</i>	<i>Plate thickness (mm)</i>
20	4.7434	0.7906	0.9375
30	5.8095	0.9682	0.8203
40	6.7082	1.1180	0.7031
50	7.5000	1.2500	0.5859
60	8.2158	1.3693	0.4688

Table 4.2: Plate and grid size sweep parameters

Depending on the applied load, the model is constructed using one or two symmetric edge boundary conditions. This is explained with the load application at each test. The mesh is generated with a maximum element size of 2.1mm, thus there are either 3 or 4 elements over the rib height. This means the larger grids are modelled with roughly 10% more DOFs. The generated meshes are shown in Appendix I.

4.3.2. Out of plane point load

Figure 4.7 shows the applied load and boundary conditions of the ortho grid model. The iso and waffle grids have identical applied conditions as shown in Appendix I. For the applied boundary conditions, the pinned outer surface has a constant plate thickness of 1.5mm and is not included in the evaluated rib mass. The edges with prescribed displacements U and rotations θ correspond with the symmetric behaviour of the full plate model. When a rib is located on the symmetric edge, it is modelled with half the normal rib thickness. Figure 4.8 shows the resulting load deflection response of the grid reinforced plates.

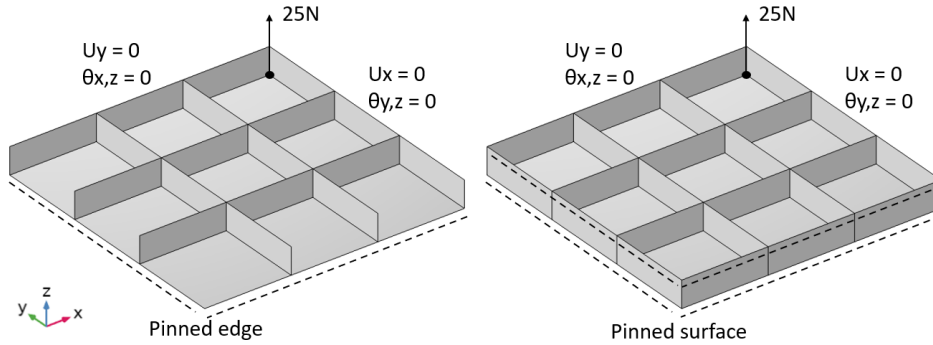


Figure 4.7: Model boundary conditions for out of plane load

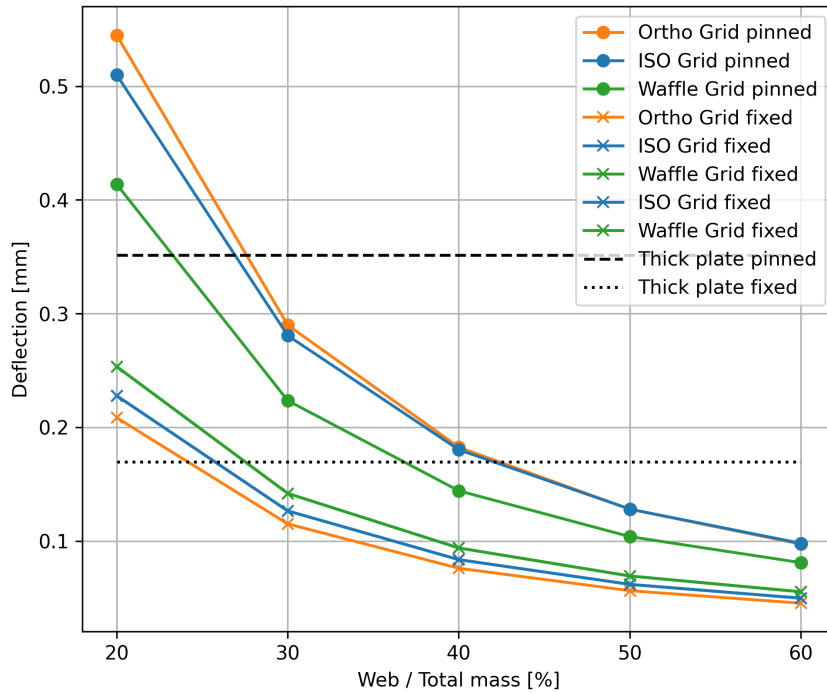


Figure 4.8: Rib grids deflection comparison with out of plane point load

The black lines indicate the deflection of plain plates with twice the mass of the grid reinforced plates. From this model analysis, the following observations are made:

When the grid edges are fixed to an outer wall, the grid performance is the opposite of the pinned boundary condition. For the fixed grids, the resulting sequence of the most to least stiff grid types corresponds with the largest strain $\varepsilon_{x,y}$ and bending $\kappa_{x,y}$ resistance as evaluated in Section 4.2.2.

Without outer walls, the waffle grid has significantly higher stiffness than the other grids. This can be explained by the twisting resistance κ_{xy} . When the rib edges are free the curvature rates of κ_x and κ_y change significantly near the corners. This is visible in the stress plots in Appendix I. The same resistance can be observed in the diagonal members of the iso grid, though the grid spacing is too large for the outer grid members to contribute significantly.

4.3.3. In plane load

This section considers the load response to an in plane load of 100N centered on the grid reinforced plates. The applied load and boundary conditions are shown for the ortho grid model in Figure 4.9. A symmetric boundary condition is applied similar to the previous section, with half the plate thickness and load modelled on the symmetric edge.

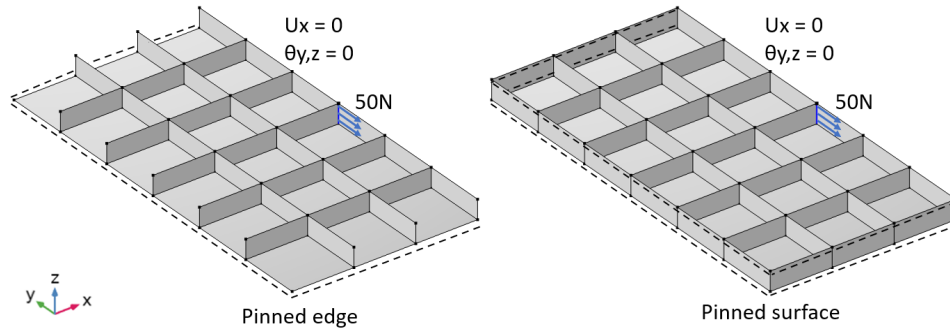


Figure 4.9: Model boundary conditions for in plane grid load

The model configuration and mesh are shown in Appendix J for all three grids. The analysed deflection results and model DOFs are shown here as well. Figure 4.10 compares the obtained deflections at the top of the loaded rib edge for all grids.

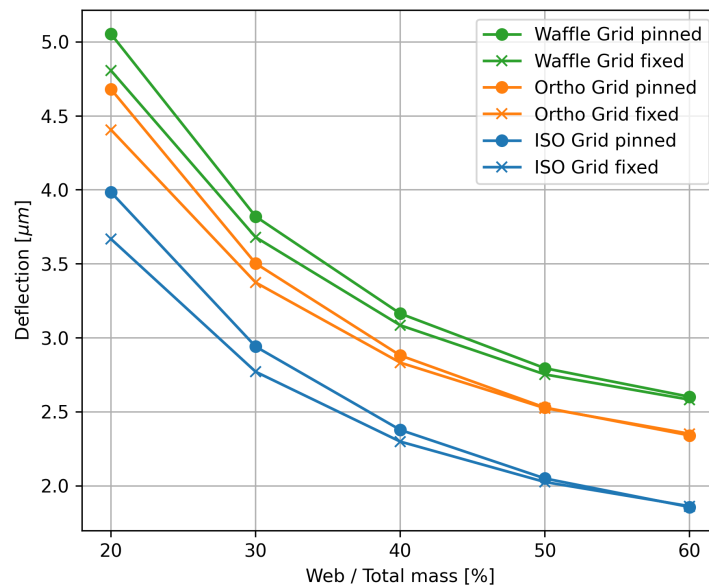


Figure 4.10: Rib grids deflection comparison with in plane point load

While the waffle grid has the highest resistance to shear loads according to the ESM, this is not the case for the localised load setup in this test. The parallel alignment of a grid member with the applied load has a more noticeable effect. In this loadcase the iso grid has the highest stiffness. This makes sense as the iso grid has an intersection of three ribs to provide both axial and shear load resistance, compared to the two rib intersection of the other grid types.

4.3.4. Distributed in plane load

As it is unlikely only the rib grid is exposed to the in plane load in a practical application, the load application is varied in this test. In a practical scenario, the load in the plate is caused by a bolt or pin attached to the grid stiffened plate. The previous isogrid model without outer walls is applied in three more scenario's. First, the load is distributed over the edge and plate centerpoint as shown in Figure 4.11. The dotted lines indicate the shell surface, as the load is applied in the mid plane. To compare these with a more practical situation, two models with solid cylinders are applied to resemble a bolt attachment. Here the load is distributed over the cylinder body as shown in Figure 4.12.

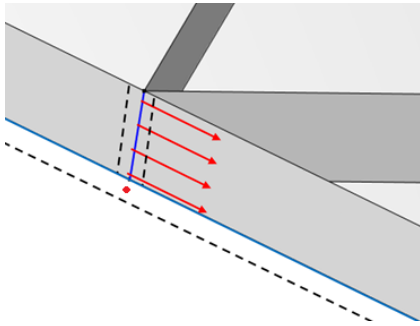


Figure 4.11: Edge and point load

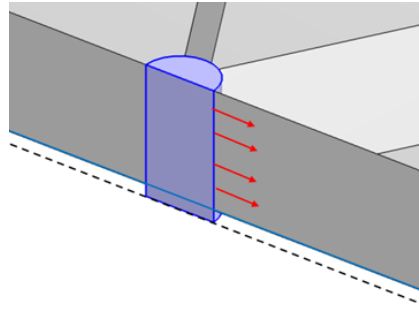


Figure 4.12: Body load

The load test is identical to the previous section, again applying a 50N load and symmetric boundary conditions. For the combined edge and point load as shown in Figure 4.11, the 50N load is distributed by the ratio of the total rib height and plate thickness. The magnitude of the edge load is the rib height divided by the total height, and the point load is the plate thickness divided by the total height.

The results of the deflection analysis are shown in Figure 4.13. Here the absolute deflection is shown, observed at the top of the ribs at the applied load. It is clear that distributing the load over the rib edge and a plate point does not compare to the deflection caused by a loaded bolt. The cylinders resembling a bolt attachment have diameters of 5mm and 8mm. This diameter is variable in the constructed model, and provides an interesting effect in the resulting deflection. Between these values, the stiffness of the plate overrides the reinforcement provided by the grid. This is especially true for the 8mm cylinder, which experiences a stronger deflection as the plate size decreases.

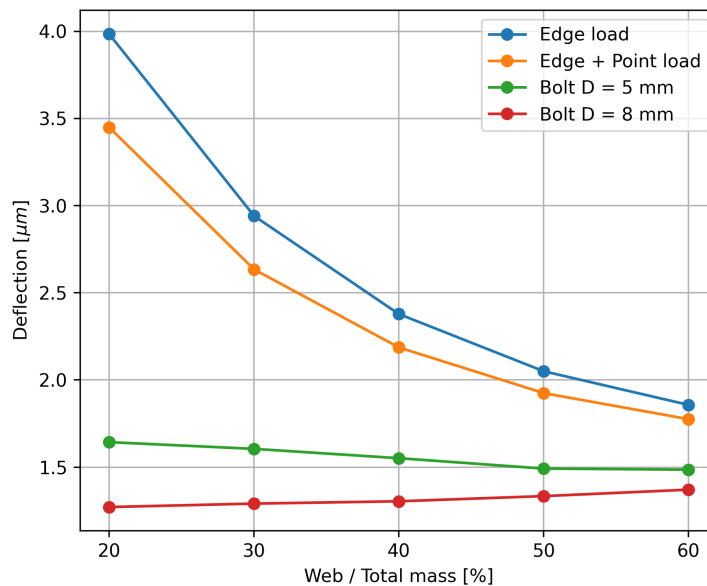


Figure 4.13: Variable in plane load application on ISO Grid

4.3.5. Discussion of results

This section contains the FEM analysis results of an ortho grid, waffle grid and iso grid reinforced plate section. All reinforced plates have identical properties rib cross section and total grid mass. Each grid reinforced plate is subjected to a hypothetical load of 100N, both in plane and out of plane. Applying the ESM contribution of each grid from the previous section, observations are made on the resulting load behaviour.

Especially for the out of plane load, the behaviour of the outer edge of the plate affects the resulting load response. Where the ortho grid has the lowest stiffness with simply supported boundaries, this grid has the highest stiffness when the grid members are attached at the outer edge. For the in plane load, the grid with the highest number of intersecting ribs has the highest load resistance. Though when the 100N load is applied to a cylinder nested in the grid instead of the element edges, the contribution of the grid becomes marginal.

It should be noted that the applied ESM analysis neglects the out of plane shear resistance of the ribs. Observing the stress response in Appendix I, the resulting in plane loads $N_{x,y}$ are in the order of 8 times higher than the out of plane shear loads $N_{xz,yz}$ in the ribs. Hence for the considered rib height and plate thickness, the out of plane shear resistance can be neglected.

4.4. Discussion

This chapter investigates the critical aspects for the design of ideally stiff reinforcement grids. A smeared stiffness approach is applied with composite plate theory to provide an intuitive overview of the design parameters of a grid reinforcement plate. This relates the geometrical parameters of a grid to the stiffness behaviour in the ABD matrix.

The grid configuration characteristics are investigated with a hypothetical set of grid reinforced plates subjected to 100N loads in the plate center. In the design of these grids, buckling considerations are simplified. To provide an optimal lightweight grid design for panels under compression or shear loads, further analysis of buckling behaviour is required.

The conducted model analyses successfully indicate the load carrying properties of basic grid configurations. For a more comprehensive set of loads, a combined grid as the bi-ortho or bi-iso grid can be selected. The smeared stiffness approach with the ESM can be applied to identify which grid type aligns with the considered loadcase.

The conducted analyses indicate a significant interaction between the reinforcement grid and the plate boundary conditions. This was strongly simplified in the previous chapter, and should be considered for the selection and design of stiffener grids for the Lunar Zebro. This is included in the recommendations at the end of this report.

5

Conclusion

This chapter concludes the research on lightweight reinforcement design for the Lunar Zebro. First the findings are discussed, related to the study of structural reinforcement methods and the applied and tested methods of rib design. The final section contains recommendations for implementation and future research for the Lunar Zebro.

5.1. Conclusion

From the reviewed designs in planetary rovers and space structures, there is no indication that the monolithic semi-monocoque structure is optimal for the Lunar Zebro. Despite the unique characteristics of the Lunar Zebro compared to other extra-terrestrial vehicles, implementing the other design methods can be beneficial. Considering to the many design requirements of the chassis, as well as the uncertainty of the future mission profile, the design problem is too complex to investigate a completely new design approach. This concludes the first research objective, and is discussed further in the recommendations.

Due to these uncertainties, this report has investigated methods to reduce the plate mass and apply ribs with the current structure configuration. Investigated methods for the design of rib reinforcement can be applied to reduce the mass of the Lunar Zebro without reducing the stiffness, thereby maintaining resistance to other static and dynamic mechanical loads.

To analyse the load response of the Lunar Zebro chassis, a case is performed in COMSOL with a simplified chassis structure. The load response to static full body acceleration is investigated in three configurations. One plain box structure, one with the added mass of the Leg Module Assemblies and finally the PCB connection bolts are included. Including the PCB stack with the loadbearing structure provided a clear reduction in deflection. This connection of the top and bottom chassis plate noticeably increases the stiffness of the chassis, reducing the stresses in the top plate.

Applying large ribs can provide an equally stiff design for the plain and weighted structure. With some modifications to the individual rib sizes the global deflections are equal to the original chassis. However in a more complex design case, this approach is not convenient. The interaction with the PCB stack greatly affects the stiffness of the overall structure. Even with a small set of ribs many modifications are required to provide an equally stiff structure. For large ribs a different design strategy is required that links the ribs to significant structural points, rather than a plate based approach.

Distributing the reinforcement with a grid of ribs is beneficial for equal stiffness design. The smooth load response of a grid reduces the localised effect of the PCB stack significantly, though some excessive local strains are still observed. In the conducted rib design tests, the thickness of the top plate is reduced from 1.5mm to 0.5mm. With the applied ribs, a mass reduction in the order of 50% is observed, though local adjustments are required to reduce local stresses. Applying ribs to the existing design is a feasible method for mass reduction while maintaining global stiffness of the structure.

To approach a more comprehensive design challenge, the behaviour of grid reinforcement structures is analysed further. It is investigated which factors are essential to consider for the design of an ideal reinforcement grid. By applying composite plate theory with the smeared stiffness method, an intuitive

overview is provided that relates the grid and plate geometry to the combined load behaviour in the ABD matrix. From the conducted grid analyses, the importance of the plate edge behaviour is apparent. Where some grids behave ideally stiff on a simply supported plate, this response is inverted on a clamped plate. With these considerations and the discussed analysis method, an optimally stiff reinforcement grid can be designed for specific load scenarios.

5.2. Recommendations

Thin plates with rib reinforcement can result in immediate mass savings for the Lunar Zebro chassis. The research conducted in this report contains the essential considerations for rib reinforcement design, though some further analysis is required. In the conducted chassis model analyses the rib edge behaviour was not considered. The link between ribs and the chassis sidewalls is removed by the simplifications. Conversely all ribs are rigidly linked to the attachment plate. This is not necessarily the case when the attachment plate is on the outer surface and the ribs can be inside the chassis. To apply rib grids in the design of the Lunar Zebro, the following aspects need to be investigated:

- The increase in local stresses and risk of permanent deformation.
- Production limitation of small ribs and thin plates.
- Nonlinear buckling behaviour of the rib-plate assembly.

Further recommendations for future research are explained below.

Chassis shape considerations:

The complex shape of the monolithic chassis complicates the production of the chassis itself as well as the required insulation. Changing the chassis to a more simple box structure allows for a wider material selection of the insulation material. Additionally the aluminium body can be supported during the CNC milling process, reducing the plate thickness limit. The camera hubs can be made external structures, similar to all deployed planetary rovers.

Structure configuration:

The disconnection between the attachment plate and rigid structural components results in a complex design problem. The PCB stack and baseplate attachment bolts should be considered for their local effects on the structure. As the attachment method to the lunar landing vehicle is not definitive, an optimization study can be conducted on the configuration of this structure. The components can be connected by a skeletal structure in a shape or size optimization study. Reconsidering the placement of the attachment points can improve the mass and stiffness of the structure significantly.

Loadbearing components:

The current design considers only the body and baseplate as part of the primary structure, neglecting the PCB stack. Many components can be considered for their loadbearing potential. The Leg Module Assemblies are a significant part of the mass budget and can be integrated with the chassis walls. Furthermore applying the PCB stack and internal circuit boards as load bearing structures can significantly reduce the loads on the chassis. This has been done before in the Mars Sojourner rover.

Space frame redesign:

Significant mass savings can be obtained with the use of composite sandwich materials. This requires more research in the production methods and certification requirements of the Lunar Zebro. Altering the semi-monocoque design scheme is a difficult subject in the sealing properties of the chassis. Investigating the weight penalty of separate external panels is a priority in this design approach.

Reinforcement grid design for local loads:

The conducted grid analyses consider an ideal scenario with the load located on the intersection of grid members. When this is not the case, adjustments may be necessary depending on the magnitude of the load or loads. The local plate thickness can be increased, more grid members can be added or the spacing of the grid can be adjusted. A shape optimization study can provide useful insight to the ideal grid design approach for such situations.

A

Physical testing methods

As the simulation of physical behaviour by FEM relies on simplifications and inherent mathematical linearization, physical testing is still essential to validate designed structures. Some examples of mechanical tests applied in the verification of space structures are [5]:

- Centrifuge: Full body acceleration loads
- Wiffle tree: Distributed load on a deforming structure (Figure A.1)
- Shaker: Vibration response
- Drop table: Shock and vibration response

These setups can also simulate combinations of loads. For example, applying a heater or vibrator in a structure on a centrifuge combines static mechanical loads with dynamic mechanical or thermal loads. This is especially useful for secondary structures, which are very sensitive to vibration loads [5].

Verification by testing requires reporting on the objectives, configuration and success criteria of the test based on the available setup and instrumentation resources. A test report containing this data, along with a formulated test prediction, can be drafted according to the standards formulated by ESA [26].

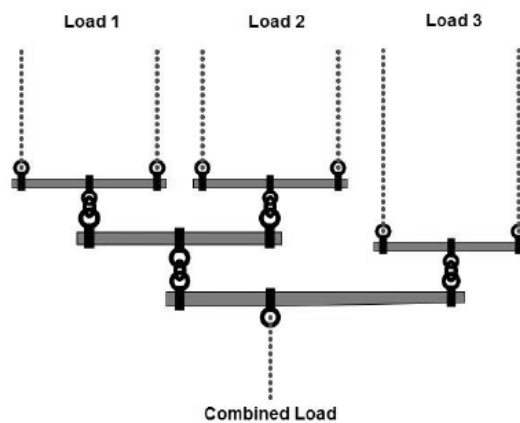


Figure A.1: Wiffle tree load distribution [48]

B

Chassis design process evaluation

In the table below the design choices as described in the body and thermal documentation of the Lunar Zebro [39] are reviewed within the structural design phases as discussed in section 1.4 from [25]. This is a summary of the complete list of requirements and selection criteria as described in [39], with the intent to highlight design choices that can be reconsidered in a (re-)design process.

Design phase	Considerations
Requirements	The chassis shall house all components, carry all loads Withstand a micrometeor impact "in the milligram range" at 10km/s Withstand an average solar flux of 1358W/m ² Act as a heatsink, provide thermal transport
Shape selection	Component placement: - Collision protection & vantage point for cameras - Leg separation and clearance below chassis - Solar panel, power supply port, deployment plate
Scheme selection	(Semi)Monocoque, component installation baseplate Uninterrupted internal volume External insulation
Connections definition	Trusses/beam stack for internal component housing Bolt-Nut attachment holes for external components
Structural members definition & sizing	Flat plate chassis w.r.t. minimum internal volume Sufficient space for installation & cable routing External connections: required nr. of bolts to maintain seal
Verification	Ansys analysis by external company
Realisation	External companies, 5 axis CNC milling aluminium chassis Ceramic CMC baseplate from Arceon

Based on the requirements and shape selection criteria, aluminium was selected as a suitable and affordable material. The addition of external insulation for thermal management occurred in a later stage of design and testing. The stated requirements for the chassis structure did not consider this insulation, which positively affects the required solar flux resistance and meteoric impact protection. where both the meteor impact protection and solar flux resistance are potentially improved significantly by the insulation.

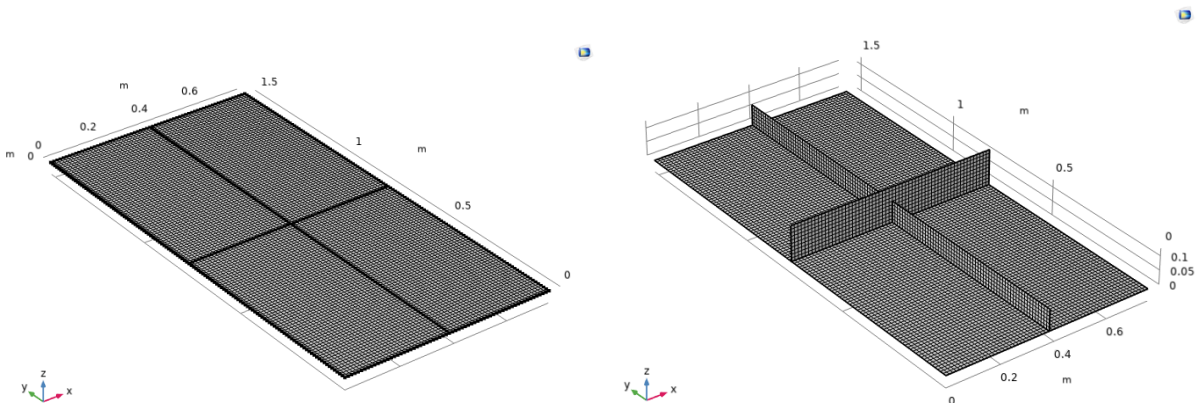
C

Finite Element Analysis Validation

Parameters of the example studies [41]

Parameter	Value	Unit	Description
a	25.4	mm	Width base shell
t	0.254	mm	Thickness base shell
b	762	mm	Length stiffened shell
c	1524	mm	Width stiffened shell
d	6.35	mm	Thickness stiffened shell
e	127	mm	Stiffener height
g	76.2	mm	Stiffener height
f	12.7	mm	Stiffener thickness
v	0.3	-	Poisson ratio
E1	117.21	GPa	Youngs Modulus non-stiffened shell
E2	203.84	GPa	Youngs Modulus stiffened shell
F	4448	N	Point load
p1	6894.76	Pa	Pressure load non-stiffened shell
p2	68947.57	Pa	Pressure load stiffened shell

FEA models of the stiffened plate analysis, finest meshes:



For the MITC9 data from COMSOL, the number of edge elements and total DOFs was given by the software. These values were also calculated to validate understanding of the element to total DOFs calculation. For both the CTRIB3 and Shell181 analyses these values were calculated based on the given amounts of elements. The calculation for the total number of DOFs takes into account the amount of shared DOFs per element for centered elements, edge elements and 4 corner elements as follows:

$$\text{Total DOFs} = \text{TotalElements} * [\text{center DOFs}] + \text{EdgeElements} * [\text{edge DOFs}] + 4 * [\text{corner DOFs}]$$

Estimation of the CTRIB3 data is based on the simplification that most corner nodes are shared between 6 elements. A CTRIB3 element has 3 translational DOFs on each corner node and 1 rotational DOF on every edge node. A triangular mesh can resemble a square mesh by dividing the number of total elements by two. Hereby the number of edge elements is calculated.

$$\text{Edge Elements} = 4 * \sqrt{\text{TotalElements} * \frac{1}{2}}$$

$$\text{Total DOFs} = \text{TotalElements} * 3 + \text{EdgeElements} * 2 + 4 * 1.5$$

Estimation of the Shell181 data, which has 3 translational and 3 rotational DOFs on all corner nodes:

$$\text{Edge Elements} = 4 * \sqrt{\text{TotalElements}}$$

$$\text{Total DOFs} = \text{TotalElements} * 6 + \text{EdgeElements} * 3 + 4 * 1.5$$

For the stiffened plate analysis, all plates are rectangular instead of square. The number of edge elements is estimated by $8 * \sqrt{\text{TotalElements}}$, again halving the number of total elements for the triangular CTRIB3 mesh.

Data of the plain plate analysis:

Element Type	Total Elements	Edge Elements*	Total DOFs*	Displacement [m]
CTRIB3	1534	110	4824	6,642E-05
	5830	211	17922	6,628E-05
	22700	426	68952	6,629E-05
	43632	591	132078	6,629E-05
Shell181	2500	200	15606	6,659E-05
	10000	400	61206	6,673E-05
	22500	600	136806	6,680E-05
	40000	800	242406	6,683E-05
MITC9	324	72	8220	6,657E-05
	900	120	22332	6,668E-05
	2500	200	61212	6,679E-05
	8100	360	196572	6,686E-05

Data of the stiffened plate analysis:

Element Type	Total Elements	Edge Elements*	total DOFs*	Displacement [m]
CTRIB3	5088	404	16071	2,734E-04
	19840	797	61114	2,846E-04
	44552	1194	136044	2,891E-04
Shell181	2130	369	13911	2,743E-04
	8530	739	53421	2,805E-04
	19170	1108	118368	2,834E-04
	34080	1477	208935	2,852E-04
MITC9	218	119	5970	2,703E-04
	1554	321	39246	2,779E-04
	3458	482	85908	2,808E-04
	8388	750	205836	2,836E-04

Data of the beam stiffener analysis:

Element Type	Shell Elements	Edge Elements*	total DOFs*	Displacement [m]
MITC9 Shells + Beams	200	90	5352	2,6264E-4
	1300	228	32580	2,6955E-4
	3612	384	89004	2,7077E-4
	8712	594	212664	2,7124E-4

Data of shell - beam stiffener comparison, stiffener height reduced with thickness constant:

Element Type	Stiffener Height Ratio	N DOFs	Displacement [m]	Difference in disp. : (Shell-Beam)/Shell
Shell plate Shell stiffeners	1,000	205836	2,836E-04	-
	0,875	201534	3,826E-04	-
	0,750	200082	5,497E-04	-
	0,625	194328	8,575E-04	-
	0,500	190026	1,495E-03	-
Shell plate Beam stiffeners	1,000	200076	2,712E-04	4,362%
	0,875	200076	3,675E-04	3,934%
	0,750	200076	5,325E-04	3,131%
	0,625	200076	8,387E-04	2,187%
	0,500	200076	1,475E-03	1,318%

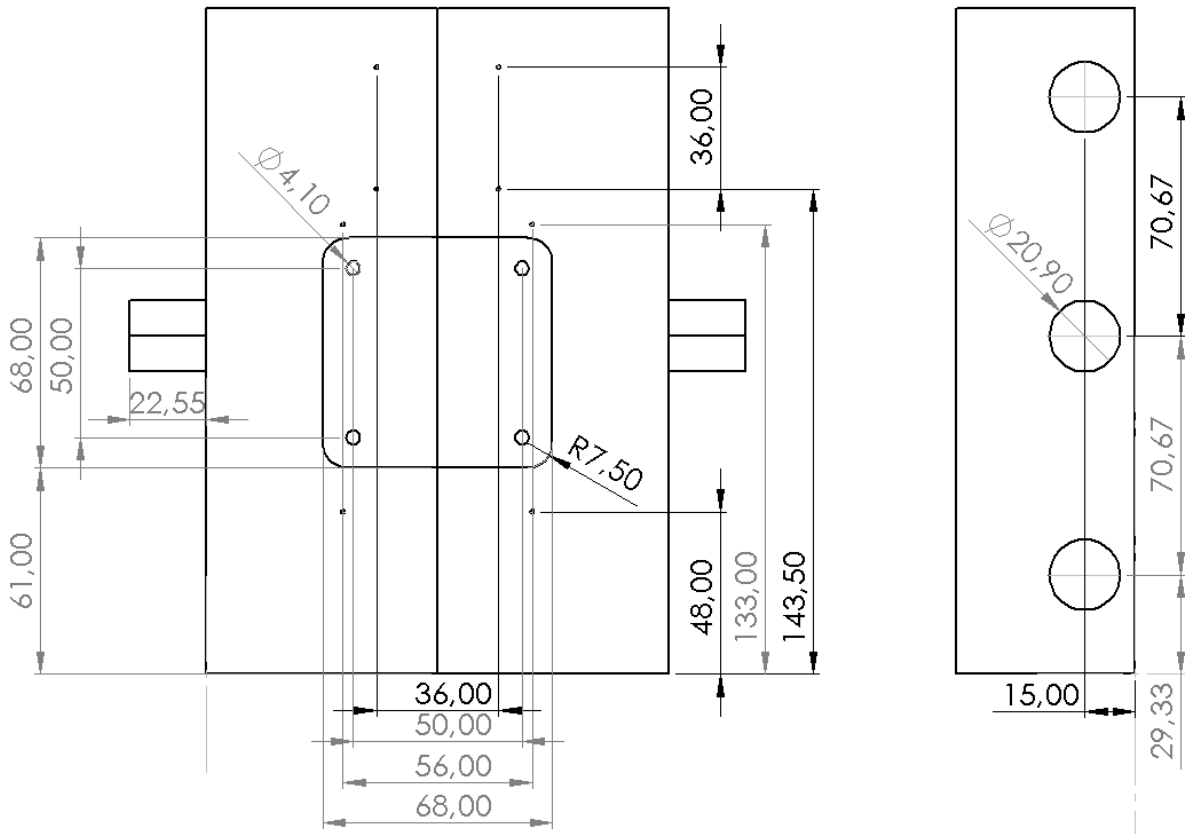
Data of shell - beam stiffener comparison, stiffener height and thickness reduced with H/t constant:

Element Type	Stiffener Height Ratio	N DOFs	Displacement [m]	Difference in disp. : (Shell-Beam)/Shell
Shell plate Shell stiffeners	1,000	205836	2,836E-04	-
	0,875	201534	4,299E-04	-
	0,750	200082	7,070E-04	-
	0,625	194328	12,94E-04	-
	0,500	190026	27,31E-04	-
Shell plate Beam stiffeners	1,000	200076	2,712E-04	4,362%
	0,875	200076	4,200E-04	2,296%
	0,750	200076	7,015E-04	0,776%
	0,625	200076	12,96E-04	-0,147%
	0,500	200076	27,45E-04	-0,505%

D

Simplified model parameters

Model geometry:



Component group	Part	Mass (g)	qty
Body	Alu chassis	293	1
	Base plate	91	1
	Fasteners (est.)	54,5	
	Sealings (est.)	30	
Leg Module Assembly	Leg	16	6
	Middle bush	25,5	2
	Corner bush	25	4
	Motor	13	6
	gearbox	27	6
	Temp sensor	2,5	6
	Motordrivers	7,2	6
	Legs total	595,6	
Solar Panel Plate	Plate	110	1
	Solar cell	3,56	12
	Sun sensor	33	1
	PCB (est.)	30	1
	SPP Total	238,6	
Solar Panel Deployment System	Motor	13	1
	Gearbox	27	1
	Driver	7,2	1
	SPDS Total	90,3	
Electronic Power System	Motherboard	50	1
	BMS PCB	35	1
	Harness	15	1
	Battery	48,5	4
	Misc.	51	
EPS total	345		

Middle LMA, component position and load:

Item	Offset (mm)	10G Force (N)	Torque (Nm)
Leg	52,5	1,5696	0,082404
Motor	0	1,2753	0
Gearbox	26	2,6487	0,068866
LMA Bushing	15,5	2,50155	0,038774
Temp sensor	-17	0,24525	-0,00417
Total	22,55	8,2404	0,185875

Corner LMA, component position and load:

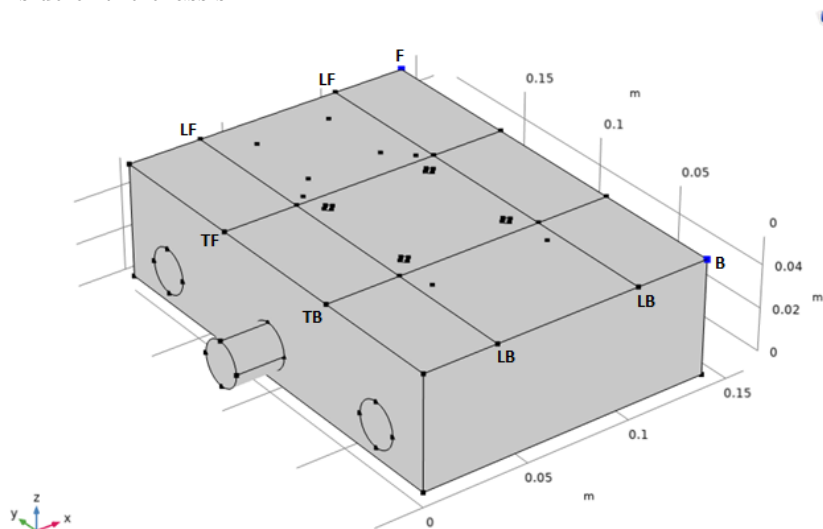
Item	Offset (mm)	10G Force (N)	Torque (Nm)
Leg	27	1,5696	0,082404
Motor	-27	1,2753	0
Gearbox	0	2,6487	0,068866
LMA Bushing	-10	2,4525	0,02453
Temp sensor	-43	0,2453	-0,00417
Total	-3.3	8,1914	-0,02712

Total offset height is the weighted average of all offsets and associated masses.

E

Large Rib Test

Reinforced model parameters, the labels indicate the Longitudinal and Transverse stiffeners on the Front and Back side of the chassis:



As the Lunar Zebro is launched in the Y-axis direction, the front section of the chassis top plate is critical in the buckling analysis. The section is about 70 by 70 millimeters between the attachment plate and the chassis front. Observing the deflections of the plain chassis from acceleration in the Y-axis, it is assumed the plate is pinned at the attachment plate and front edge and clamped along the rib edges, resulting in the K factor shown in the table below..

For the ribs, Euler beam buckling occurs over the rib thickness in the x-y plane and shear buckling in the y-z plane. Euler beam buckling is calculated taking fixed-guided constraints. The effective rib height includes the adjacent plate thickness in the buckling calculations.

<i>Description</i>	<i>Value</i>	<i>Unit</i>
Plate thickness	0.5	mm
Plate/Rib length	70	mm
Rib Height (from plate)	3.5	mm
Effective rib height	4.0	mm
Rib thickness	1.2	mm

<i>Buckling -</i>				
<i>Method</i>	<i>Factor</i>	<i>Load (N)</i>	<i>Safety Factor</i>	<i>Safe Load (N)</i>
Plate	K = 6.32	892.7	6	148.8
Euler Beam	C = 1	82.54	3	27.51
Shear Beam	-	37.69	3	12.56

Plain model deflections, no Leg Module masses or PCB stacks:

		<i>Deflection at corner nodes [μm]</i>					
Acceleration load axis:		X		Y		Z	
Structure point:		B	F	B	F	B	F
Original model		37,201	37,202	68,482	74,978	35,5933	60,521
Rib reinforced model		38,967	38,973	78,997	87,097	40,978	66,225

		<i>Deflection change [μm]</i>					
Loadcase:		X		Y		Z	
Point:		B	F	B	F	B	F
Rib adjusted:	LB	-0,184	-0,18	-2,805	-1,884	-1,591	1,023
	LF	-0,152	-0,161	-1,566	-2,772	1,232	-2,25
	TB	-1,621	-1,615	-2,297	-0,701	-3,752	0,996
	TF	-1,606	-1,622	-0,699	-2,75	1,149	-4,976

Equal deflection can be obtained by adjusting the Longitudinal rib sets.

Chassis with Leg Module masses, no PCB stack:

		<i>Deflection at corner nodes [μm]</i>					
Acceleration load axis:		X		Y		Z	
Structure point:		B	F	B	F	B	F
Original model		131,36	131,37	232,6	254,96	89,892	166,59
Rib reinforced model		136,17	136,18	270,2	297,7	117,04	206,8

		<i>Deflection change [μm]</i>					
Loadcase:		X		Y		Z	
Point:		B	F	B	F	B	F
Rib adjusted:	LB	-0,64	-0,62	-9,62	-6,45	-4,77	3,06
	LF	-0,54	-0,55	-5,36	-9,49	3,99	-7,28
	TB	-5,67	-5,63	-7,9	-2,4	-11,35	3
	TF	-5,62	-5,66	-2,4	-9,44	3,58	-15,52

In this model, the deflections resulting from Z acceleration increased most noticeably. Adjustments to the rib set do not sufficiently support Z-axis accelerations for equal deflection.

Chassis with Leg Module masses and PCB stack:

		<i>Deflection at corner nodes [μm]</i>					
Acceleration load axis:		X		Y		Z	
Structure point:		B	F	B	F	B	F
Original model		107,53	107,57	179,78	191,09	64,703	106,01
Rib reinforced model		108,82	108,15	194,41	208,88	80,5	132,14

		<i>Deflection change [μm]</i>					
Loadcase:		X		Y		Z	
Point:		B	F	B	F	B	F
Rib adjusted:	LB	-0,51	-0,44	-5,13	-3,36	-2,532	1,56
	LF	-0,34	-0,35	-2,66	-4,52	1,76	-3,13
	TB	-3,6	-3,51	-4,17	-1,32	-5,434	1,52
	TF	-3,49	-3,51	-1,17	-4,39	1,585	-6,81

Insufficient support to Z-axis acceleration.

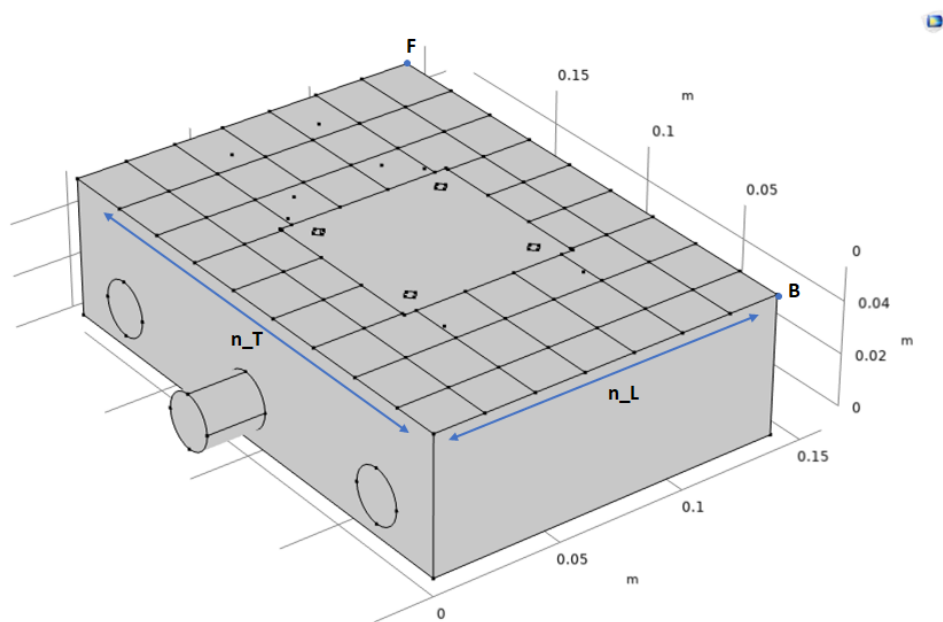
F

Rib Grid Test

As the stiffeners are small, here it is assumed plate sections between stiffeners are pinned. For the ribs, Euler beam buckling is calculated taking pinned-pinned constraints. The effective rib height includes the adjacent plate thickness in the buckling calculations.

<i>Description</i>	<i>Value</i>	<i>Unit</i>
Plate thickness	0.5	mm
Plate/Rib length	34	mm
Rib Height (from plate)	3.0	mm
Effective rib height	3.5	mm
Rib thickness	0.8	mm

<i>Buckling -</i>				
<i>Method</i>	<i>Factor</i>	Load (N)	Safety Factor	Safe Load (N)
Plate	$K = 3.29$	956.76	6	159.46
Euler Beam	$C = 1$	90.710	3	30.237
Shear Beam	-	42.500	3	14.166



Plain model deflections, no Leg Module masses or PCB stacks:

Loadcase:		Deflections [μm]					
		X		Y		Z	
Point:		B	F	B	F	B	F
Baseline:	Original chassis	37,201	37,202	68,482	74,978	35,5933	60,521
	nL, nT = [5 , 7]	46,249	46,301	105,43	115,72	42,801	75,385
Grid density:	nL, nT = [5 , 8]	37,221 *	37,210 *	91,286	99,775	35,623 *	62,724 *
	nL, nT = [6 , 8]	36,673 *	36,676 *	82,243	90,159	35,176 *	60,415 *

In the following tables, nL and nT corresponds to the number of longitudinal and transverse stiffeners as shown in the model diagram on the previous page.

Full model deflections, LMA mass and PCB stacks included:

Loadcase:		Deflections [μm]					
		X		Y		Z	
Point:		B	F	B	F	B	F
Base model:	Original chassis	107,53	107,57	179,78	191,09	64,703	106,01
	nL, nT = [5 , 7]	115,39	113,80	221,50	231,91	86,631	129,94
Grid density:	nL, nT = [5 , 8]	104,88 *	105,55 *	209,16	224,30	67,450	119,02
	nL, nT = [6 , 8]	98,906	99,773	181,49 *	195,04 *	65,605 *	111,26

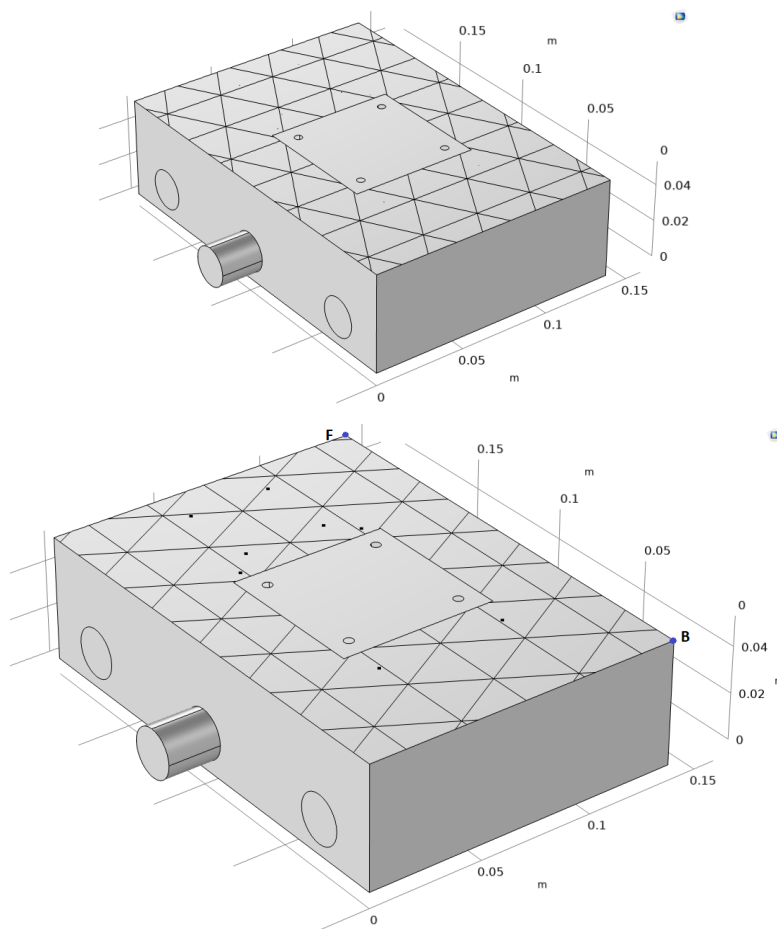
Comparing the deflections of the base model with those of the [6, 8] rib grid model, the deflections are almost equal in both tests (cells indicated with *). The PCB stack provides noticeable reinforcement in the X and Y acceleration. However, in the Z-acceleration load the deflections are slightly increased.

Rib slenderness test, model deflections with LMA mass and PCB stacks included:

Loadcase:		Deflections [μm]					
		X		Y		Z	
Point:		B	F	B	F	B	F
Rib slenderness:	3,75	98,906	99,773	181,49	195,04	65,605	111,26
	2,25	102,33	103,24	186,38	200,45	67,476	114,75
	1	107,86	108,83	192,98	207,70	70,826	120,40

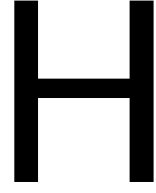
G

Iso Grid Test



Both iso grid models which resulted in near equal stiffness are shown above. With equal deflection to the original chassis model as a priority, the second tested orientation behaves significantly better in the Y and Z accelerations.

Loadcase:	Deflections [μm]					
	X		Y		Z	
Point:	B	F	B	F	B	F
Original 1.5mm chassis	107,53	107,57	179,78	191,09	64,703	106,01
Iso grid orientation 1	104,36	103,74	191,22	198,18	76,846	107,17
Iso grid orientation 2	103,19	102,68	177,03	189,28	65,917	110,95



Grid Equivalent Stiffness Matrix

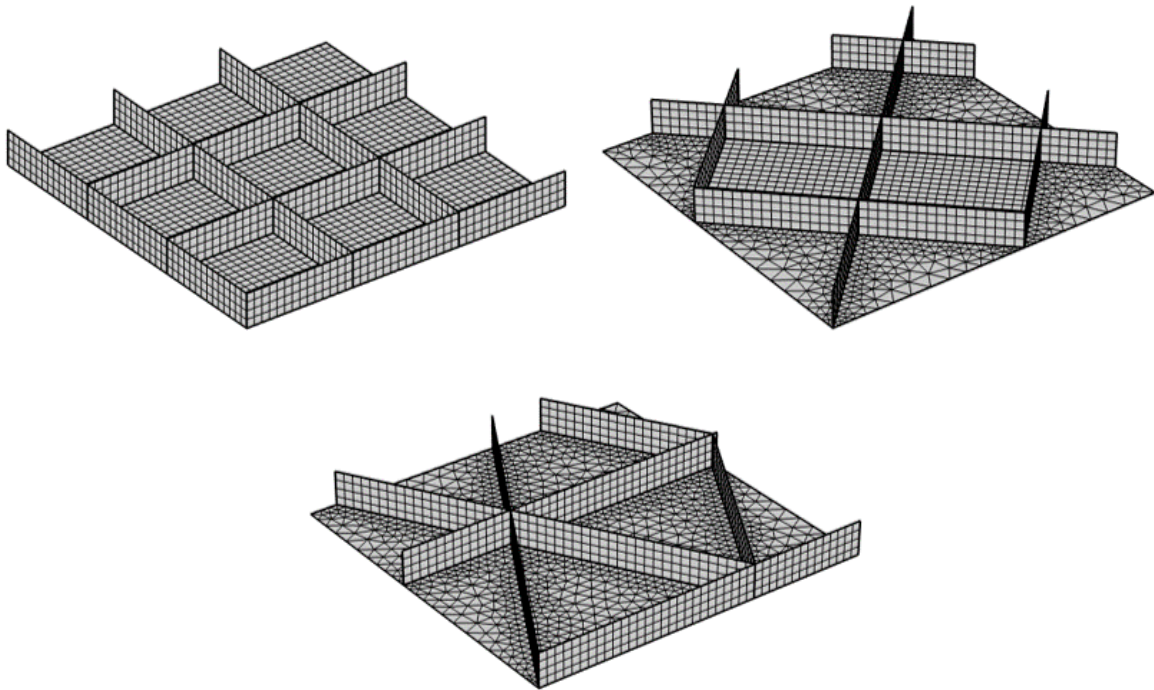
$$\begin{bmatrix} A^{st} & B^{st} \\ B^{st} & D^{st} \end{bmatrix} =$$

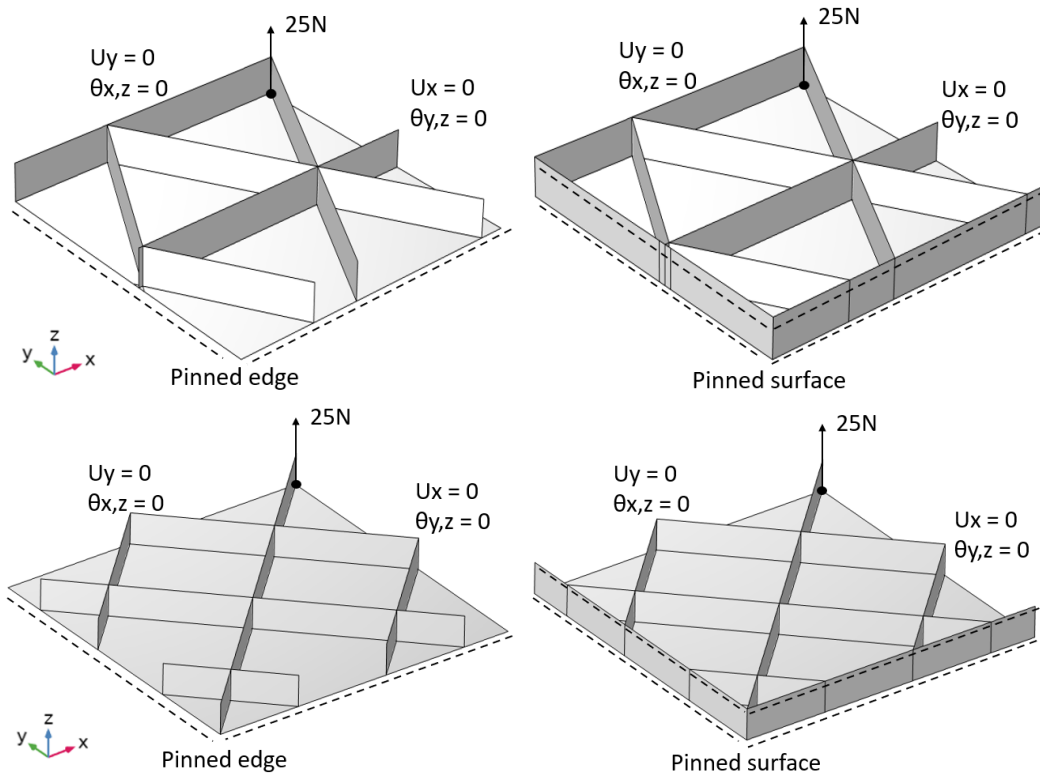
$$\begin{bmatrix} R_a (2k_1 c^3 + k_3 + 2k_5) / b_0 & 2R_a k_1 s^2 c / b_0 & 0 & R_b (2k_1 c^3 + k_3 + 2k_5) / b_0 & 2R_b k_1 s^2 c / b_0 & 0 \\ 2R_a k_1 s c^2 / a_0 & R_a (2k_1 s^3 + k_4 + 2k_6) / a_0 & 0 & 2R_b k_1 s c^2 / a_0 & R_b (2k_1 s^3 + k_4 + 2k_6) / a_0 & 0 \\ 0 & 0 & 2R_a k_1 s^2 c / b_0 & 0 & 0 & 2R_b k_1 s^2 c / b_0 \\ R_b (2k_1 c^3 + k_3 + 2k_5) / b_0 & 2R_b k_1 s^2 c / b_0 & 0 & R_d (2k_1 c^3 + k_3 + 2k_5) / b_0 & 2R_d k_1 s^2 c / b_0 & 0 \\ 2R_b k_1 s c^2 / a_0 & R_b (2k_1 s^3 + k_4 + 2k_6) / a_0 & 0 & 2R_d k_1 s c^2 / a_0 & R_d (2k_1 s^3 + k_4 + 2k_6) / a_0 & 0 \\ 0 & 0 & 2R_b k_1 s^2 c / b_0 & 0 & 0 & 2R_d k_1 s^2 c / b_0 \end{bmatrix}$$



Grid comparison OoP load

COMSOL Multiphysics meshes of the grid reinforced plates for the Out of Plane load test:

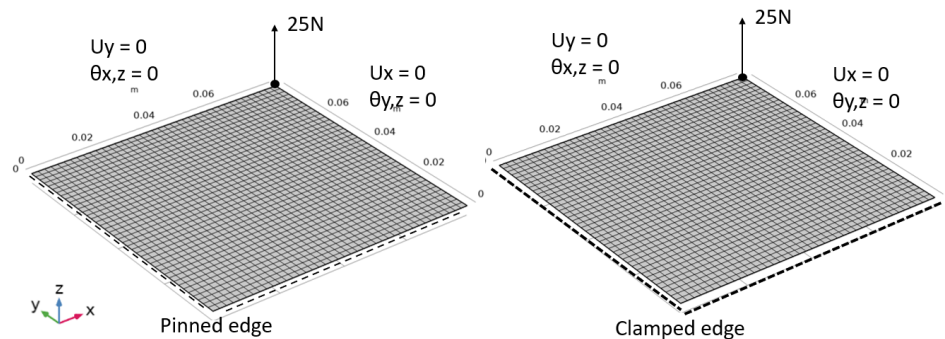




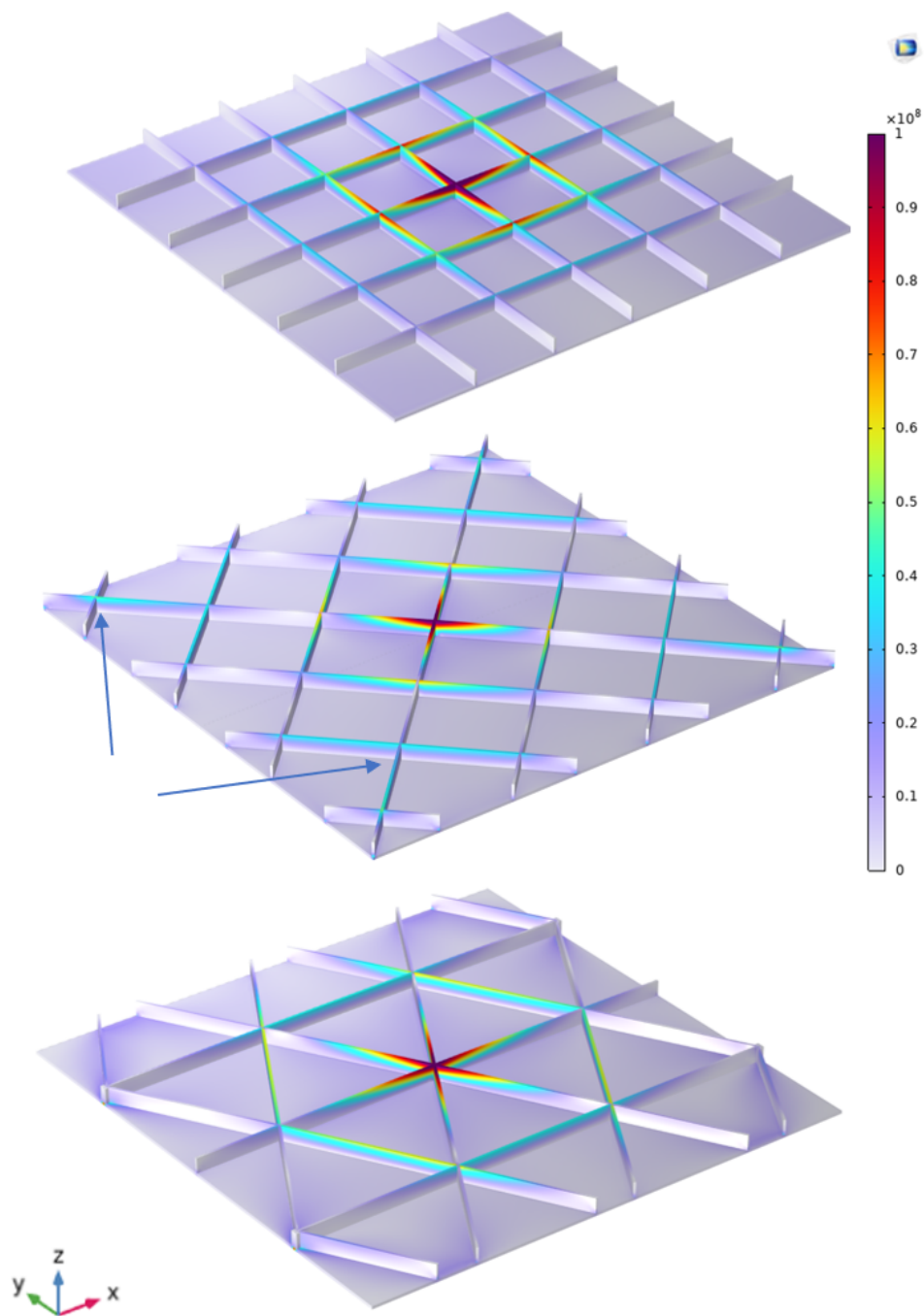
Pinned grid:	Iso		Ortho		Waffle	
Grid mass %	D [mm]	DOFs	D [mm]	DOFs	D [mm]	DOFs
20%	0,51001	51102	0,5450	64362	0,4138	54663
30%	0,2808	51102	0,2900	64362	0,2236	54663
40%	0,1804	56514	0,1826	70500	0,1443	59769
50%	0,1282	56514	0,1281	70500	0,1040	59769
60%	0,09812	56514	0,09740	70500	0,08113	59769

Walled grid:	Iso		Ortho		Waffle	
Grid mass %	D [mm]	DOFs	D [mm]	DOFs	D [mm]	DOFs
20%	0,2279	60360	0,2086	70950	0,2535	62643
30%	0,1266	60360	0,1152	70950	0,142	62643
40%	0,08375	67776	0,0762	79110	0,09402	69705
50%	0,06201	67776	0,05648	79110	0,06938	69705
60%	0,04987	67776	0,04546	79110	0,05548	69705

The plain plate model has 39366 DOFs and centerpoint deflections of 0.16978 and 0.35157 mm.

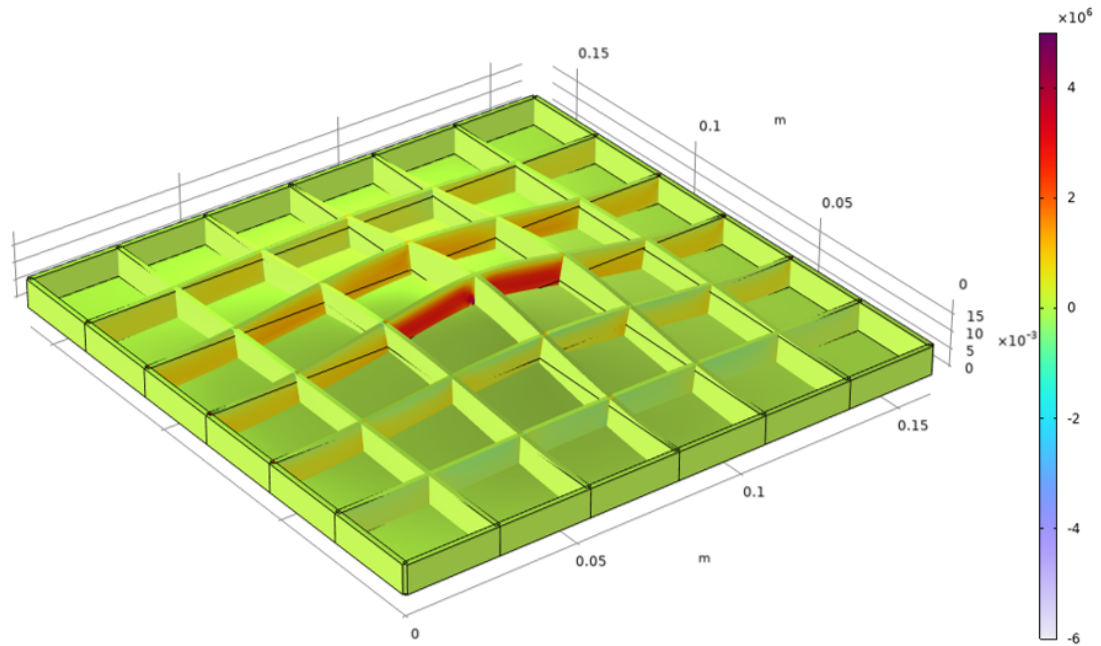


von Mises stress, Gauss Point evaluation (N/m²) in COMSOL Multiphysics:

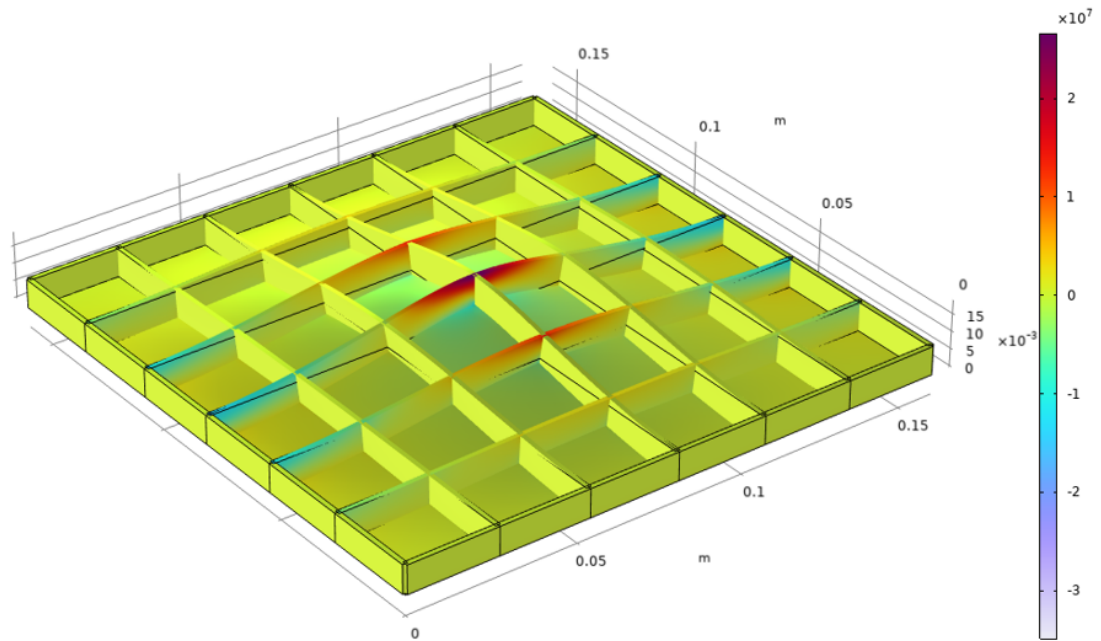


The waffle grid experiences significant stress at the outer corners. Observe that the other grid types have higher stresses in the plate rather than the ribs along the outer plate edge.

The considered smeared stiffness approach and resulting ESM neglect the out of plane shear loads, $\tau_{xz,yz}$. Below the observed axial stress xx-component is shown for the largest evaluated ortho grid, with a rib height of 8.2mm and plate thickness of 0.47mm. These are the largest observed shear stresses of all analysed grids.

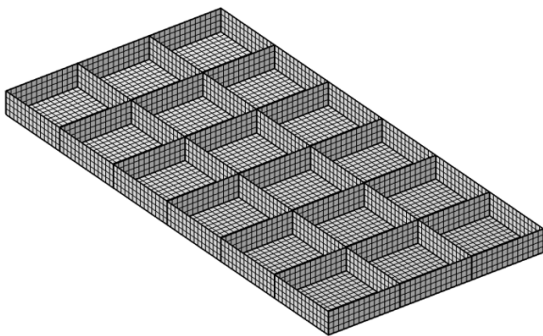
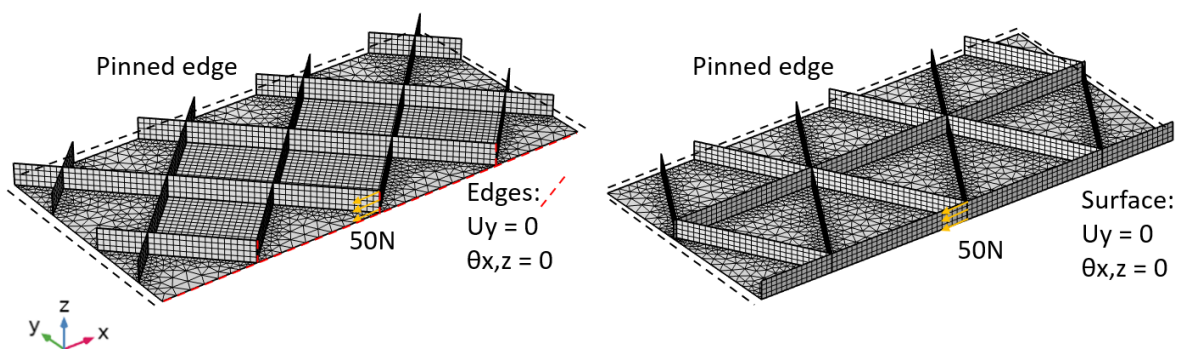


Comparing these stresses to the axial stress xz-component, observe that the stress range is reduced by a factor of 8.

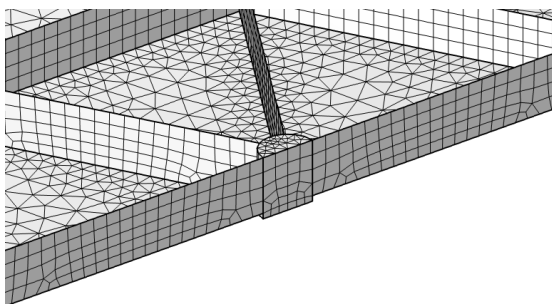


J

Grid comparison in-plane load



Mesh of the distributed body load on a $D=8\text{mm}$ cylinder:



Pinned grid:	Iso		Ortho		Waffle	
<i>Web mass %</i>	<i>D [mm]</i>	<i>DOFs</i>	<i>D [mm]</i>	<i>DOFs</i>	<i>D [mm]</i>	<i>DOFs</i>
20%	0,003984	94458	0,004680	125112	0,005053	104409
30%	0,002941	94458	0,003503	125112	0,003820	104409
40%	0,002378	105288	0,002881	136356	0,003164	114609
50%	0,002050	105288	0,002529	136356	0,002795	114609
60%	0,001857	105288	0,002341	136356	0,002602	114609

Walled grid:	Iso		Ortho		Waffle	
<i>Web mass %</i>	<i>D [mm]</i>	<i>DOFs</i>	<i>D [mm]</i>	<i>DOFs</i>	<i>D [mm]</i>	<i>DOFs</i>
20%	0,003668	112551	0,004406	138288	0,004806	122334
30%	0,002771	112551	0,003374	138288	0,003680	122334
40%	0,002299	127353	0,002833	153576	0,003085	136506
50%	0,002026	127353	0,002525	153576	0,002753	136506
60%	0,001863	127353	0,002352	153576	0,002582	136506

Bibliography

- [1] G H Heiken, D T Vaniman, and B M French. *Lunar sourcebook : a user's guide to the Moon*. Tech. rep. Cambridge University Press, 1991. URL: www.lpi.usra.edu/publications/books/lunar_sourcebook/.
- [2] James Richard. Wertz and Wiley J. Larson. *Space mission analysis and design*. Microcosm, 1999, p. 969. ISBN: 1881883108.
- [3] “Third Stage Fact Sheet”. In: *Saturn V News Reference* (1968).
- [4] SpaceX. *Falcon User's Guide*. Tech. rep. Space Exploration Technologies Corp., 2020. URL: www.spacex.com/media/falcon-users-guide-2021-09.pdf.
- [5] Jacob Job Wijker. *Spacecraft structures*. Springer Berlin Heidelberg, 2008, pp. 1–504. ISBN: 9783540755524. DOI: 10.1007/978-3-540-75553-1.
- [6] G. Cremonese et al. “Micrometeoroids flux on the Moon”. In: *Astronomy and Astrophysics* 551 (2013). ISSN: 00046361. DOI: 10.1051/0004-6361/201220541.
- [7] K. Bhanu Sankara Rao, B. Raj, and A. Nagesha. “Fatigue Testing: Thermal and Thermomechanical”. In: *Reference Module in Materials Science and Materials Engineering* (2017). DOI: 10.1016/B978-0-12-803581-8.03464-0.
- [8] Richard H Maurer et al. *Harsh Environments: Space Radiation Environment, Effects, and Mitigation*. Tech. rep. 1. Johns Hopkins APL, 2008.
- [9] J B Miog. “Design of the locomotion subsystem for Lunar Zebro A design and implementation to ensure that Zebro can thrive on the moon”. PhD thesis. Delft: TU Delft, 2018.
- [10] Annadurai M. *Future Exploration Missions of ISRO*. Tech. rep. UNCOPUOS 60th Session, 2017. URL: <https://www.unoosa.org/documents/pdf/copuos/2017/copuos2017tech30E.pdf>.
- [11] Alex Ellery. *PLANETARY ROVERS Robotic Exploration of the Solar System*. Tech. rep. 2016. URL: <http://www.springer.com/series/5495>.
- [12] Craig Covault. “China's Bold Lunar Plan”. In: *Aerospace America* November (2013), pp. 24–29.
- [13] Kassel Simon. “Lunokhod-1 Soviet Lunar Surface Vehicle”. In: *The Rand Corporation* (1971).
- [14] O A Le. *Lunar Roving Vehicle Operations Handbook*. Tech. rep. Huntsville: The Boeing Company, Apr. 1971.
- [15] James R Gaier. *The Effects of Lunar Dust on EVA Systems During the Apollo Missions*. Tech. rep. 2005. URL: <http://www.sti.nasa.gov>.
- [16] Gregory S Hickey et al. *Integrated Lightweight Structure and Thermal Insulation for Mars Rover*. Tech. rep. 1995, pp. 656–666. URL: <https://www.jstor.org/stable/44611970>.
- [17] P S Schenker et al. *Lightweight rovers for Mars science exploration and sample return*. Tech. rep. Pasadena: Jet Propulsion Laboratory, California Institute of Technology, 1996.
- [18] Joy A. Crisp et al. “Mars Exploration Rover mission”. In: *Journal of Geophysical Research E: Planets* 108.12 (Dec. 2003). ISSN: 01480227. DOI: 10.1029/2002je002038.
- [19] Darlene S Lee. *Mars Exploration Rover Primary Payload Design and Verification*. Tech. rep. NASA JPL, 2003.
- [20] Keith S Novak et al. *Development of a Thermal Control Architecture for the Mars Exploration Rovers*. Tech. rep. 13. 2003.
- [21] *Mars 2020/Perseverance*. Tech. rep. NASA, 2020. URL: www.nasa.gov.
- [22] Emily Lakdawalla. *The Design and Engineering of Curiosity*. Springer International Publishing, 2018. DOI: 10.1007/978-3-319-68146-7.

- [23] Pradeep Bhandari et al. *Mars Science Laboratory Thermal Control Architecture*. Tech. rep. Jet Propulsion Laboratory, California Institute of Technology, 2005.
- [24] Gasser F. Abdelal, Nader Abuefoutouh, and Ahmed H. Gad. *Finite element analysis for satellite structures: Applications to their design, manufacture and testing*. Springer-Verlag London Ltd, Jan. 2013, pp. 1–334. ISBN: 9781447146377. DOI: 10.1007/978-1-4471-4637-7.
- [25] Ali Aborehab et al. “Configuration design and modeling of an efficient small satellite structure”. In: *Engineering Solid Mechanics* 8.1 (2020), pp. 7–20. ISSN: 22918752. DOI: 10.5267/j.esm.2019.9.002.
- [26] ECSS and ESA-ESTEC. *Space engineering Mechanical - Part 2: Structural*. Tech. rep. Noordwijk: The European Space Agency, 2000.
- [27] Bruce Yost and Sasha Weston. *Small Spacecraft Technology State of the Art report*. Tech. rep. Moffett Field: Ames Research Center, NASA, 2021. URL: <http://www.sti.nasa.gov>.
- [28] ISISPACE. *ISISPACE 2-Unit CubeSat structure*. 2013.
- [29] Stephen Horan et al. *The Three Corner Satellite Mission*. Tech. rep. New Mexico State University, 2002. URL: <https://www.researchgate.net/publication/268359920>.
- [30] Bayon S. *CDF STUDY REPORT COMET INTERCEPTOR Assessment of Mission to Intercept a Long Period Comet or Interplanetary Object*. Tech. rep. Noordwijk: ESA, 2019.
- [31] Karthigesu Thanarasi. “Thermal analysis of CUBESAT in worse case hot and cold environment using FEA method”. In: *Applied Mechanics and Materials*. Vol. 225. 2012, pp. 497–502. ISBN: 9783037855065. DOI: 10.4028/www.scientific.net/AMM.225.497.
- [32] NASA. *Micrometeor Protection*. 1999. URL: <https://llis.nasa.gov/lesson/705>.
- [33] J C Brown, A J Robertson, and Stan T Serpento. *Motor Vehicle Structures: Concepts and Fundamentals*. Tech. rep. 2002.
- [34] E C Tsirogiannis. *Design of an efficient and lightweight chassis, suitable for an electric car*. Tech. rep. Chania: Technical University of Crete, 2015. URL: <https://www.researchgate.net/publication/313475487>.
- [35] Y.C. Lam and S. Santhikumar. “Automated rib location and optimization for plate structures”. In: *Structural and Multidisciplinary Optimization* 25.1 (Mar. 2003), pp. 35–45. ISSN: 1615-147X. DOI: 10.1007/s00158-002-0270-7.
- [36] Luyang Tan et al. “Multi-objective topology optimization to reduce vibration of micro-satellite primary supporting structure”. In: *Journal of Vibroengineering* 19.2 (2016), pp. 831–843. ISSN: 13928716. DOI: 10.21595/jve.2016.17517.
- [37] Ji Hong Zhu, Wei Hong Zhang, and Liang Xia. “Topology Optimization in Aircraft and Aerospace Structures Design”. In: *Archives of Computational Methods in Engineering* 23.4 (Dec. 2016), pp. 595–622. ISSN: 18861784. DOI: 10.1007/s11831-015-9151-2.
- [38] Christos Kassapoglou. *Design and Analysis of Composite Structures*. Wiley, May 2013. ISBN: 9781118401606. DOI: 10.1002/9781118536933.
- [39] *Body&Thermal documentation Phase B*. Tech. rep. Delft: Lunar Zebro Structures Department, TU Delft, 2020.
- [40] F. VAN KEULEN and J. BOOIJ. “REFINED CONSISTENT FORMULATION OF A CURVED TRIANGULAR FINITE ROTATION SHELL ELEMENT”. In: *International Journal for Numerical Methods in Engineering* 39.16 (Aug. 1996), pp. 2803–2820. ISSN: 0029-5981. DOI: 10.1002/(SICI)1097-0207(19960830)39:16<2803::AID-NME977>3.0.CO;2-2.
- [41] Coen Bakker. “Simultaneous optimization of the topology and the layout of modular stiffeners on shells and plates”. PhD thesis. Delft: Technical University Delft, 2020. URL: [https://repository.tudelft.nl/..](https://repository.tudelft.nl/)
- [42] S Herranz et al. “The milling of airframe components with low rigidity: A general approach to avoid static and dynamic problems”. In: *Proceedings of the Institution of Mechanical Engineers, Part B: Journal of Engineering Manufacture* 219.11 (Nov. 2005), pp. 789–801. ISSN: 0954-4054. DOI: 10.1243/095440505X32742.

-
- [43] Warren C. Young and Rychard G. Budynas. *Roark's Formulas for Stress and Strain*. 7th ed. New York: The McGraw-Hill Companies, Inc., 2002. ISBN: 0-07-072542-X.
- [44] Yuanming Xu et al. "A new effective smeared stiffener method for global buckling analysis of grid stiffened composite panels". In: *Composite Structures* 158 (Dec. 2016), pp. 83–91. ISSN: 02638223. DOI: 10.1016/j.compstruct.2016.09.015. URL: <https://doi.org/10.1016/j.compstruct.2016.09.015>.
- [45] NASA/JPL-Caltech. *Mars Oxygen ISRU Experiment*. 2021. URL: <https://photojournal.jpl.nasa.gov/catalog/PIA24201>.
- [46] Yu Luan, Mogens Ohlrich, and Finn Jacobsen. "Improvements of the smearing technique for cross-stiffened thin rectangular plates". In: *Journal of Sound and Vibration* 330.17 (Aug. 2011), pp. 4274–4286. ISSN: 0022460X. DOI: 10.1016/j.jsv.2011.03.021. URL: <https://doi.org/10.1016/j.jsv.2011.03.021>.
- [47] R.R. Meyer. *Isogrid Design Handbook*. Tech. rep. Huntington Beach: McDonnell Douglas Astronautics Company, 1972. URL: <https://ntrs.nasa.gov/citations/19720000322>.
- [48] Jeremy P. Gray and Frank Campagna. "Human-like characteristics for high degree of freedom robotic door-opening end-effector". In: ed. by Douglas W. Gage et al. May 2011. DOI: 10.1117/12.886139.